

Topological quantum optics from long-range to all-to-all interactions

Dissertation

der Mathematisch-Naturwissenschaftlichen Fakultät
der Eberhard Karls Universität Tübingen
zur Erlangung des Grades eines
Doktors der Naturwissenschaften
(Dr. rer. nat.)

Mathias Bo Mjøen Svendsen
aus Tromsø (Norwegen)

Tübingen

2025

Abstract

In this thesis, we study topological phases and phenomena in quantum many-body atomic systems coupled to a common environment. Atoms coupled to a common environment display collective behaviour, including induced long-range dipole-dipole interactions and collective dissipation of excitations into the environment. Many-body quantum optical systems are promising platforms to study topological phases due to the high degree of control of the system parameters that can be achieved by changing, for example, the interatomic spacings. Coupling the atomic system to a structured environment, like a dielectric or metallic structure, allows for tailoring the dipole-dipole interactions to reach a given strength and range of interactions. Interactions can even be made all-to-all by coupling the atoms to a nanophotonic waveguide. The high control of the interactions enables both the study of existing topological models and the exploration of new ones with long-range interactions, where little is known about the fate of topological properties. Furthermore, the controllable interactions enable the study of topological transport mechanisms such as topological pumping, which is based on cyclic variation of the Hamiltonian parameters. As a result of the collective behaviour, topological phases can be made subradiant, which allows for the study of long-lived topological dynamics.

In the first original work resulting from the work in this Thesis, we derive the induced dipole-dipole interactions between an ensemble of atoms coupled to a nanophotonic waveguide by means of the electromagnetic Green's tensor. We derive, analytically, the all-to-all dipole-dipole interactions stemming from the guided modes of the waveguide. Moreover, we provide, for the first time, a numerical method for computing with high precision, the unguided contribution to the dipole-dipole interactions. This interaction differs significantly from its free space counterpart, especially when the atoms are close to the waveguide surface. We illustrate this by comparing the transmission of fiber-guided light from free space modes and the numerically computed unguided modes, where not only the resonance peaks are shifted, but an overall deformation of the transmission spectrum is evident for a large atomic system size.

In the second and third original works, we study the existence of topological

phases in many-body quantum optical systems in the presence of long-range to all-to-all interactions. In particular, we study the robust topological transport of a photon embedded in a one-dimensional chain in three relevant quantum optics platform, namely Rydberg atoms, atoms in low-lying states in free space and atoms coupled to a nanophotonic waveguide. We show topological transport of a photon, which is robust against local disorder in the atomic position. The transport can be performed subradiantly in the case of atoms in low-lying states and atoms coupled to a waveguide, or within the lifetime of the Rydberg atoms. Finally, we present a two-dimensional topological model with Rydberg atoms. The model displays a myriad of distinct topological phases, including two weak topological insulating phases, characterized by edge states occupying only one boundary, and a weakly broken higher order topological insulating phase with corner-like states. Moreover, a semi-metallic phase is found manifested by a pair of oppositely topologically charged and tunable Dirac points and associated tilted and anisotropic cones. For specific parameter choices, the Dirac points collapse into nodal lines.

Zusammenfassung

In dieser Arbeit untersuchen wir topologische Phasen und Phänomene in atomaren Vielteilchensystemen, die an eine gemeinsame Umgebung gekoppelt sind. Atome, die an eine gemeinsame Umgebung gekoppelt sind, zeigen ein kollektives Verhalten, einschließlich induzierter weitreichender Dipol-Dipol-Wechselwirkungen und kollektiver Dissipation von Anregungen in die Umgebung. Quantenoptische Vielteilchensysteme sind eine vielversprechende Plattform zur Untersuchung topologischer Phasen, da die Systemparameter in hohem Maße kontrolliert werden können, indem beispielsweise die Abstände zwischen den Atomen verändert werden. Darüber hinaus ermöglicht die Kopplung des atomaren Systems an eine strukturierte Umgebung, z. B. eine dielektrische oder metallische Struktur, die Anpassung der Dipol-Dipol-Wechselwirkungen, um die gewünschte Stärke und Bandbreite der Wechselwirkungen zu erreichen. Durch Kopplung an einen nanophotonischen Wellenleiter können sogar Wechselwirkungen mit unendlicher Reichweite hergestellt werden. Die hohe Kontrolle über die Wechselwirkungen ermöglicht es, sowohl bestehende topologische Modelle zu untersuchen als auch neue Modelle mit weitreichenden Wechselwirkungen zu erforschen, bei denen wenig über den Verbleib der topologischen Eigenschaften bekannt ist. Darüber hinaus ermöglichen die kontrollierbaren Wechselwirkungen die Untersuchung von topologischen Transportmechanismen wie dem topologischen Pumpen, das auf der zyklischen Variation der Hamilton-Parameter beruht. Aufgrund des kollektiven Verhaltens können topologische Phasen subradiant gemacht werden, was die Untersuchung der langlebigen topologischen Dynamik ermöglicht.

In der ersten wissenschaftlichen Arbeit leiten wir die induzierten Dipol-Dipol-Wechselwirkungen zwischen einem Ensemble von Atomen, die an einen nanophotonischen Wellenleiter gekoppelt sind, mit Hilfe des elektromagnetischen Greenschen Tensors her. Wir zeigen analytisch, dass sich die Dipol-Dipol-Wechselwirkungen aus den geführten Moden des Wellenleiters ergeben. Darüber hinaus stellen wir zum ersten Mal eine numerische Methode zur Verfügung, mit der der ungeliebte Beitrag zu den Dipol-Dipol-Wechselwirkungen mit hoher Genauigkeit berechnet werden kann. Diese Wechselwirkung unterscheidet sich er-

heblich von ihrem Gegenstück im freien Raum, insbesondere dann, wenn sich die Atome nahe der Oberfläche des Wellenleiters befinden. Wir veranschaulichen dies durch den Vergleich der Übertragung von fasergeführtem Licht aus Freiraummoden und den numerisch berechneten ungelenkten Moden, wobei nicht nur die Resonanzspitzen verschoben werden, sondern eine allgemeine Deformation des Übertragungsspektrums für ein großes atomares system zu beobachten ist.

In der zweiten und dritten wissenschaftlichen Arbeit untersuchen wir die Existenz von topologischen Phasen in quantenoptischen Vielteilchensystemen mit langreichweitigen bis hin zu uendlich-reichweitigen Wechselwirkungen. Insbesondere untersuchen wir den robusten topologischen Transport eines in eine eindimensionale Kette eingebetteten Photons in drei relevanten, quantenoptischen Plattformen, nämlich Rydberg-Atomen, Atomen in tiefliegenden Zuständen im freien Raum und Atomen, die mit einem nanophotonischen Wellenleiter gekoppelt sind. Wir demonstrieren den topologischen Transport eines Photons, der gegenüber lokaler Unordnung in der atomaren Position resistent ist. Der Transport kann im Fall von Atomen in tiefliegenden Zuständen und Atomen, die an einen Wellenleiter gekoppelt sind, subradian oder innerhalb der Lebensdauer der Rydberg-Atome erfolgen. Schließlich stellen wir ein zweidimensionales topologisches Modell mit Rydberg-Atomen vor. Das Modell zeigt eine Vielzahl unterschiedlicher topologischer Phasen, darunter zwei schwache topologische Isolationsphasen, die durch Randzustände an lediglich einer außenkante des systems gekennzeichnet sind, und eine schwach gebrochene topologische Isolationsphase höherer Ordnung mit eckenartigen Zuständen. Darüber hinaus finden wir eine halbmetallische Phase, die sich durch ein Paar topologisch entgegengesetzt geladener und abstimmbarer Dirac-Punkte und zugehörige geneigte und anisotrope Kegel manifestiert. Bei der Wahl bestimmter Parameter kollabieren die Dirac-Punkte zu Knotenlinien.

List of publications and personal contribution

List of publications

1. Mathias B. M. Svendsen and Beatriz Olmos. *Modified dipole-dipole interactions in the presence of a nanophotonic waveguide*, Quantum **7**, 1091 (2023)
2. Mathias B. M. Svendsen, Marcel Cech, Max Schemmer and Beatriz Olmos *Topological photon pumping in quantum optical systems*, Quantum **8**, 1488 (2024)
3. Mathias B. M. Svendsen and Beatriz Olmos. *A kaleidoscope of topological phases in 2D Rydberg lattices*

Personal contribution of the candidate

No.	Scientific ideas	Data generation	Analysis and interpretation	Paper writing	Status
1	50%	100%	70%	50%	Published
2	60%	100%	70%	60%	Published
3	100%	100%	90%	100%	Preprint

Acknowledgments

First of all, I would like to thank my supervisor Prof. Beatriz Olmos Sanchez for her guidance throughout my PhD. You have always been available when I got stuck and I have truly enjoyed our discussions. I am grateful for your support and enthusiasm whenever I have shown you my scientific ideas. My thanks also go to Marcel Cech and Max Schemmer for our collaboration on a long, but rewarding project. I would like to express a special appreciation to my fellow PhD and postdoc group members: Albert, Cecilia, Gabriele, Björn, Parvinder, Joe, Mario, Marcel, Simon, Robert, Marc, Chris, Paulo, Sofía, Wilson and our former members Matteo and Francesco. I have thoroughly enjoyed our talks, both at and after work. Tübingen would not have been the same without you. I would also like to extend my appreciation to our secretary Ingrid for her help with handling the German bureaucracy.

I am forever grateful for my family and their constant support. It is always a pleasure to return home for holidays. A special thanks go to my brother for all our adventures, both back home and skiing or hiking in the alps. Finally, to my girlfriend Franziska. Thank you for all your support. I am looking forward to many more days with you tending our vegetable garden.

Contents

1	Introduction	1
1.1	Topological protection	1
1.2	Many-body quantum optics	2
1.3	Topology in quantum optics	4
1.4	Structure of the thesis	6
2	The quantum master equation and quantum electrodynamics	7
2.1	The Quantum Optical Master Equation	7
2.2	The electromagnetic Green's tensor	11
2.2.1	Green's tensor in free space	13
2.2.2	Green's tensor for a cylindrical waveguide	16
2.3	Rydberg atoms	21
3	Topology in physics	23
3.1	Characterization of topological phases	23
3.2	Adiabatic evolution, Berry phase and Berry curvature	27
3.3	The SSH model	30
3.4	Topological pumping	34
3.5	Robust quantum state transfer	38
4	Modified dipole-dipole interactions in waveguide QED	43
4.1	Introduction	43
4.2	System and master equation	44
4.3	Green's tensor for a cylindrical nanofiber	45
4.3.1	Guided modes	45
4.3.2	Radiation modes	47
4.3.3	Numerical evaluation of the radiative dipole-dipole interactions	50
4.3.4	Modified dipole-dipole interaction between two atoms near a nanofiber	52

4.4	Transmission of fiber-guided light	53
4.5	Conclusions and outlook	55
5	Topological photon pumping	57
5.1	Introduction	57
5.2	Topological pumping in one dimension	58
5.2.1	Topological pumping and dispersion	61
5.3	The extended Rice-Mele model	62
5.3.1	Topological properties of the extended Rice-Mele model . .	64
5.4	Topological photon pumping in quantum optics	67
5.4.1	Short-range hopping: Rydberg atoms	68
5.4.2	Long-range hopping: Atoms in free space	71
5.4.3	All-to-all hopping: Waveguide system	73
5.5	Robustness against dissipation and disorder	76
5.5.1	Dissipation	76
5.5.2	Disorder	78
5.6	Conclusions and outlook	80
6	Topological phases in a 2D Rydberg lattice	83
6.1	Introduction	83
6.2	The 2D SSH model with Rydberg atoms: Bulk properties	84
6.3	Semi-metallic phase	88
6.4	Topological gapped phases	91
6.4.1	Semi-infinite system	91
6.4.2	Finite system	94
6.4.3	Edge excitation dynamics	96
6.4.4	Robustness against defects	97
6.5	Conclusion and outlook	98
7	Conclusion and outlook	99
	Bibliography	120

Chapter 1

Introduction

1.1 Topological protection

Topology is concerned with classes of objects, which can be formed to one another by continuous and smooth deformations like stretching, bending or twisting, but without tearing or gluing. The classic example is that a coffee cup can be continuously deformed into a donut, however not into a ball since this would require gluing the hole in the handle. In this sense, a coffee cup and a donut are topologically equivalent and belong to the same topological class classified by a *topological invariant*, which in this example is the number of holes. The same concept can be equivalently applied to phases in physics. In physics, we say that a topological phase is a phase which is robust against adiabatic local, but finite perturbations. These perturbations are the smooth deformations like stretching, bending or twisting from the previous example with the cup and the donut. Topological phases cannot be described by localized many-body wavefunctions. On the contrary, the information is stored non-locally over the whole system manifested by the robustness against local disorder. A change of the topology of a system is always signified by a phase transition, i.e. a closing of the gap in the energy spectrum.

The field of topology has been an important branch of mathematics for the last 100 years initiated by the work of Poincaré in the late 19th century. One of the first applications of topology in theoretical physics was the analysis of magnetic monopoles by Dirac in 1931 [1]. He calculated that the flux through a closed loop surrounding the monopole is quantized in integer steps n , a topological invariant. However, the field of topology in physics first exploded in the 1980s with the discovery of the quantum Hall effect.

The quantum Hall effect was discovered by Klitzing in 1980. The experiment involved measuring the Hall resistance of a silicon-MOSFET at low temperatures

and with a strong magnetic fields [2]. From classical physics one expects that the increase of the Hall voltage is continuous as a function of increasing magnetic field. Surprisingly, it was discovered that the Hall resistance increased in quantized steps. This quantization is universal in the sense that it does not, to a large extent, depend on macroscopic details like the exact value of the magnetic field. It is rather a property of the topology of the system. The Hall current can be interpreted as carried out by chiral edge modes flowing unidirectionally on the boundary. This is a manifestation of the hallmark of topological phases in physics, namely the *bulk boundary correspondence*. The signatures of topological phases can be observed on the boundary. The discovery of the quantum Hall effect earned Klitzing the Nobel prize in 1985. Later, in 2016, the Nobel prize was awarded to Haldane, Thouless and Klosterlitz for theoretical discoveries of topological phase transitions and topological phases of matter emphasizing the relevance of the field to this day showcased by the intensified experimental and theoretical research including topological Dirac and Weyl semimetals [3–6], topological superconductors [7], and higher order topological phases [8–11].

The inherent robustness of topological phases can be harnessed to transport particles or quantum states with high fidelity. This typically involves adiabatic parameter cycles yielding transport protected by a topological invariant, called topological pumping, or adiabatically connecting topological zero energy edge modes of topological models, called robust quantum state transfer. These transport mechanisms can be coined under the common term, topological transport. The robustness of topological transport arises from mathematical symmetries, such as inversion or time-reversal symmetry, and has already been exploited for the fabrication of more robust devices [12, 13] and the establishment of physical standards [14]. The first experimental realization of quantized topological pumping was achieved using cold atoms in optical superlattices [15, 16] and has later been observed in electromechanical [17, 18] and open systems [19, 20]. The robust transfer of edge modes has been demonstrated in quasi-crystalline structures using photonic waveguide arrays [21, 22].

1.2 Many-body quantum optics

The interactions between matter and electromagnetic radiation is of fundamental interest. A typical scenario to consider is a set of emitters, such as atoms, molecules or nanoparticles, coupled to a common environment, where energy and information can leak out to the surrounding environment. For simplicity, let us now consider atoms. The distinctive feature of such systems is that if the

atoms are brought sufficiently close together the action of one atom will affect the other atoms, i.e. the ensemble displays a collective behaviour. The collective behaviour can be split into two prominent features. The first is the induced coherent dipole-dipole exchange interactions. An atom initially excited can exchange a virtual photon with another atom. The second is incoherent dissipation where atoms lose excitations to the surrounding environment. The rate of dissipation can either be faster or slower than the spontaneous decay of the single atoms depending on the specific atomic setup and environment highlighting the collective behaviour called *super-* and *subradiance* respectively. Superradiance was first theoretically postulated by Dicke in the 1950s, with the observation of spontaneous decay from a dense atomic gas, that occurred on a much higher rate than the single atom decay rate [23]. Superradiance has later been verified in experiments involving a range of systems from quantum dots [24, 25] to cavity QED setups [26, 27] and Bose-Einstein condensates [28, 29]. Subradiance was first experimentally verified by Pavolini et. al. around 30 years after the seminal work by Dicke [30]. The collective behaviour of atoms coupled to a common environment has been harnessed in a variety of theoretical applications including subradiance-protected excitation transport [31], subradiant photon storage [32], and in the experimental realization of coherent emission [33].

The rates associated with the dipole-dipole exchange interaction and dissipation can be modified via the specific choice of the environment and its boundary conditions, which may be tailored in order to obtain desirable properties. For example, introducing a dielectric or metallic structure in close proximity to an atomic gas, modifies the local electromagnetic spectrum and hence the collective behaviour of the ensemble [34–38]. This effect was noticed by Purcell in 1950 [39] and has later been verified in various experiments involving atoms or electrons in cavities, and molecules coupled to dielectric structures [40–43].

Among these structures, so-called nanophotonic waveguides, such as single mode optical nanofibers [44, 45] or integrated photonic nanostructures [46–49], particularly stand out since they provide strong and homogenous coupling between the atoms and long coherence times [50], and also due to the confined or guided field modes carried by these nanostructures, which can lead to propagation-direction-dependent (chiral) emission [51]. The translationally invariant nature of these guided modes gives rise to infinitely ranged coherent dipole-dipole interactions and incoherent couplings between the atoms. These all-to-all interactions have recently facilitated, for example, the observation of super- and subradiance [52–54], the realization of long-lived photon storage and multiple photon bound states [55–59] and the investigation of new dynamical phases and phase transitions [60, 61]. The modes propagating in the space out-

side of the nanostructure are often referred to as radiation or unguided modes. Unfortunately, since these modes can propagate in any direction in space, their contribution to the coherent and incoherent interactions between the atoms is highly non-trivial, containing, for example, frequency integrals that either converge very slowly or not at all. Hence, they are often approximated by the free-space modes [53, 62], an approximation that, however, inevitably breaks down when the atoms are close to the nanostructure. A number of works have nicely provided expressions for these contributions in terms of complex integration contours or calculated them numerically under strong approximations, like low-frequency cut-offs [55, 63–65]. Up to now, how to compute these contributions exactly remains an open challenge, but something that will be tackled in this work.

1.3 Topology in quantum optics

The concept of symmetries and topology is deeply connected. Historically, the majority of research within topological physics was focused on condensed matter systems owing to the natural symmetries in crystalline structures. Here, the topological lattice models like the Su–Schrieffer–Heeger (SSH) model in 1D and Haldane model in 2D involves short-range hopping of particles on the lattice. In recent years, many-body quantum optical systems have been explored as a platform for studying topological phases and related topological phenomena. In these systems, the induced dipole-dipole exchange interactions between emitters can be interpreted as hopping parameters, and the system can either be mapped to known topological lattice models or applied to investigate new topological phenomena. Here, the excitations act as particles and the emitters as lattice sites. The benefit of quantum optics as a platform for studying topological phases is the high degree of control of the system parameters, which can be tuned by for example changing the interatomic distances or by coupling emitter lattice systems to structured environments to tailor the dipole-dipole exchange interaction in order to reach desired coupling strengths and range. Topological phenomena like flat bands and chiral edge currents have been demonstrated in 2D lattices of atoms in free space [66, 67] and in emitter arrays coupled to nanophotonic crystals [68, 69]. Furthermore, topological edge states have been observed in a 1D emitter chain coupled to a nanophotonic waveguide [70, 71] and in multimode cavities [72]. Since many-body quantum optical systems naturally display long-range interactions breaking from the typical topological models with nearest neighbour hopping, topological phases with long-range or even all-

to-all hoppings can be studied where little is known about the fate of topological properties. Recent works indicate that the effect of such long-ranged character varies from system to system [73–76].

The collective nature of the interactions and dissipation enables subradiant long-lived topological phases where the dynamics are not affected by dissipation. Remarkably however, it is even found that dissipation itself can induce topological phases where the dissipation provides a targeted cooling into topological phases starting from arbitrary initial states [77–79]. Dissipatively induced two-dimensional Chern insulator states have also been demonstrated with topological transport properties such as persistent currents in the steady state [80].

Rydberg atoms have proven to be a promising platform to study topological features in quantum optics systems due to their high controllability, long lifetimes and strong dipolar interactions. The strong dipolar interactions decays with the distance cubed, enabling an approximate mapping to existing nearest neighbour topological models such as the SSH model. The edge modes of the SSH model have been experimentally observed in a Rydberg lattice array by Léséleuc et. al. with ^{87}Rb atoms individually trapped in an array of optical tweezers and excited into Rydberg states giving rise to dipole-dipole exchange interactions acting as effective hopping [81]. Symmetry protected topological phases and topological edge states have also been observed in Rydberg glasses [82] and in Rydberg synthetic dimensions [83]. Recent advances in creating large and controllable two and three-dimensional arrays with individually trapped Rydberg atoms [84–86] has facilitated the potential study of higher dimensional topological physics. Edge states have been theoretically predicted in a 2D honeycomb lattice with three level Rydberg atoms [87]. However, there are still many open questions regarding higher order topological phases in quantum optics systems.

The goal of this thesis is to broaden the understanding of topological phenomena in quantum many-body optical systems and investigate the consequence of long-range interactions in topological systems. In particular, we will study robust topological transport mechanisms in quantum optical systems from short-range couplings achieved in Rydberg systems to all-to-all couplings in atom-waveguide systems in order to achieve high fidelity transport of a photon embedded in the atomic system. Furthermore, we will investigate the realization of higher dimensional topological phases in Rydberg arrays and address if existing phenomena in condensed matter systems like weak topological insulators, higher order topological insulators and semimetallic phases can be achieved in quantum optical systems.

1.4 Structure of the thesis

The thesis will be structured as follows. In Chapter 2 we will introduce the necessary tools to understand and study many-body atomic systems coupled to a common environment through the quantum optical master equation. Furthermore, we introduce the three systems that will constitute the platforms implemented in this work, namely atoms in low-lying states in free space, Rydberg atoms and atoms coupled to a nanophotonic waveguide. In Chapter 3 we outline the basics concepts of topological phases in physics. In particular, we introduce the theory behind topological transport, namely topological pumping and robust quantum state transfer. In Chapters 4-6 we present the original results obtained in this work. In Chapter 4 we present how to calculate the modified dipole-dipole interactions between emitters in the presence of a nanophotonic waveguide with a focus on the non-trivial calculation of the contribution from radiation modes [88]. In Chapter 5 we demonstrate high fidelity topological pumping in the three systems mentioned above and address the fate of topological transport with long-range interactions [89]. In Chapter 6 we propose a 2D topological model with Rydberg atoms with zero Berry curvature. Finally, in Chapter 7 we provide a conclusion and discuss potential further directions of the work.

Chapter 2

The quantum master equation and quantum electrodynamics

Contrary to closed systems, open quantum systems do not follow a unitary evolution. For open quantum system it is hence useful to consider the dynamics in terms of the systems density matrix. The dynamics of the density matrix is governed by the so called quantum master equation. In this chapter we will introduce the quantum optical master equation for two-level systems coupled to a common environment. As there are already various derivations of the quantum optical master equation available [90–92], we will not provide a derivation here, but rather briefly describe the approximations used and their validity in the systems considered in this thesis. Then we will introduce the electromagnetic Green’s tensor, which is the central object that determines the coefficients in the master equation. We derive the Green’s tensor in free space before deriving integral expressions for the Green’s tensor for a cylindrical waveguide by eigenmode decomposition. Finally, we will briefly discuss the physics of Rydberg atoms before closing the chapter by introducing an approximation that allows us to solve the quantum optical master equation for large number of emitters, the single excitation approximation.

2.1 The Quantum Optical Master Equation

In this section we will introduce the so called quantum optical master equation, which governs the dynamics of a many-body two-level system coupled to some common environment. Here, we will consider a general system made up of two parts as illustrated in Figure 2.1. First, an atomic system consisting of N identical two-level emitters with spatial coordinates given by \mathbf{r}_α with α denoting the α -th emitter. The two-level emitters have a ground and excited state denoted

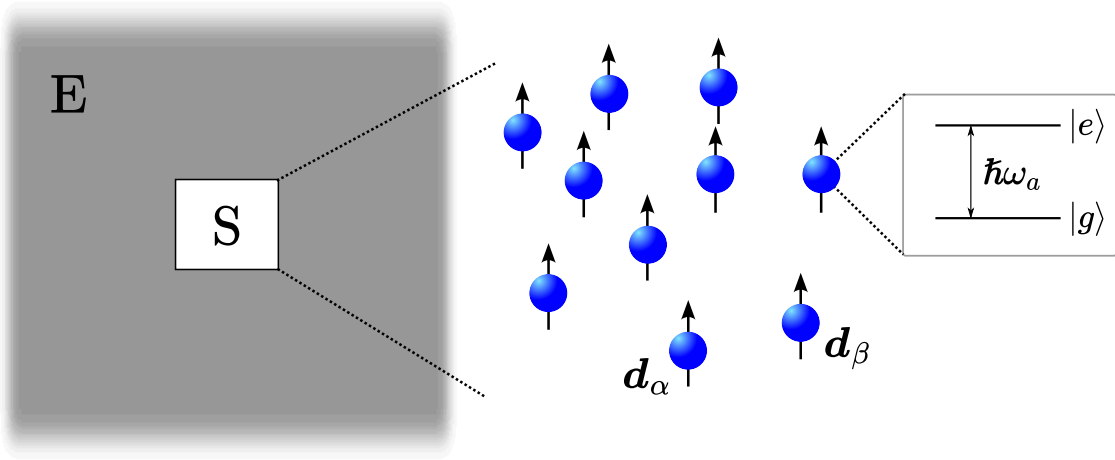


Figure 2.1: *Atomic system coupled to common environment.* An atomic system denoted by S consisting of two level emitters with excited state $|e\rangle$ and ground state $|g\rangle$ separated by an energy $\hbar\omega_a$ coupled to a large common environment E .

by $|g\rangle$ and $|e\rangle$ respectively separated by an energy $\hbar\omega_a$, where $\omega_a = 2\pi c/\lambda_a$ is the transition frequency and λ_a is the transition wavelength.

The atomic system is coupled to a common environment that consists of an electromagnetic field. The form of the electromagnetic field depends on the specific medium that constitutes the environment and can in general be described by the permittivity $\epsilon(\mathbf{r}, \omega)$. We assume that the atomic system resides in free space, but the surrounding electric field can be modified by the presence of some object with permittivity, which differs from the free space value ϵ_0 .

The dynamics of the reduced density matrix $\hat{\rho}_S$, which contains only the internal degrees of freedom of the emitters, is determined by the master equation

$$\dot{\hat{\rho}}_S = i \sum_{\alpha \neq \beta} V_{\alpha\beta} [\hat{\sigma}_\alpha^\dagger \hat{\sigma}_\beta, \hat{\rho}_S] + \sum_{\alpha, \beta} \Gamma_{\alpha\beta} \left(\hat{\sigma}_\beta \hat{\rho}_S \hat{\sigma}_\alpha^\dagger - \frac{1}{2} \{ \hat{\sigma}_\alpha^\dagger \hat{\sigma}_\beta, \hat{\rho}_S \} \right), \quad (2.1)$$

where $\hat{\sigma}_\alpha = |g_\alpha\rangle\langle e_\alpha|$ is the spin-1/2 ladder operator for the α -th emitter. The first part of the master equation describes the coherent dipole-dipole interaction or exchange interaction between the emitters via the exchange of virtual photons. The strength of the interaction is given by the magnitude of the coefficient $V_{\alpha\beta}$. The second part of the equation describes incoherent photon emission or dissipation in the system, which in general possesses a collective character. The diagonal terms of the coefficients $\Gamma_{\alpha\beta}$ are the single emitter spontaneous decay rate, while the off-diagonal elements, for $\alpha \neq \beta$, are responsible for the collective character of the emission.

The exact form of the coefficients $V_{\alpha\beta}$ and $\Gamma_{\alpha\beta}$ depends on the specific envir-

onment. The dependence of the environment can be encoded in the so-called *electromagnetic Green's tensor* \bar{G}

$$\begin{aligned} V_{\alpha\beta} &= \frac{\omega_a^2}{\hbar\epsilon_0 c^2} \mathbf{d}_\alpha^* \text{Re}\{\bar{G}(\mathbf{r}_\alpha, \mathbf{r}_\beta, \omega_a)\} \mathbf{d}_\beta^T, \\ \Gamma_{\alpha\beta} &= \frac{2\omega_a^2}{\hbar\epsilon_0 c^2} \mathbf{d}_\alpha^* \text{Im}\{\bar{G}(\mathbf{r}_\alpha, \mathbf{r}_\beta, \omega_a)\} \mathbf{d}_\beta^T, \end{aligned} \quad (2.2)$$

where \mathbf{d}_α is the transition dipole moment between the ground and excited state of emitter α [37, 38, 91]. In general, the transition dipole moment is a complex vector, which takes the phase factors of the two states into account. The direction of the vector determines how the system interacts with electromagnetic waves of a specific polarization, while the magnitude describes the strength of the interaction. The collective jump operators and rates can be found by diagonalizing the matrix $\Gamma_{\alpha\beta}$, such that

$$\Gamma \hat{a}_k = \sum_{\alpha\beta} M_{k\alpha} \Gamma_{\alpha\beta} M_{\beta k}^*, \quad (2.3)$$

are the decay rates and

$$\hat{J}_k = \sum_\alpha M_{k\alpha} \hat{\sigma}_\alpha, \quad (2.4)$$

are the jump operators. In general, the jump operators are superpositions of all single atom spin operators $\hat{\sigma}_\alpha$. When the off-diagonal elements of $\Gamma_{\alpha\beta}$ are small compared to the diagonal ones, the decay rates are $\Gamma \hat{a}_k \approx \Gamma_{\alpha\alpha}$. However, if the off-diagonal elements are comparable to the diagonal, the rates can be larger or smaller than the single atom decay rate, called superradiant or subradiant respectively.

Casting the quantum optical master equation in Lindblad form (2.1) with coefficients given in equation (2.2) relies on utilizing a set of approximations. In the following, we will outline the different approximations and on which assumptions they are based.

Dipole Approximation

Consider an emitter, which center is located in $\mathbf{r} = 0$ with a surrounding electric field $\mathbf{E}(\mathbf{r}, t)$. The dipole-approximation assumes that the variation of the electric field over the emitter's spatial extension is negligible such that we can make an expansion of the electric field in \mathbf{r} and keep only the lowest order term, resulting in a linear coupling (dipolar coupling) between the electric field and the emitter [93]. This assumption is valid if the wavelength of the electromagnetic field is much larger than the atomic length scale allowing us to expand the electric field in powers of \mathbf{r} and only keep the lowest order. Increasing the size of the

emitters, the approximation breaks down and inclusion of higher order multipole couplings in the electric field expansion is needed. This leads to additional terms in the coefficients $V_{\alpha\beta}$ and $\Gamma_{\alpha\beta}$, which includes terms of first and second derivatives of the Green's tensor [94]. In this thesis we consider atoms in low lying states and Rydberg atoms. Rydberg atoms have a large spatial extension due to the highly excited valence electron. However, the transition wavelength between two Rydberg states considering for example Rubidium, are typically in the millimeter range [95], much larger than the size of the Rydberg atom such that the dipole approximation still holds.

Born approximation

The Born approximation assumes that the coupling between the emitters and the common environment is weak such that it can be treated as a perturbation. Since the coupling is weak, the system's influence on the environment is negligible, such that the system and environment are non-correlated during the entire time evolution. The density matrix for the total system $\hat{\rho}$ at time t can then be expressed through a tensor product

$$\hat{\rho}(t) = \hat{\rho}_S(t) \otimes \hat{\rho}_E$$

where $\hat{\rho}_S$ is the density matrix of the atomic system and $\hat{\rho}_E$ is the density matrix of the environment [90,92].

Markov approximation

The Markov approximation assumes that the timescales of correlations between the atomic system and the environment are much shorter than the typical timescales in which the state of the atomic system changes [96]. This is, as in the case of the Born approximation, a result of weak coupling between the atomic system and the environment, which is why the two approximations often are grouped under the term Born-Markov approximation. If the system is said to be Markovian, the dynamics will only depend on the current time t and not on previous times, i.e. there are no memory effects.

Secular approximation

The secular approximation involves averaging out fast oscillating terms [90]. The fast oscillating terms happen on timescales $\delta t < 1/\omega_a$, where ω_a is the transition frequency. These fast oscillating terms are not expected to contribute to the

dynamics as the transition frequencies are much larger than the typical timescales of the system [97].

2.2 The electromagnetic Green's tensor

The Green's tensor formalism is a powerful tool for analysing systems described by the macroscopic Maxwell equations and is the central object to calculate the coefficients in the quantum optical master equation (2.1). The electromagnetic Green's tensor describes how the electric field with frequency ω propagates from a point-like source located at \mathbf{r} to a position \mathbf{r}' . The Green's tensor is defined as the solution to the equation [98]

$$[k^2\epsilon(\mathbf{r}, \omega) - \nabla \times \nabla \times] \bar{G}(\mathbf{r}, \mathbf{r}', \omega) = -\mathbb{1}\delta(\mathbf{r} - \mathbf{r}'), \quad (2.5)$$

where $k = \omega/c$ and $\epsilon(\mathbf{r}, \omega)$ is the relative electric permittivity dependent on the specific media and/or the arrangement of absorbing and dispersing electric bodies, and with boundary conditions

$$\lim_{|\mathbf{r} - \mathbf{r}'| \rightarrow \infty} \bar{G}(\mathbf{r}, \mathbf{r}', \omega) = 0.$$

The Green's tensor satisfies both the Schwarz reflection principle

$$\bar{G}^*(\mathbf{r}, \mathbf{r}', \omega) = \bar{G}(\mathbf{r}, \mathbf{r}', -\omega^*),$$

and the Onsager reciprocity [99]

$$\bar{G}^T(\mathbf{r}, \mathbf{r}', \omega) = \bar{G}(\mathbf{r}', \mathbf{r}, \omega).$$

In order to find the coefficients of the master equation (2.1) both the real and imaginary part of the Green's tensor is needed. To relate the real and imaginary part of the Green's tensor, the Kramers-Kronig relation can be applied. The application of the Kramers-Kronig relation to a complex function $\chi(\omega)$ requires that the function satisfies two conditions. The function has to converge to a finite value as $|\omega| \rightarrow \infty$ in the upper half plane and the function has to be holomorphic in the upper half plane, i.e. the function contains no poles in the complex upper half plane.

The Green's tensor converges as $|\omega| \rightarrow \infty$ in the upper half plane satisfying the former condition of the Kramers-Kronig relation. However, the Green's tensor can have poles on the real line at $\omega = 0$, making it non-holomorphic in general. However by multiplying the Green's tensor by ω^2 , the small and large

frequency limits may be applied [100]

$$\lim_{|\omega| \rightarrow 0} \frac{\omega^2}{c^2} \bar{G}(\mathbf{r}, \mathbf{r}', \omega) = -\mathbb{1}\delta(\mathbf{r} - \mathbf{r}'),$$

$$\lim_{|\omega| \rightarrow \infty} \frac{\omega^2}{c^2} \bar{G}(\mathbf{r}, \mathbf{r}', \omega) = \bar{M},$$

where the components of \bar{M} are $M_{ij} < \infty$, which is exactly the Kramers-Kronig conditions. Therefore, the Kramers-Kronig relation may always be applied to the function $\omega^2 \bar{G}(\mathbf{r}, \mathbf{r}', \omega)$, but not always to the Green's tensor itself.

However, the singular part of the Green's tensor at $\omega = 0$ may be isolated by decomposing the Green's tensor into its transverse and longitudinal components

$$\bar{G}(\mathbf{r}, \mathbf{r}', \omega) = \bar{G}^\perp(\mathbf{r}, \mathbf{r}', \omega) + \bar{G}^\parallel(\mathbf{r}, \mathbf{r}', \omega).$$

The transverse Green's tensor is in general holomorphic in the complex upper half-plane including the real line and hence satisfies the conditions for the Kramers-Kronig relation, while the longitudinal part is singular in $\omega = 0$. The transverse and longitudinal part of the Green's tensor may be found by means of the transverse and longitudinal projection operators [101, 102]

$$\bar{G}^\perp(\mathbf{k}, \omega) = \bar{\Pi}^\perp \bar{G}(\mathbf{k}, \omega) \bar{\Pi}^\perp,$$

$$\bar{G}^\parallel(\mathbf{k}, \omega) = \bar{\Pi}^\parallel \bar{G}(\mathbf{k}, \omega) \bar{\Pi}^\parallel,$$

where the projection operators are defined as

$$\bar{\Pi}_{ij}^\perp = \delta_{ij} - \frac{k_i k_j}{|\mathbf{k}|^2}, \quad \bar{\Pi}_{ij}^\parallel = \frac{k_i k_j}{|\mathbf{k}|^2}.$$

In cases without a uniform dielectric distribution or involving complex geometries, a direct solution of equation (2.5) is non-trivial. In such cases employing the trick of eigenmode decomposition can be useful. Consider the positive frequency part of the electric field $\mathbf{E}(\mathbf{r}, \omega)$. From classical electromagnetism the positive frequency part of the electric field is the solution to the equation

$$[k^2 \epsilon(\mathbf{r}, \omega) - \nabla \times \nabla \times] \mathbf{E}(\mathbf{r}, \omega) = -i\omega \mu_0 \mathbf{j}_T(\mathbf{r}, \omega),$$

where μ_0 is the permeability in free space and $\mathbf{j}_T(\mathbf{r}, \omega)$ is the transverse current density. It is convenient to introduce the vector function $\mathbf{g}(\mathbf{r}, \omega) = \sqrt{\epsilon(\mathbf{r}, \omega)} \mathbf{E}(\mathbf{r}, \omega)$,

which is the solution to

$$\mathcal{H}g(\mathbf{r}, \omega) = -i\omega\mu_0 \frac{\mathbf{j}_T(\mathbf{r}, \omega)}{\sqrt{\epsilon(\mathbf{r}, \omega)}},$$

where we have defined the hermitian differential operator $\mathcal{H}g(\mathbf{r}, \omega) = [k^2 - \frac{1}{\epsilon(\mathbf{r}, \omega)} \nabla \times \nabla \times]g(\mathbf{r}, \omega)$, assuming that the permittivity is a real function. Now we can define a set of solutions $\{g_n, \lambda_n\}$ to the eigenvalue problem $\mathcal{H}g_n = \lambda_n g_n$. Since the operator \mathcal{H} is hermitian, there exists a set of eigensolutions $\{g_n^\dagger, \lambda_n^*\}$ to $g_n^\dagger \mathcal{H} = \lambda_n^* g_n^\dagger$ such that the orthogonality and completeness relations

$$\begin{aligned} \int g_n^\dagger(\mathbf{r}, \omega) \cdot g_m(\mathbf{r}, \omega) d^3r &= \delta_{nm}, \\ \sum_n g_n(\mathbf{r}, \omega) g_n^\dagger(\mathbf{r}', \omega) &= \mathbb{I}\delta(\mathbf{r} - \mathbf{r}'), \end{aligned} \quad (2.6)$$

are satisfied [103, 104]. We can define a Green's tensor $\bar{G}_g(\mathbf{r}, \mathbf{r}', \omega)$ for the function $g(\mathbf{r}, \omega)$, which satisfies

$$g(\mathbf{r}, \omega) = -i\omega\mu_0 \int d\mathbf{r}' \bar{G}_g(\mathbf{r}, \mathbf{r}', \omega) \frac{\mathbf{j}_T(\mathbf{r}', \omega)}{\sqrt{\epsilon(\mathbf{r}', \omega)}}.$$

Using the relations in equation (2.6), the Green's tensor $\bar{G}_g(\mathbf{r}, \mathbf{r}', \omega)$ can be expressed as

$$\bar{G}_g(\mathbf{r}, \mathbf{r}', \omega) = \sum_n \frac{g_n(\mathbf{r}, \omega) g_n^\dagger(\mathbf{r}', \omega)}{\lambda_n}.$$

Finally, by considering the relation between the vector function $g(\mathbf{r}, \omega)$ and the electric field, the Green's tensor for the electromagnetic field may be expressed as

$$\bar{G}(\mathbf{r}, \mathbf{r}', \omega) = \sum_n \frac{\mathbf{E}_n(\mathbf{r}, \omega) \mathbf{E}_n^\dagger(\mathbf{r}', \omega)}{\lambda_n}, \quad (2.7)$$

where $\mathbf{E}_n(\mathbf{r}, \omega)$ are the eigenmodes of the eigenvalue problem

$$[k^2 - \frac{1}{\epsilon(\mathbf{r}, \omega)} \nabla \times \nabla \times] \mathbf{E}_n(\mathbf{r}, \omega) = \lambda_n \mathbf{E}_n(\mathbf{r}, \omega). \quad (2.8)$$

This reduces the tensor equation (2.5) to an eigenvalue problem.

2.2.1 Green's tensor in free space

In free space the relative permittivity is $\epsilon(\mathbf{r}, \omega) = 1$ simplifying equation (2.5)

$$[k^2 - \nabla \times \nabla \times] \bar{G}^{(0)}(\mathbf{r}, \mathbf{r}', \omega) = -\mathbb{I}\delta(\mathbf{r} - \mathbf{r}'). \quad (2.9)$$

Taking the divergence on both sides

$$k^2 \nabla \cdot \bar{G}^{(0)}(\mathbf{r}, \mathbf{r}', \omega) = -\nabla \delta(\mathbf{r} - \mathbf{r}'). \quad (2.10)$$

Inserting the relation (2.10) in equation (2.9) and using the vector identity $\nabla \times \nabla \times \mathbf{A} = \nabla(\nabla \cdot \mathbf{A}) - \nabla^2 \mathbf{A}$, the equation for the Green's tensor may be written as

$$[\nabla^2 + k^2] \bar{G}^{(0)}(\mathbf{r}, \mathbf{r}', \omega) = - \left[\mathbb{1} + \frac{1}{k^2} \nabla \nabla \right] \delta(\mathbf{r} - \mathbf{r}').$$

In order to simplify the problem we define the Green's function $g^{(0)}$ of the operator $[\nabla^2 + k^2]$, which is the solution to the equation

$$[\nabla^2 + k^2] g^{(0)}(\mathbf{r}, \mathbf{r}', \omega) = -\delta(\mathbf{r} - \mathbf{r}'). \quad (2.11)$$

Note that $g^{(0)}$ is a scalar function. The Green's function $g^{(0)}$ is related to the full Green's tensor of the problem through the equation

$$\bar{G}^{(0)}(\mathbf{r}, \mathbf{r}', \omega) = \left[\mathbb{1} + \frac{1}{k^2} \nabla \nabla \right] g^{(0)}(\mathbf{r}, \mathbf{r}', \omega). \quad (2.12)$$

The solution for $g^{(0)}$ can be found by making a Fourier transform of equation (2.11)

$$\frac{1}{(2\pi)^3} \int [\nabla^2 + k^2] g^{(0)}(\mathbf{r}, \mathbf{r}', \omega) e^{-i\kappa \cdot \rho} d^3 \rho = -1, \quad (2.13)$$

where we have defined the relative coordinate $\rho = \mathbf{r} - \mathbf{r}'$. Equation (2.13) can be rewritten in terms of $\mathcal{G}^{(0)}$, the Fourier transform of $g^{(0)}$

$$-\kappa^2 \mathcal{G}^{(0)}(\kappa, \omega) + k^2 \mathcal{G}^{(0)}(\kappa, \omega) = -1.$$

Solving for $\mathcal{G}^{(0)}$ we find

$$\mathcal{G}^{(0)} = -\frac{1}{k^2 - \kappa^2}. \quad (2.14)$$

To find the real space solution of the Green's function we take the inverse Fourier transform of equation (2.14)

$$\begin{aligned} g^{(0)}(\mathbf{r}, \mathbf{r}', \omega) &= \frac{1}{(2\pi)^3} \int d^3 \kappa \mathcal{G}^{(0)}(\kappa, \omega) e^{-i\kappa \cdot \rho} \\ &= -\frac{1}{(2\pi)^3} \int_0^{2\pi} d\phi \int_{-1}^1 d(\cos \theta) \int_0^\infty d\kappa \kappa^2 \frac{1}{k^2 - \kappa^2} e^{-i\kappa \rho \cos \theta}. \end{aligned}$$

Carrying out the integration over the angles ϕ and θ , the expression simplifies to

$$g^{(0)}(\rho, \omega) = -\frac{i}{(2\pi)^2 \rho} \int_{-\infty}^{\infty} d\kappa \kappa \frac{e^{i\kappa\rho}}{k^2 - \kappa^2}.$$

Using methods of contour integration gives the solution

$$g^{(0)}(\rho, \omega) = \frac{e^{ik\rho}}{4\pi\rho}.$$

The full Green's tensor of the system may now be found by using the relation in equation (2.12)

$$\bar{G}^{(0)}(\mathbf{r}, \mathbf{r}', \omega) = \frac{k}{4\pi} e^{ik\rho} \left[(3\hat{\rho}^2 - \mathbb{1}) \left(\frac{1}{(k\rho)^3} - \frac{i}{(k\rho)^2} \right) + (\mathbb{1} - \hat{\rho}^2) \frac{1}{k\rho} \right], \quad (2.15)$$

where $\hat{\rho} = \rho/\rho$ and $\rho = |\rho|$. The tensor $\hat{\rho}^2$ should be interpreted as $\hat{\rho}\hat{\rho}^T$. Using the projection operators in equation (2.2), the longitudinal and transverse components of the free space Green's tensor may be expressed as

$$\bar{G}^{0\parallel}(\mathbf{r}, \mathbf{r}', \omega) = (3\hat{\rho}^2 - \mathbb{1}) \frac{1}{4\pi\rho^3 k^2}, \quad (2.16)$$

$$\begin{aligned} \bar{G}^{0\perp}(\mathbf{r}, \mathbf{r}', \omega) &= \frac{ke^{ik\rho}}{4\pi} \left\{ (3\hat{\rho}^2 - \mathbb{1}) \left[\frac{1}{(k\rho)^3} - \frac{i}{(k\rho)^2} \right] \right. \\ &\quad \left. + (\mathbb{1} - \hat{\rho}^2) \frac{1}{k\rho} \right\} - (3\hat{\rho}^2 - \mathbb{1}) \frac{1}{4\pi\rho^3 k^2}, \end{aligned} \quad (2.17)$$

where the divergence of the longitudinal Green's tensor at $\omega = 0$ can clearly be seen.

The collective coefficients in free space may now be easily calculated from equation (2.2) taking the real and imaginary part of the Green's tensor in equation (2.15) evaluated at the transition frequency $\omega_a = k_a c$

$$\begin{aligned} \Gamma_{\alpha\beta} &= \frac{3\gamma}{2} \left[j_0(k_a r_{\alpha\beta}) - \frac{j_1(k_a r_{\alpha\beta})}{k_a r_{\alpha\beta}} + j_2(k_a r_{\alpha\beta})(\hat{\mathbf{d}} \cdot \hat{\mathbf{r}}_{\alpha\beta})^2 \right], \\ V_{\alpha\beta} &= \frac{3\gamma}{4} \left[y_0(k_a r_{\alpha\beta}) - \frac{y_1(k_a r_{\alpha\beta})}{k_a r_{\alpha\beta}} + y_2(k_a r_{\alpha\beta})(\hat{\mathbf{d}} \cdot \hat{\mathbf{r}}_{\alpha\beta})^2 \right], \end{aligned} \quad (2.18)$$

where j_n and y_n are the spherical Bessel functions of the first and second kind respectively and $\gamma = \frac{d^2 k_a^3}{3\pi\epsilon_0\hbar}$ is the single-atom spontaneous decay rate in free space. The dipole-dipole interaction and decay rate for two different dipole orientations are shown in Figure 2.2. For dipoles perpendicular to the separation vector (blue line), the dipole-dipole interactions decay as $\frac{1}{r_{\alpha\beta}}$ for large $r_{\alpha\beta}$ underlining the long-

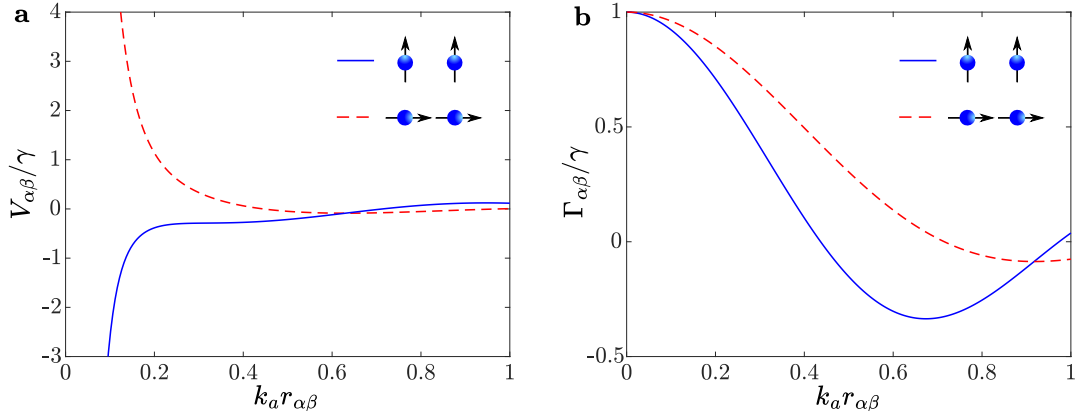


Figure 2.2: *Dipole-dipole interaction and decay rate in free space.* Dipole-dipole interaction (a) and decay rate (b) in free space as a function of the dimensionless separation $k_a r_{\alpha\beta}$ for different dipole orientations.

range character of the interactions. For dipoles parallel to the separation vector (red dashed line), the leading term of the dipole-dipole interactions decay as $\frac{1}{r_{\alpha\beta}^2}$ for large $r_{\alpha\beta}$. When the nearest neighbour interatomic distance is comparable to the transition wavelength $\lambda_a = \frac{2\pi}{k_a}$ the dissipation displays a collective character and superradiant and subradiant modes can be found.

2.2.2 Green's tensor for a cylindrical waveguide

Lets now consider the free space environment is modified by the presence of a cylindrical fiber waveguide with radius r_f and refractive index n_1 , placed along $r = 0$ in a cylindrical coordinate system (r, ϕ, z) and extended in the z -direction as depicted in Figure 2.3. The waveguide medium is characterized by a refractive index n_1 . In this case a direct solution of the Green's tensor from equation (2.5) is highly non-trivial, however, a solution can be found using eigenmode decomposition, expressing the Green's tensor in terms of sums or integrals over the electromagnetic field modes.

The waveguide can support a set of modes of the electromagnetic field, which are bound inside the fiber called guided modes. The rest of the modes of the electromagnetic field are radiation modes propagating outside of the fiber. However, these modes are also affected by the presence of the fiber. It is useful to separate the guided (μ) and radiation (ν) contributions of the electric field

$$\mathbf{E} = \mathbf{E}^{(\mu)} + \mathbf{E}^{(\nu)}.$$

For simplicity, we will assume that we are in the single-mode regime where the waveguide only supports the fundamental HE₁₁-modes [105]. Note that this is

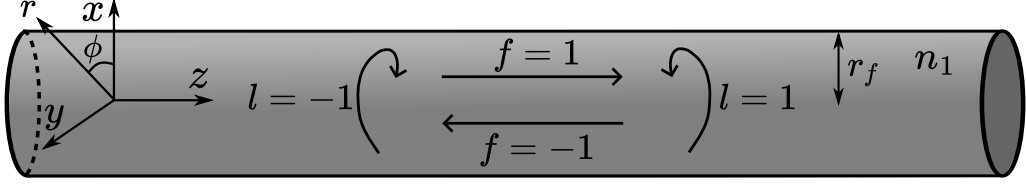


Figure 2.3: *Cylindrical fiber waveguide*. A cylindrical waveguide is centered in $r = 0$ in a cylindrical coordinate system (r, ϕ, z) and extended in the z -direction. The waveguide has a radius r_f and is characterized by a refractive index n_1 . The waveguide supports a set of guided modes of the electromagnetic field that can propagate in the forwards or backwards direction ($f = \pm 1$ respectively) and can be polarized clockwise or counter clockwise ($l = \pm 1$ respectively).

the relevant regime we are interested in for experimental setups. The fundamental guided modes will be labeled by $\mu = (\beta l f)$, where β is the longitudinal propagation constant, $f = \pm 1$ denotes the forward and backwards propagation direction along z and $l = \pm 1$ is the polarization index (+ is the counter clockwise polarization and - is the clockwise polarization), as indicates in Figure 2.3. The radiation modes will be labeled by $\nu = (\omega \beta m l)$ where ω is the mode frequency, β is the longitudinal propagation constant, which may vary continuously from $-k$ to k , where $k = \omega/c$ for each value of ω , $m = 0, \pm 1, \pm 2, \dots$ is the mode order and $l = \pm 1$ is the polarization.

Guided modes

The guided modes of the electric field at a position $\mathbf{r} = (r, \phi, z)$ may be expressed as

$$\mathbf{E}^{(\mu)}(\mathbf{r}) = \mathbf{e}^{(\mu)}(r) e^{il\phi} e^{if\beta z},$$

where β is the guided longitudinal propagation constant and $\mathbf{e}^{(\mu)}(r)$ is the guided profile function of the fiber. The guided modes $\mathbf{E}^{(\mu)}(\mathbf{r})$ are eigenvectors of the Hermitian operator $\mathcal{H} = [k^2 - \frac{1}{\epsilon(\mathbf{r}, \omega)} \nabla \times \nabla \times]$ with eigenvalues $\lambda_{(\mu)} = k'^2 - (\beta^2 - q^2)$, where $k' = \omega'/c$ and ω' is the argument frequency of the guided Green's tensor. Using the eigenmode decomposition technique given in equation (2.7), the Green's tensor for guided modes may be expressed as

$$\bar{G}^{gd}(\mathbf{r}, \mathbf{r}', \omega') = \frac{1}{2\pi} \sum_{fl} \int_0^\infty d\beta \frac{\mathbf{e}^{(\mu)}(\mathbf{r}) \mathbf{e}^{(\mu)\dagger}(\mathbf{r}')}{k'^2 - (\beta^2 - q^2)} e^{il(\phi-\phi')} e^{if\beta(z-z')},$$

where the profile function of a guided mode is

$$\mathbf{e}^{(\mu)}(r) = e_r^{(\mu)}(r) \hat{\mathbf{r}} + e_\phi^{(\mu)}(r) \hat{\boldsymbol{\phi}} + e_z^{(\mu)}(r) \hat{\mathbf{z}},$$

and is normalized

$$\int_0^{2\pi} d\phi \int_0^\infty \epsilon(\mathbf{r}, \omega) |\mathbf{e}^{(\mu)}|^2 r dr = 1.$$

The guided profile function components has the following symmetry relations

$$\begin{aligned} e_r^{(\beta lf)} &= e_r^{(\beta l-f)} = e_r^{(\beta-lf)}, \\ e_\phi^{(\beta lf)} &= e_\phi^{(\beta l-f)} = -e_\phi^{(\beta-lf)}, \\ e_z^{(\beta lf)} &= -e_z^{(\beta l-f)} = e_z^{(\beta-lf)}. \end{aligned}$$

The guided profile functions has components, for $r < r_f$, given by

$$\begin{aligned} e_r^{(\mu)}(r) &= iC \frac{q}{\kappa} \frac{K_1(qr_f)}{J_1(qr_f)} [(1-s)J_0(\kappa r) - (1+s)J_2(\kappa r)], \\ e_\phi^{(\mu)}(r) &= -C \frac{lq}{\kappa} \frac{K_1(qr_f)}{J_1(qr_f)} [(1-s)J_0(\kappa r) + (1+s)J_2(\kappa r)], \\ e_z^{(\mu)}(r) &= C \frac{2fq}{\kappa} \frac{K_1(qr_f)}{J_1(qr_f)} J_1(\kappa r), \end{aligned}$$

and for $r > r_f$

$$\begin{aligned} e_r^{(\mu)}(r) &= iC[(1-s)K_0(qr) + (1+s)K_2(qr)], \\ e_\phi^{(\mu)}(r) &= C[(1+s)K_2(qr) - (1-s)K_0(qr)], \\ e_z^{(\mu)}(r) &= C \frac{2fq}{\beta} K_1(qr). \end{aligned}$$

Here, $\kappa^2 = k^2 n_1^2 - \beta^2$ and $q^2 = \beta^2 - k^2$ characterizes the field inside and outside the fiber respectively. The longitudinal propagation constant β of the fiber may be determined by solving the fiber eigenvalue equation

$$\begin{aligned} \frac{J_0(\kappa r_f)}{\kappa r_f J_1(\kappa r_f)} &= \frac{n_1^2 + 1}{2n_1^2} \frac{K'_1(qr_f)}{qr_f K_1(qr_f)} + \frac{1}{\kappa^2 r_f^2} - \left[\left(\frac{n_1^2 - 1}{2n_1^2} \frac{K'_1(qr_f)}{qr_f K_1(qr_f)} \right)^2 \right. \\ &\quad \left. + \frac{\beta^2}{n_1^2 k^2} \left(\frac{1}{q^2 r_f^2} + \frac{1}{\kappa^2 r_f^2} \right)^2 \right]^{1/2}. \end{aligned}$$

The functions $J_m(x)$ and $K_m(x)$ are the Bessel function of first kind and modified Bessel function of second kind respectively, which have the following form in the

asymptotic limit ($|x| \gg 1$)

$$\begin{aligned} J_m(x) &\approx \sqrt{\frac{2}{\pi x}} \cos\left(x - \frac{m\pi}{2} - \frac{\pi}{4}\right), \\ K_m(x) &\approx \sqrt{\frac{2}{\pi x}} e^{-x}. \end{aligned}$$

The primed Bessel functions are their derivatives $J'_m(x) = \frac{d}{dx}J_m(x)$, $K'_m(x) = \frac{d}{dx}K_m(x)$. Finally, the parameter s is defined as

$$s = \frac{\frac{1}{\kappa^2 r_f^2} + \frac{1}{q^2 r_f^2}}{\frac{J'_1(\kappa r_f)}{\kappa r_f J_1(\kappa r_f)} + \frac{K'_1(q r_f)}{q r_f K_1(q r_f)}}.$$

Radiation modes

The radiation modes of the electric field at position $\mathbf{r} = (r, \phi, z)$ may be expressed as

$$\mathbf{E}^{(\nu)}(\mathbf{r}) = \mathbf{e}^{(\nu)}(r)e^{im\phi}e^{i\beta z}.$$

The electric field modes $\mathbf{E}^{(\nu)}(\mathbf{r})$ are eigenvectors of the Hermitian operator $\mathcal{H} = [k^2 - \frac{1}{\epsilon(\mathbf{r}, \omega)} \nabla \times \nabla \times]$ with eigenvalues $\lambda_{(\nu)} = k'^2 - (\beta^2 + q^2)$, where $k' = \omega'/c$ and ω' is the argument frequency of the radiation Green's tensor. The characteristic momenta of the radiation field inside and outside the fiber are $\kappa^2 = k^2 n_1^2 - \beta^2$ and $q^2 = k^2 - \beta^2$ respectively. Unlike for the guided modes, the variables β and q for the radiation modes are continuous variables for each value of k and may be expressed in terms of an angle θ

$$\beta = k \cos \theta, \quad q = k \sin \theta.$$

The radiation modes of the electric field can be both transverse and longitudinal, and the radiation contribution to the Green's tensor may be decomposed as $\bar{G}^{rd}(\omega) = \bar{G}^{rd\perp}(\omega) + \bar{G}^{rd\parallel}(\omega)$. On the other hand, one can also separate the Green's tensor as a sum of the vacuum modes and the ones scattered by the nanofiber as $\bar{G}^{rd}(\omega) = \bar{G}^0(\omega) + \bar{G}^{sc}(\omega)$. The scattered modes are, however, purely transverse, allowing to replace the longitudinal radiation Green's tensor with the well known longitudinal part of the vacuum Green's tensor and write

$$\bar{G}^{rd}(\mathbf{r}, \mathbf{r}', \omega) = \bar{G}^{rd\perp}(\mathbf{r}, \mathbf{r}', \omega) + \bar{G}^{0\parallel}(\mathbf{r}, \mathbf{r}', \omega).$$

where $\bar{G}^{0\parallel}(\mathbf{r}, \mathbf{r}', \omega)$ is the well known longitudinal part of the vacuum Green's tensor in equation (2.16). Using eigenmode decomposition for the transverse part

of the radiation Green's tensor gives

$$\bar{G}^{rd}(\mathbf{r}, \mathbf{r}', \omega') = \sum_{ml} \int_{-\infty}^{\infty} d\beta \int_0^{\infty} dq \frac{\mathbf{e}^{(\nu)}(\mathbf{r}) \mathbf{e}^{(\nu)\dagger}(\mathbf{r}')}{k'^2 - (\beta^2 + q^2)} e^{im(\phi - \phi')} e^{i\beta(z - z')} + \bar{G}^{0\parallel}(\mathbf{r}, \mathbf{r}', \omega'), \quad (2.19)$$

where the transverse profile function of a radiation mode is

$$\mathbf{e}^{(\nu)}(r) = e_r^{(\nu)}(r) \hat{\mathbf{r}} + e_{\phi}^{(\nu)}(r) \hat{\boldsymbol{\phi}} + e_z^{(\nu)}(r) \hat{\mathbf{z}},$$

and is normalized according to

$$\int_0^{2\pi} d\phi \int_0^{\infty} dr r \epsilon(\mathbf{r}, \omega) [\mathbf{e}^{(\nu)} \cdot \mathbf{e}^{(\nu)*}]_{\beta=\beta', m=m'} = \delta_{ll'} \delta(\omega - \omega').$$

The transverse modes of the radiation electric field satisfy $\nabla \cdot [\epsilon(\mathbf{r}, \omega) \mathbf{E}^{(\nu)}(\mathbf{r})] = 0$, and are characterized by the transverse profile functions $\mathbf{e}^{(\nu)}(r)$ with components in cylindrical coordinates, for $r < r_f$, given by

$$\begin{aligned} e_r^{(\nu)}(r) &= \frac{i\beta}{\kappa} A J'_m(\kappa r) - m \frac{\omega \mu_0}{\kappa^2 r} B J_m(\kappa r), \\ e_{\phi}^{(\nu)}(r) &= -m \frac{\beta}{\kappa^2 r} A J_m(\kappa r) - \frac{i}{\kappa} \omega \mu_0 B J'_m(\kappa r), \\ e_z^{(\nu)}(r) &= A J_m(\kappa r), \end{aligned}$$

and for $r > r_f$

$$\begin{aligned} e_r^{(\nu)}(r) &= \sum_{j=1,2} \frac{i\beta}{q} C_j H_m'^{(j)}(qr) - m \frac{\omega \mu_0}{q^2 r} D_j H_m^{(j)}(qr), \\ e_{\phi}^{(\nu)}(r) &= \sum_{j=1,2} -m \frac{\beta}{q^2 r} C_j H_m^{(j)}(qr) - \frac{i}{q} \omega \mu_0 D_j H_m'^{(j)}(qr), \\ e_z^{(\nu)}(r) &= \sum_{j=1,2} C_j H_m^{(j)}(qr). \end{aligned}$$

The functions $J_m(x)$ and $H_m^{(j)}(x)$ are the Bessel function of first kind and Hankel functions of j -th kind respectively, which takes the following form in the asymptotic limit ($|x| \gg 1$)

$$\begin{aligned} J_m(x) &\approx \sqrt{\frac{2}{\pi x}} \cos \left(x - \frac{m\pi}{2} - \frac{\pi}{4} \right), \\ H_m^{(1)}(x) &\approx \sqrt{\frac{2}{\pi x}} e^{i(x - \frac{m\pi}{2} - \frac{\pi}{4})}, \\ H_m^{(2)}(x) &\approx \sqrt{\frac{2}{\pi x}} e^{-i(x - \frac{m\pi}{2} - \frac{\pi}{4})}. \end{aligned}$$

The coefficients C_j and D_j are related to the coefficients A and B

$$C_j = (-1)^j \frac{i\pi q^2 r_f}{4} (AL_j + i\mu_0 c BV_j),$$

$$D_j = (-1)^{j-1} \frac{i\pi q^2 r_f}{4} (i\epsilon_0 c AV_j - BM_j),$$

where ϵ_0 and μ_0 is the vacuum permittivity and permeability respectively, and

$$V_j = \frac{mk\beta}{r_f \kappa^2 q^2} (1 - n_1^2) J_m(\kappa r_f) H_m^{(j)*}(qr_f),$$

$$M_j = \frac{1}{\kappa} J'_m(\kappa r_f) H_m^{(j)*}(qr_f) - \frac{1}{q} J_m(\kappa r_f) H_m'^{(j)*}(qr_f),$$

$$L_j = \frac{n_1^2}{\kappa} J'_m(\kappa r_f) H_m^{(j)*}(qr_f) - \frac{1}{q} J_m(\kappa r_f) H_m'^{(j)*}(qr_f).$$

By choosing the constant $B = il\eta A$, the normalization of the profile function leads to the equations

$$\eta = \epsilon_0 c \left(\frac{|V_j|^2 + |L_j|^2}{|V_j|^2 + |M_j|^2} \right)^{1/2},$$

and

$$1 = \frac{16\pi^2 k^2}{q^3} \left(|C_j|^2 + \frac{\mu_0}{\epsilon_0} |D_j|^2 \right).$$

In Chapter 4, we aim to solve the integrals in the equation for the guided and radiation Green's tensor to obtain the dipole-dipole interactions between emitters coupled to a nanophotonic waveguide.

2.3 Rydberg atoms

Rydberg atoms are a class of atoms with valence electrons in a highly excited state, i.e. with a high principal quantum number n . The higher quantum number, the farther the electron is from the atom core giving Rydberg atoms extremely large dipole moments resulting in strong dipole-dipole interactions between Rydberg atoms. Rydberg atoms also display remarkable long life-times. These exaggerated properties makes Rydberg atoms highly useful in experiments and for simulating long coherent dynamics.

Atoms excited to Rydberg states interact through strong dipole-dipole interactions even at large distances (in the order of micrometers) due to their large dipole moment d scaling as n^4 . Since the transition frequency between Rydberg states is small compared to atoms in low lying states, we can approximate the dipole-dipole interactions between atoms excited to Rydberg states in free space

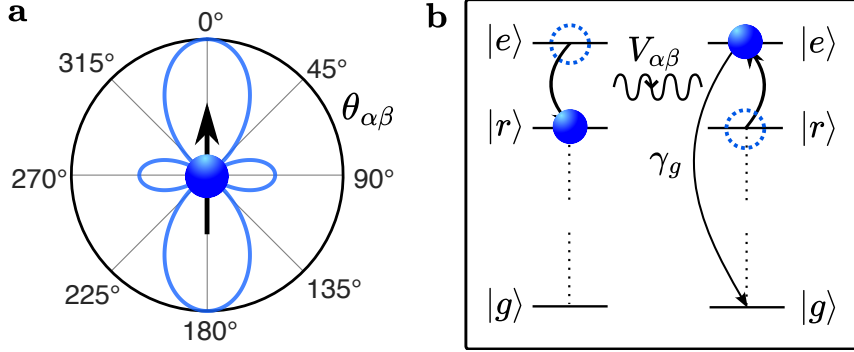


Figure 2.4: *Rydberg atoms.* **a:** The dipole-dipole interaction strength between two Rydberg atoms as a function of the angle $\theta_{\alpha\beta}$. **b:** Two Rydberg atoms excited to Rydberg states $|r\rangle$ and $|e\rangle$ interact via the exchange of a virtual photon with a rate $V_{\alpha\beta}$. The main decay channel is to the ground state $|g\rangle$ given by the decay rate γ_g .

by considering only the leading term of $V_{\alpha\beta}$ for a two level system in (2.18), for $k_ar_{\alpha\beta} \ll 1$

$$V_{\alpha\beta} = \frac{d^2}{4\pi\epsilon_0\hbar} \frac{3\cos^2\theta_{\alpha\beta} - 1}{r_{\alpha\beta}^3}, \quad (2.20)$$

where we have defined $\theta_{\alpha\beta}$ as the angle between the dipole d_α and the separation vector $r_{\alpha\beta}$. The angular dependence of the dipole-dipole interaction is shown in Figure 2.4. The dipole-dipole interaction between Rydberg atoms is many orders of magnitude larger than for atoms in low lying states at the same distance. The strong dipole-dipole interactions makes Rydberg atoms an exceptional platform to study and realize various many-body Hamiltonians [106, 107] and model condensed matter systems, for example topologically non-trivial lattices as will be discussed in Chapter 6.

Doing the same expansion for $k_ar_{\alpha\beta} \ll 1$ for the dissipation matrix, given for a two-level system in equation (2.18), one finds that $\Gamma_{\alpha\beta} = \gamma$. However, Rydberg atoms are not purely two-level systems and the main decay channel for a Rydberg excitation is limited to the spontaneous decay from the Rydberg state to the ground state γ_g as depicted in Figure 2.4. Applying Fermi golden rule one finds that the decay rate γ_g scales as n^{-3} . Hence, Rydberg atoms with high principal quantum numbers have long lifetimes.

Chapter 3

Topology in physics

In this chapter we will review the theory of topology in physics, a concept which has attracted a lot of attention in recent years due to the robust nature of topological phases. We will start by introducing the notion of symmetries, which is the key to characterizing topological phases. We proceed by treating adiabatic evolution and how it leads to one of the central ideas in topology, namely the Berry phase. Subsequently, we introduce a realization of topological phases in 1D, the SSH model, and present one of the distinctive features of topological phases, the bulk-boundary correspondence. Finally, we conclude by establishing the theory of robust adiabatic transport in topological systems in the form of topological pumping and quantum state transfer.

3.1 Characterization of topological phases

In order to determine if a topological phase can be present in a system and if so, how is it characterized, two questions should be asked. What are the symmetries of the system and what is the dimensionality of the system. The concept of symmetries is deeply rooted in the understanding and characterization of topological phases. Although having symmetries is not an absolute requirement for topological phases to exist, many topological phases and effects arise specifically due to particular combination of symmetries of the underlying Hamiltonian [108–110]. In the following, we will discuss four symmetries that will play a crucial role in the classification of topological phases in 1D and 2D systems.

However, before introducing the different symmetries, it is useful to introduce the concept of bulk Hamiltonians. Lattice systems are central in the study of topological phases due to their inherent symmetries. Every lattice system has a bulk and a boundary. If the lattice is large, i.e. approaching the thermodynamic limit where the number of particles $N \rightarrow \infty$, the bulk comprises most of the system and

will determine the physical and topological properties. Due to the translational invariance of the bulk a Fourier transform can be made of the system's Hamiltonian to momentum space defined by the momentum \mathbf{k} . As a consequence of Bloch's theorem, the eigenstates of the momentum space Hamiltonian $\hat{H}(\mathbf{k})$ will be on plane wave form

$$|\psi(\mathbf{k})\rangle = |\mathbf{k}\rangle \otimes |u_{\mathbf{k}}\rangle,$$

where $|\mathbf{k}\rangle$ is the plane wave basis and $|u_{\mathbf{k}}\rangle$ is the cell-periodic part of the wavefunction [111, 112]. The states $|u_{\mathbf{k}}\rangle$ are the eigenstates of the so called bulk momentum space Hamiltonian $\hat{h}(\mathbf{k})$ defined as

$$\hat{h}(\mathbf{k}) = \langle \mathbf{k} | \hat{H}(\mathbf{k}) | \mathbf{k} \rangle.$$

The eigenstates $|u_{\mathbf{k}}\rangle$ are associated to energy bands $E_{\mathbf{k}}$ given by the eigenvalue problem

$$\hat{h}(\mathbf{k})|u_{\mathbf{k}}\rangle = E_{\mathbf{k}}|u_{\mathbf{k}}\rangle. \quad (3.1)$$

The bulk momentum space Hamiltonian will be the central object to determine the symmetries of the system.

Time-reversal symmetry

As the name suggests, time-reversal symmetry implies that the dynamics of the system remains unchanged if time is reversed, i.e. $t \rightarrow -t$. Time-reversal symmetry can be defined via the time-reversal operator $\hat{\mathcal{T}} = \hat{U}\hat{\mathcal{K}}$, where \hat{U} is a unitary operator, i.e. $\hat{U}\hat{U}^\dagger = \mathbb{1}$ and $\hat{\mathcal{K}}$ is the conjugation operator [113]. The presence of the conjugation operator makes the time-reversal operator an anti-unitary operator. The unitary operator \hat{U} depends on the specific system considered. Here, we will restrict ourselves to systems of spinless particles where the unitary operator takes the simple form $\hat{U} = \mathbb{1}$.

Since we will work with lattice systems, it is useful to see how the time-reversal operator acts in momentum space. Consider a bulk momentum space Hamiltonian $\hat{h}(\mathbf{k})$, which has the eigenvalue equation given in equation 3.1. The bulk momentum space Hamiltonian possesses time-reversal symmetry if

$$\hat{\mathcal{T}}\hat{h}(\mathbf{k})\hat{\mathcal{T}}^{-1} = \hat{h}(-\mathbf{k}). \quad (3.2)$$

This means that the eigenvalue equation may be written as

$$\hat{h}^*(-\mathbf{k})|u_{\mathbf{k}}\rangle = E_{\mathbf{k}}|u_{\mathbf{k}}\rangle,$$

and taking the complex conjugate on both sides gives

$$\hat{h}(-\mathbf{k})|u_{\mathbf{k}}\rangle^* = E_{\mathbf{k}}|u_{\mathbf{k}}\rangle^*.$$

From the above equation we can see that for each state $|u_{\mathbf{k}}\rangle$, there exists a time-reversal partner $|u_{\mathbf{k}}\rangle^*$ of the Hamiltonian $\hat{h}(-\mathbf{k})$ with the same energy $E_{\mathbf{k}}$. Time-reversal symmetry hence ensures that the energy bands $E_{\mathbf{k}}$ are symmetric around $\mathbf{k} = \mathbf{0}$ in the FBZ.

Particle-hole symmetry

Systems with particle-hole symmetry are invariant to the change of all the particles to its corresponding hole. In practical terms, this corresponds to the interchange between creation and annihilation operators in the system Hamiltonian. Particle-hole symmetry may be expressed through an anti-unitary operator $\hat{\mathcal{C}} = \hat{U}\hat{\mathcal{K}}$, where \hat{U} is a unitary operator and $\hat{\mathcal{K}}$ is the conjugation operator, which anticommutes with any particle-hole symmetric Hamiltonian.

In momentum space it can be shown that any particle-hole symmetric Hamiltonian satisfies the relation

$$\hat{\mathcal{C}}\hat{h}(\mathbf{k})\hat{\mathcal{C}}^{-1} = -\hat{h}(-\mathbf{k}). \quad (3.3)$$

For the two band models that will be considered in this thesis, the unitary in the particle-hole operator is the Pauli matrix $\hat{U} = \hat{\sigma}_z$, such that $\hat{\mathcal{C}} = \hat{\sigma}_z\hat{\mathcal{K}}$. The particle hole operator has the property that if $|u_{\mathbf{k}}\rangle$ is an eigenstate of a particle-hole symmetric Hamiltonian $\hat{h}(\mathbf{k})$, then $\hat{\mathcal{C}}|u_{\mathbf{k}}\rangle$ is also an eigenstate [113, 114]. The energy band associated to this eigenstate is given by the eigenvalue equation

$$\hat{h}(\mathbf{k})(\hat{\mathcal{C}}|u_{\mathbf{k}}\rangle) = -\hat{\mathcal{C}}(\hat{h}(\mathbf{k})|u_{\mathbf{k}}\rangle) = -E_{\mathbf{k}}\hat{\mathcal{C}}|u_{\mathbf{k}}\rangle.$$

From this it can be concluded that any particle-hole symmetric $\hat{h}(\mathbf{k})$ have energy bands that satisfies $E_{\mathbf{k}} = -E_{-\mathbf{k}}$.

Chiral symmetry

Chiral symmetry is the combination of time-reversal and particle-hole symmetry defined by the chiral operator $\hat{S} = \hat{\mathcal{C}} \cdot \hat{\mathcal{T}}$. In the context of crystalline structures, chiral symmetry is often referred to as sublattice symmetry. For lattice systems consisting of two sublattices, a chiral or sublattice symmetry operation corresponds to transforming all particles on one sublattice to the same particle on the other sublattice.

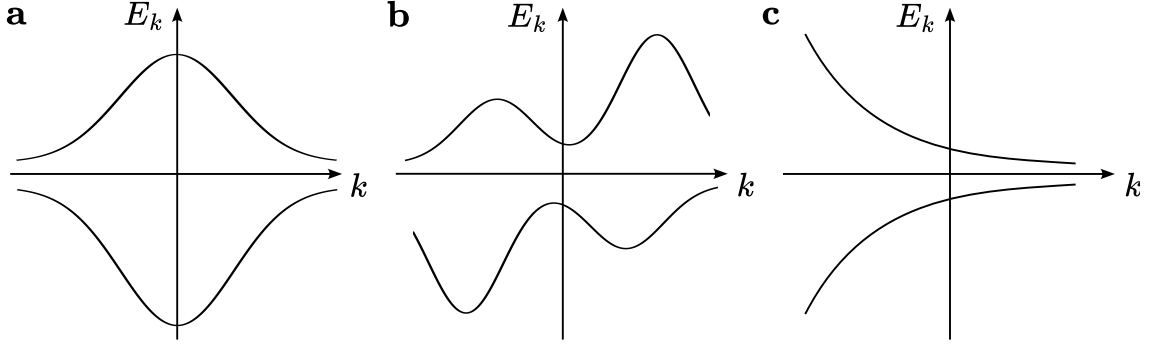


Figure 3.1: *Symmetry effect on energies.* **a:** Time-reversal symmetry gives symmetric energy bands E_k around $k = 0$. **b:** Particle-hole symmetry results in energy bands that are symmetric around $k = 0$ combined with an interchange of bands. **c:** Chiral symmetry gives symmetric energy bands $E_k = -E_{-k}$.

In momentum space, a chiral symmetric Hamiltonian satisfies the relation

$$\hat{S}\hat{h}(\mathbf{k})\hat{S}^{-1} = -\hat{h}(\mathbf{k}). \quad (3.4)$$

As for the two previous symmetries discussed, chiral symmetry puts a restriction on the energy spectrum, namely that $E_k = -E_{-k}$. Figure 3.1 summarizes and illustrates the effects of the three symmetries discussed so far on the energy bands.

Inversion symmetry

Inversion symmetry refers to systems that are invariant under inversion of space, i.e. $\mathbf{r} \rightarrow -\mathbf{r}$, and is the spatial counterpart to time-reversal symmetry studied above. Inversion symmetry plays an important role in crystalline structures due to their inherent spatial periodicity. In such systems, inversion symmetry corresponds to crystal structures that remain invariant under point reflection around a designated inversion center.

As the other symmetries discussed previously, inversion symmetry can be expressed through an operator $\hat{\mathcal{I}}$ called the inversion operator. The inversion operator acting on a state in the position basis has the following effect

$$\hat{\mathcal{I}}|\psi(\mathbf{r})\rangle = |\psi(-\mathbf{r})\rangle,$$

where $\mathbf{r} = 0$ is the inversion center. In momentum space, inversion symmetry corresponds to the inversion of momentum $\mathbf{k} \rightarrow -\mathbf{k}$. For the two band models, which is what we will consider in this thesis, the inversion operator is represented by the Pauli matrix $\hat{\mathcal{I}} = \hat{\sigma}_x$ [115]. Any inversion symmetric momentum space

Hamiltonian satisfies the relation

$$\hat{\mathcal{I}}\hat{h}(\mathbf{k})\hat{\mathcal{I}}^{-1} = \hat{h}(-\mathbf{k}). \quad (3.5)$$

The coexistence of the two inversion symmetries (time and space), results in pairwise degenerate energies [116].

Bulk-boundary correspondence

One of the hallmarks of topological phases in physics is the fact that even though the topology is determined by the bulk of the system, the signatures can be observed on the edges. This is known as the bulk-boundary correspondence. A change of the value of a topological invariant requires a gap closing in the energy spectrum, implying that a degeneracy occurs at the boundary between a topologically non-trivial system and its surroundings, leading to the appearance of localized edge states crossing the bulk energy gaps. More precisely, a non-zero topological invariant of a d -dimensional bulk is expected to be manifested by $(d - 1)$ -dimensional boundary states. These boundary states have energies that are gapped, or largely separated from the energies of the typical bulk states of the system. As a result of the topological protected invariant, the boundary states show a remarkable robustness against local disorder. In particular they are protected from strong perturbations at the boundary of the system, which may break translational symmetry [109].

3.2 Adiabatic evolution, Berry phase and Berry curvature

The adiabatic theorem states that an initial eigenstate of a Hamiltonian will remain an instantaneous eigenstate of the time-dependent Hamiltonian given that the variation is slow and there is a finite gap in the energy spectrum such that

$$\hat{H}(t)|\psi_n(t)\rangle = E_n(t)|\psi_n(t)\rangle. \quad (3.6)$$

Consider now an state expanded in the basis formed by the instantaneous eigenstates of the Hamiltonian $|\Psi(t)\rangle = \sum_n c_n(t)|\psi_n(t)\rangle$. The evolution of the state is given by the time-dependent Schrödinger equation

$$i\hbar \frac{d}{dt}|\Psi(t)\rangle = \hat{H}(t)|\Psi(t)\rangle. \quad (3.7)$$

Inserting the expansion of $|\Psi(t)\rangle$ into equation (3.7) gives

$$i\hbar \sum_n \left(c_n(t) \frac{d}{dt} |\psi_n(t)\rangle + \left(\frac{d}{dt} c_n(t) \right) |\psi_n(t)\rangle \right) = \sum_n c_n(t) E_n(t) |\psi_n(t)\rangle.$$

Multiplying the above equation with $\langle \psi_m(t)|$ from the left and using the fact that $|\psi_n(t)\rangle$ forms an orthonormal basis results in the following expression

$$i\hbar \frac{d}{dt} c_m(t) + i\hbar \sum_n c_n(t) \langle \psi_m(t) | \frac{d}{dt} |\psi_n(t)\rangle = c_m(t) E_m(t). \quad (3.8)$$

The part involving $\langle \psi_m(t) | \frac{d}{dt} |\psi_n(t)\rangle$ may be rewritten by considering the time-derivative of equation (3.6)

$$\left(\frac{d}{dt} \hat{H}(t) \right) |\psi_n(t)\rangle + \hat{H}(t) \frac{d}{dt} |\psi_n(t)\rangle = \left(\frac{d}{dt} E_n(t) \right) |\psi_n(t)\rangle + E_n(t) \frac{d}{dt} |\psi_n(t)\rangle.$$

Again, by multiply both sides with $\langle \psi_m(t)|$ and considering the case where $m \neq n$ we arrive at

$$\langle \psi_m(t) | \frac{d}{dt} |\psi_n(t)\rangle = - \frac{\langle \psi_m(t) | \frac{d}{dt} \hat{H}(t) | \psi_n(t)\rangle}{E_m(t) - E_n(t)}.$$

Inserting this into equation (3.8) gives

$$\frac{d}{dt} c_m(t) - \sum_{n \neq m} \frac{\langle \psi_m(t) | \frac{d}{dt} \hat{H}(t) | \psi_n(t)\rangle}{E_m(t) - E_n(t)} = -\langle \psi_m(t) | \frac{d}{dt} |\psi_m(t)\rangle + i\hbar c_m(t) E_m(t). \quad (3.9)$$

Since the evolution of the Hamiltonian is adiabatic, the rate of change in the Hamiltonian $\frac{d}{dt} \hat{H}(t)$ is small. Furthermore since the difference in energies between the instantaneous eigenstates of $\hat{H}(t)$ is finite, the last term on the left hand side of equation (3.9) can be dropped [117–119]. This is known as the *adiabatic approximation*. Equation (3.9) now reduced to the simpler form

$$\frac{d}{dt} c_m(t) = -\langle \psi_m(t) | \frac{d}{dt} |\psi_m(t)\rangle + i\hbar c_m(t) E_m(t).$$

Integrating the above equation gives the solution for the expansion coefficients $c_m(t) = c_m(0) e^{i\theta_m(t)} e^{i\gamma_m(t)}$, where we have defined the dynamical and geometric or *Berry phase*

$$\begin{aligned} \theta_m(t) &= -\frac{1}{\hbar} \int_0^t E_m(t') dt', \\ \gamma_m(t) &= i \int_0^t \langle \psi_m(t') | \frac{d}{dt} |\psi_m(t')\rangle dt', \end{aligned}$$

respectively [120, 121]. As the names suggests, the dynamical phase depends on the evolution time t , while the geometric phase depends on the geometry or topology of the trajectory in parameter space. For the Berry phase to be a physical, observable quantity it has to be gauge invariant. To check this we try to eliminate the Berry phase by introducing the transformation $|\psi_m(t)\rangle \rightarrow |\psi'_m(t)\rangle = |\psi_m(t)\rangle e^{i\alpha(t)}$. Under this transformation the Berry phase becomes

$$\gamma'_m(t) = i \int_0^t \langle \psi'_m(t') | \frac{d}{dt} | \psi'_m(t') \rangle dt'.$$

Inserting the transformation gives

$$\gamma'_m(t) = \gamma_m(t) + \alpha(0) - \alpha(t),$$

meaning that the Berry phase is gauge invariant if $\alpha(0) = \alpha(t)$, i.e if the trajectory in parameter space forms a closed loop. The Berry phase is thus only observable for cyclic evolutions.

Crystalline solids are systems where the effect of Berry phase naturally occurs. Consider a lattice with a Hamiltonian characterized by a crystal momentum k residing in the First Brillouin Zone (FBZ). As introduced in the previous section, the eigenstates of the Hamiltonian are given by $\hat{H}(k)|\psi_{km}\rangle = E_{km}|\psi_{km}\rangle$, where m now is the band index and $|\psi_{km}\rangle$ are of the form $|\psi_{km}\rangle = |k\rangle \otimes |u_{km}\rangle$, where $|u_{km}\rangle$ is the cell-periodic part of the wavefunction of the m -th band. Due to the torus topology of the FBZ varying k throughout the whole FBZ forms a closed path and the berry phase of the m -th band may be expressed as

$$\gamma_m = i \int_{\text{FBZ}} \langle u_{km} | \nabla_k | u_{km} \rangle \cdot dk. \quad (3.10)$$

This case of the Berry phase running across the entire FBZ is often called the Zak phase and plays an important role in the study of topology in crystalline solids. In presence of inversion symmetry the Berry phase is a quantized quantity equal to 0 or π attributed to a trivial or topological phase, respectively. The Berry phase also plays an important role in the study of polarization [122]. Using Stokes theorem, the Berry phase may be expressed as a surface integral

$$\gamma_m = \int_S (\nabla_k \times A_{m,k}) \cdot \hat{n} dS, \quad (3.11)$$

where we have defined the gauge dependent quantity called the *Berry connection* $A_{m,k} = i \langle u_{km} | \nabla_k | u_{km} \rangle$. The integrand in equation (3.11) is called the *Berry*

curvature

$$\Omega_{k_x k_y}^m = \frac{\partial}{\partial k_x} A_{m, k_y} - \frac{\partial}{\partial k_y} A_{m, k_x} \quad (3.12)$$

and resembles a magnetic field in parameter space with the Berry connection acting as a vector potential. Despite the Berry connection being a gauge dependent quantity, the Berry curvature is gauge invariant and hence observable [123]. The Berry curvature is an intrinsic property of the topology of the band structure, in particular it is non-zero in systems with broken time-reversal or inversion symmetry. According to the Chern theorem, the integral of the Berry curvature over a closed manifold is quantized

$$\oint_S \Omega_{k_x, k_y}^m dS = 2\pi C^m,$$

where C^m is an integer called the *Chern number* [123, 124]. Continuing the analogy with the Berry curvature acting like a magnetic field, a non-zero Chern number is analogous with a magnetic monopole with a finite flux through the surface S .

The Berry curvature and the Chern number play an important role in the classification of topological phases in 2D lattice systems and in topological transport theory as will be discussed in Chapter 5.

3.3 The SSH model

The standard model for studying topological phases in 1D is the Su-Schrieffer-Heeger (SSH) model. It was originally implemented to model polyacetylene polymer chains [125], but generally it describes a 1D staggered lattice or chain of spinless fermions with nearest neighbour hopping. The hopping rates are alternating for each lattice site as shown in Figure 3.2.

The SSH model considers a 1D lattice consisting of N sites. The lattice is composed of two sublattices A and B, both with $N/2$ lattice sites each and a unit cell is formed by pairing one site from A and B. The cells are separated by the lattice constant a . A particle can hop within its unit cell (from sublattice A to B) with a rate given by J'_1 . Furthermore, a particle can hop between neighbouring cells, i.e. from sublattice B to sublattice A of the neighbouring cell, with a rate J_1 . There are no interactions between particles, only hopping, so the system is described by a single-particle Hamiltonian

$$\hat{H} = \hbar \sum_j^{N/2} J'_1 \hat{b}_j^\dagger \hat{a}_j + J_1 \hat{a}_{j+1}^\dagger \hat{b}_j + \text{h.c.}, \quad (3.13)$$

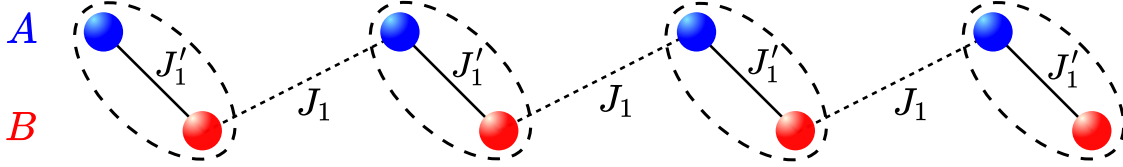


Figure 3.2: *SSH model*. Particles can hop between two sublattices A and B, shown by blue and red dots, with staggered hopping rates J'_1 and J_1 denoted by solid and dashed lines respectively. The dashed circles denote unit cells.

where \hat{a}_j^\dagger (\hat{a}_j) and \hat{b}_j^\dagger (\hat{b}_j) are the creation (annihilation) operators acting on the unit cell j on sublattice A and B respectively. Assuming that the chain is long, i.e. N is large, we can focus on the bulk of the system. Due to the translational invariance of the bulk, we can make a Fourier transform of the creation and annihilation operators given by

$$\begin{aligned}\hat{a}_k &= \frac{1}{\sqrt{N/2}} \sum_j^{N/2} e^{ikaj} \hat{a}_j, \\ \hat{b}_k &= \frac{1}{\sqrt{N/2}} \sum_j^{N/2} e^{ikaj} \hat{b}_j,\end{aligned}$$

where k is the quasi-momentum. Inserting the Fourier transformed operators in the SSH Hamiltonian (3.13) and making use of the definition of the Dirac delta function $N\delta_{kk'} = \sum_{j=1}^N e^{2\pi ij/N(k-k')}$, the Hamiltonian may be written in irreducible form in momentum space as

$$\hat{H} = \sum_{\substack{k \in FBZ \\ \alpha, \beta \in A, B}} \hat{c}_\alpha^\dagger(k) \hat{h}_{\alpha\beta}(k) \hat{c}_\beta(k),$$

where $\hat{c}_A(k) = \hat{a}_k$ and $\hat{c}_B(k) = \hat{b}_k$. The matrix $\hat{h}(k)$ for the SSH model is given by

$$\hat{h}(k) = \hbar \begin{pmatrix} 0 & J'_1 + J_1 e^{ika} \\ J'_1 + J_1 e^{-ika} & 0 \end{pmatrix}. \quad (3.14)$$

The form of $\hat{h}(k)$ displays time reversal symmetry $\hat{\mathcal{T}}\hat{h}(k)\hat{\mathcal{T}}^{-1} = \hat{h}(-k)$, particle-hole symmetry $\hat{\mathcal{C}}\hat{h}(k)\hat{\mathcal{C}}^{-1} = -\hat{h}(-k)$ and chiral symmetry $\hat{\mathcal{S}}\hat{h}(k)\hat{\mathcal{S}}^{-1} = \hat{h}(-k)$. The momentum space Hamiltonian is also inversion symmetric $\hat{\mathcal{I}}\hat{h}(k)\hat{\mathcal{I}}^{-1} = \hat{h}(-k)$, with an inversion center in the middle of the two central sites in the chain. Note that here, inversion symmetry is the point reflection around the inversion center combined with the exchange of the sublattices. The combination of symmetries of the SSH chain implies that the model can be allocated to the BDI symmetry class, which has a \mathbb{Z} -type topological invariant in one dimension [108, 109]. The topo-

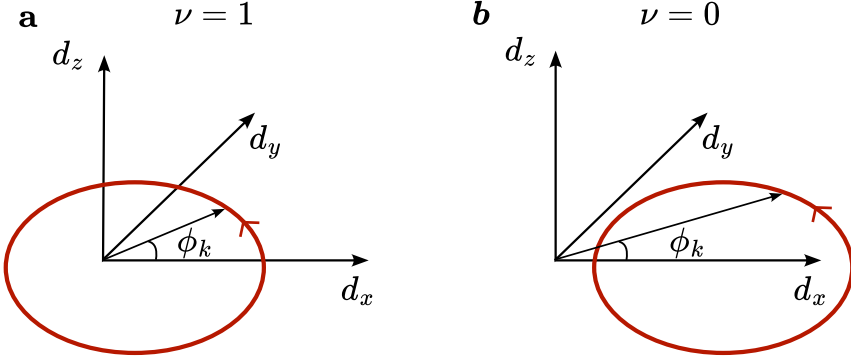


Figure 3.3: *Winding number of the SSH model.* **a:** The winding number is $\nu = 1$ if the curve traced by $\mathbf{d}(k)$ encircles the origin and **b:** $\nu = 0$ if the origin is outside the circle.

logical invariant for the SSH model can be understood by studying the bulk momentum space Hamiltonian (3.14). Any hermitian 2x2 matrix may be expressed in terms of Pauli matrices ($\sigma = (\hat{\sigma}_x, \hat{\sigma}_y, \hat{\sigma}_z)$) and the identity matrix ($\hat{\sigma}_0$). The bulk momentum space Hamiltonian can hence be expressed as $\hat{h}(k) = \hbar \mathbf{d}(k) \cdot \hat{\sigma}$, where we have defined the vector

$$\mathbf{d}(k) = (J'_1 + J_1 \cos(ka), J_1 \sin(ka), 0).$$

The vector can be written as $\mathbf{d}(k) = |\mathbf{d}(k)| e^{i\phi_k}$, where the phase factor $\phi_k = \arctan(d_y/d_x)$. The phase factor gives the internal structure of the eigenstates of the bulk Hamiltonian with momentum k

$$|u_{k\pm}\rangle = \frac{1}{\sqrt{2}} \begin{pmatrix} \pm e^{-i\phi_k} \\ 1 \end{pmatrix},$$

while the magnitude gives the energy of the bands $E_{k\pm} = \pm |\mathbf{d}(k)|$. Using the definition of the Berry phase for 1D lattice systems given in equation (3.10), the Berry phase of the SSH model is given by

$$\gamma_{\pm} = \pm \frac{1}{2} \int_{\text{FBZ}} dk \frac{\partial \phi_k}{\partial k}.$$

Solving the integral we find that the Berry phase of the SSH model can take the following values

$$\gamma_{\pm} = \begin{cases} \mp \pi & \text{if } |J_1| > |J'_1| \\ 0 & \text{if } |J_1| < |J'_1| \end{cases}.$$

When the Berry phase is 0, i.e. when $|J_1| < |J'_1|$, the SSH model is in its trivial phase. However, when the Berry phase is equal to $\pm\pi$, i.e. when $|J_1| > |J'_1|$, the

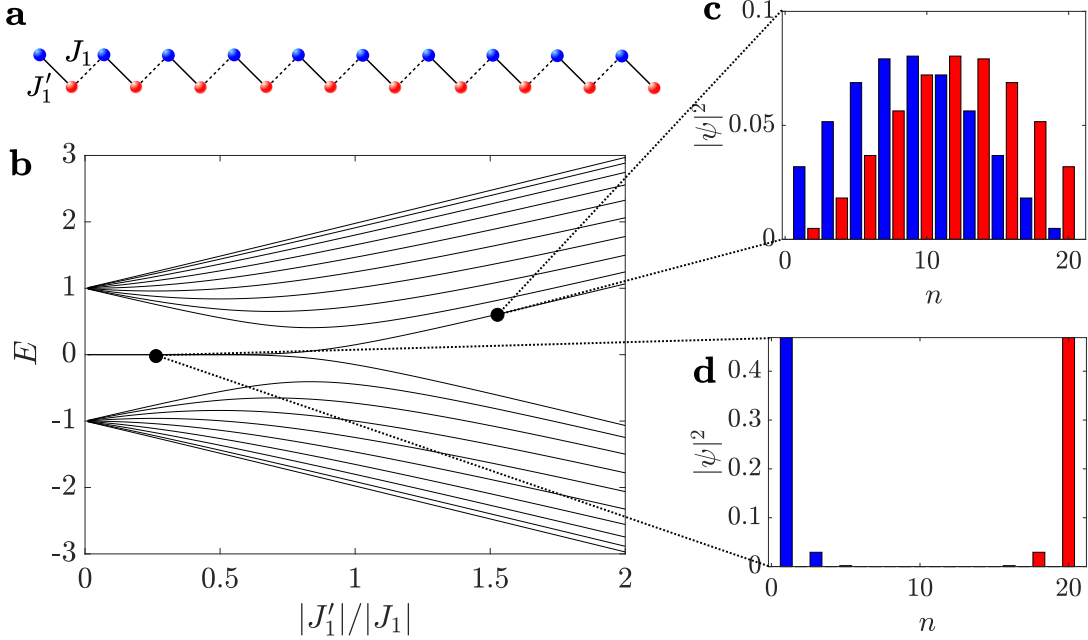


Figure 3.4: *Edge states of the SSH model.* **a:** The SSH lattice. **b:** The energies of the the SSH Hamiltonian with $N = 20$ particles as a function of $|J'_1|/|J_1|$. **c:** An eigenstate ψ for $|J'_1| > |J_1|$ where the most of the support is in the bulk. **d:** An eigenstate ψ for $|J'_1| > |J_1|$ with most of the support on the edge.

SSH model is in its topological phase and describes a 1D topological insulator.

A more intuitive way of characterizing the topological trivial and non-trivial phases of the SSH model is to study the path traced out by the vector $\mathbf{d}(k)$ parameterized by the momentum k in the FBZ. The topology of the system can be determined by simply inspecting whether the closed path encircles the origin. More precisely we can define a topological invariant, the *winding number*, which for the SSH model is given by $v = |\gamma_{\pm}|/\pi$, that counts how many times the path traced out by $\mathbf{d}(k)$ encircles the origin [111] as exemplified in Figure 3.3. There are two ways to change the winding number of the system. Either "pull" the path through the origin by changing the hopping parameters J'_1 and J_1 , or "lift" the path up from the plane spanned by d_x and d_y , by adding a component to d_z , which breaks the chiral symmetry, demonstrating the robustness of the topological phase. Changing the winding number by doing the former requires that you move through the critical point where the path touches the origin, i.e. when $|J'_1| = |J_1|$, the transition point between the trivial and non-trivial phase, where the winding number is undefined.

At the transition point the energy bands $E_k^{\pm} = \pm|\mathbf{d}(k)|$ touch in the borders of the FBZ and the SSH model describes a conductor. For the topological trivial and non-trivial phase the energy bands are gapped throughout the FBZ. However, the topological non-trivial phase is characterized by a pair of eigenenergies

at zero energy separated from the band energies, the energies of the edge states of the SSH model. The two edge states are odd and even superpositions localized on the left and right boundary of the chain with exponentially decreasing occupancy when moving towards the bulk of the chain. The edge states only have a non-zero component on sublattice A/B on the left/right side of the chain. Figure 3.4 shows the evolution of the eigenenergies of the SSH Hamiltonian for $N = 20$ particles when the ratio $|J'_1|/|J_1|$ is increased. When $|J'_1| < |J_1|$ edge states occur with low energies separated from the rest, while for $|J'_1| > |J_1|$, the eigenstates no longer have a dominant support on the edges. In the limiting case of the topological phase of the SSH chain where $J'_1 = 0$, the edge states are not symmetric around the center of the chain but is exponentially localized on either the left or the right side of the chain.

3.4 Topological pumping

Topological pumping relates a systems transport behaviour to its underlying topological properties. Topological pumping can be seen as the quantum analog of the Archimedes screw, where a slow and cyclic motion of the handle pumps water upwards, while for the quantum version pumping of particles is achieved by a slow (adiabatic) and cyclic variation of the Hamiltonian parameters. The concept of topological pumping was introduced by Thouless in the 80's [126]. Initially, the concept was formulated for solid-state systems involving electron or charge transport, but over time it has been adapted to various systems, with 'charge' denoting a generic particle or excitation.

Consider a lattice of particles described by a Hamiltonian consisting of a set of parameters, which are variable in time. Topological pumping requires that the parameters are varied in such a way that the parameter curve encircles a topological degeneracy point in the Hamiltonian (i.e. where the energy gap closes and the winding number is undefined) and in this way making controlled transitions between two topologically distinct phases, which are characterized by topological invariants. After one completed cycle, the initial state is displaced or "pumped". A smooth pumping cycle can be related to a 2D Chern insulator where the time parameter acts as a second wavenumber as it is periodic and can be mapped on a torus. In Chern insulator phases a non-zero Chern number indicates the presence of edge states, analogously to the winding number of the SSH model as introduced in the previous section.

Depending on the choice of initial state, the displacement after a completed cycle can either be a non-quantized or a quantized number of lattice sites, where

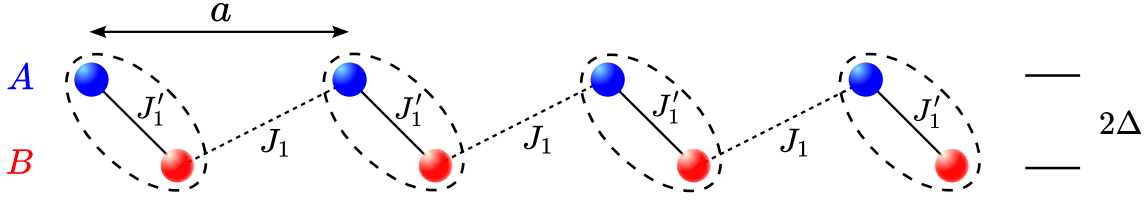


Figure 3.5: *Rice-Mele model*. A chain consisting of two sublattices A and B with blue and red lattice sites respectively, separated by an energy 2Δ . One site of each sublattice forms a unit cell. Particles can hop within its unit cell with a rate J'_1 and from one unit cell to the neighbouring with a rate J_1 . The intrasublattice distance is denoted by a .

the quantization is protected by a topological invariant, the Chern number. When an energy band is fully or uniformly occupied, i.e. all k -states have the same mean occupation, the displacement is given by an integer number (the Chern number) of lattice sites [15, 16]. For inhomogeneous occupation of the bands, the displacement per cycle is non-quantized and can be adjusted [127, 128]. Due to the dependence of the exact geometry of the path, non-quantized topological pumping is often referred to as geometrical pumping in the literature. In this thesis topological pumping will be used as a generic term for both phenomena.

The standard model to study topological pumping is the Rice-Mele model. The Rice-Mele model is an extension to the SSH model, with an additional sublattice energy offset Δ . The Rice-Mele Hamiltonian reads

$$H = \hbar \sum_{j=1}^{N/2} [J'_1 \hat{b}_j^\dagger \hat{a}_j + J_1 \hat{a}_{j+1}^\dagger \hat{b}_j + \text{h.c.}] + \hbar \Delta \sum_{j=1}^{N/2} [\hat{a}_j^\dagger \hat{a}_j - \hat{b}_j^\dagger \hat{b}_j]. \quad (3.15)$$

The Rice-Mele model itself is a non-topological model, except in the limiting case when $\Delta = 0$, due to the broken chiral and particle-hole symmetry induced by Δ . However, the Rice-Mele model still hosts edge states in the topological regime of the SSH model, i.e. when $|J'_1| < |J_1|$, for non-zero values of Δ [129]. Due to the sublattice energy shift, the edge states are not at zero energy, but at energy corresponding to the value of $\pm \hbar \Delta$. The sublattice energy shift breaks the degeneracy of the edge states with the two edge states being exponentially localized at only one edge of the chain. Despite the trivial topological nature of the Rice-Mele model, the edge states are robust against disorder in the hopping parameters as long as Δ is small compared to the values of J_1 such that there is a large gap between the edge states and the bulk states in the energy spectrum.

The introduction of the sublattice energy shifts in the Rice-Mele model allows for making smooth transitions between the topological and trivial phases of the SSH model, without going through the topological degeneracy point where

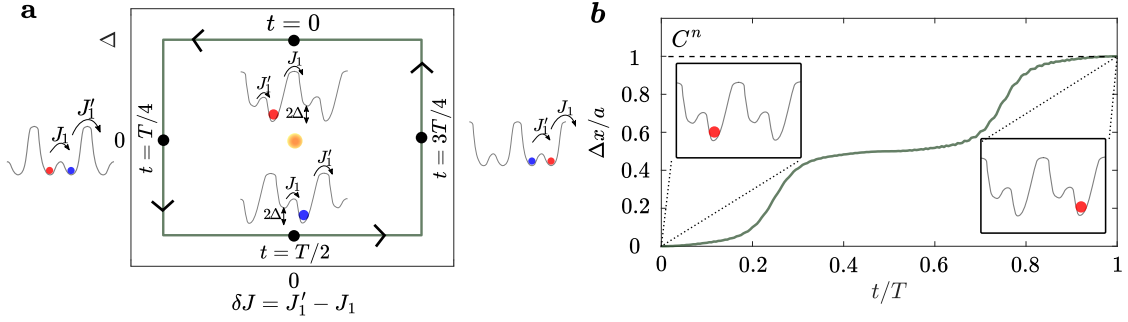


Figure 3.6: *Topological pumping in the Rice-Mele model* **a:** Adiabatically varying the parameters $\delta J = J'_1 - J_1$ and Δ in time in a closed cycle around the topological singularity point [orange dot at $(\Delta, \delta J) = (0, 0)$], one can achieve topologically protected displacement of the fermions by an amount $\Delta x = a$ per cycle, as shown in panel **b**.

$|J'_1| = |J_1|$, by making the parameters time-dependent. Quantized topological pumping can be intuitively understood by considering the picture in Figure 3.6a. Initially (at $t = 0$), $\Delta > 0$, a particle is located on the red sublattice. Now, slowly decreasing the value of Δ to zero while increasing $J_1 > J'_1$ the particle will split on the red sublattice and the blue sublattice to the right. Decreasing Δ further to negative values, the particle will fully localize on the more energetically favourable blue sublattice. Then, increasing Δ again to zero while simultaneously increasing $J'_1 > J_1$, the particle will again split on the blue sublattice and the red sublattice on the right. Returning to the initial parameter configuration with $\Delta > 0$, forming a closed path around the origin in parameter space, the particle will fully localize on the red sublattice. However after this procedure, the initial particle has been displaced by $\Delta x/a = 1$ equal to the Chern number, C^n , of the lower band as shown in Figure 3.6b.

In general, for a uniformly filled band, the displacement after a completed cycle can be calculated from

$$\Delta x = \frac{a}{2\pi} \int_0^T dt \int_{\text{FBZ}} \Omega_{tk}^n dk = aC^n, \quad (3.16)$$

with FBZ denoting the First Brillouin Zone and Ω_{tk}^n is the Berry curvature of the n -th band introduced in Section 3.2. To compute the Berry curvature, the bulk properties of the Rice-Mele model are needed. Similarly as for the SSH model, the bulk momentum space Hamiltonian is found by making a Fourier transform of the creation and annihilation operators and reads

$$\hat{h}(k) = \hbar \begin{pmatrix} \Delta & J'_1 + J_1 e^{ika} \\ J'_1 + J_1 e^{-ika} & -\Delta \end{pmatrix}, \quad (3.17)$$

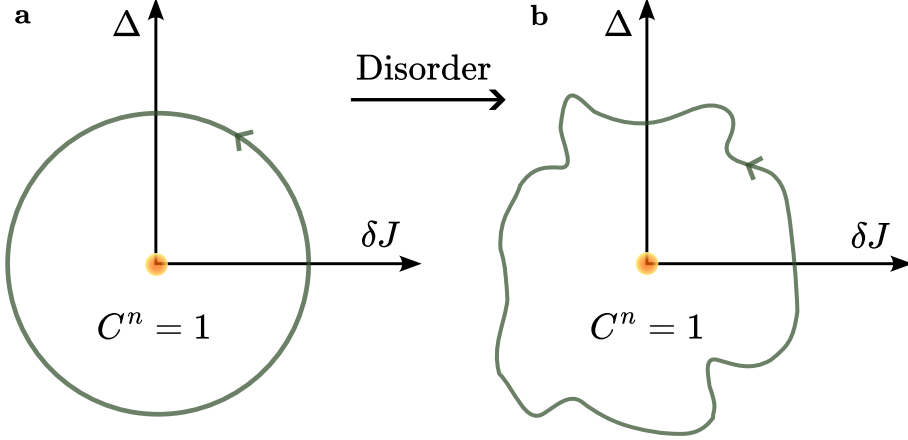


Figure 3.7: *Robustness of topological pumping* **a:** A path in parameter space giving a displacement after a pumping cycle equal to the Chern number $C^n = 1$. **b:** Adding disorder in the system, deforming the path, the displacement after a pumping cycle remains quantized as long as the path still encircles the topological degeneracy point marked by the orange dot.

and the eigenstates are given by

$$\begin{aligned} |u_{k-}\rangle &= \frac{1}{\mathcal{N}} \left(\frac{J'_1 + J_1 e^{ika}}{-\sqrt{|J'_1 + J_1 e^{ika}|^2 + \Delta^2} - \Delta} \right), \\ |u_{k+}\rangle &= \frac{1}{\mathcal{N}} \left(\frac{\sqrt{|J'_1 + J_1 e^{ika}|^2 + \Delta^2} + \Delta}{J'_1 + J_1 e^{-ika}} \right), \end{aligned}$$

where \mathcal{N} is a normalization factor and $+/-$ denotes the upper/lower band. The upper and lower energy bands are given by $E_{k\pm} = \pm \sqrt{|J'_1 + J_1 e^{ika}|^2 + \Delta^2}$. The form of the bulk momentum space Hamiltonian in equation (3.17) possesses time-reversal symmetry (3.2). The three other relevant symmetries, particle-hole, chiral and inversion symmetry are all broken due to the diagonal term when $\Delta \neq 0$, meaning that the Rice-Mele model in 1D does not have a topological invariant. The breaking of inversion symmetry results in a non-zero Berry curvature, giving rise to a non-zero displacement after a pumping cycle as seen from equation (3.16). In fact, the inversion symmetry for $\Delta = 0$ is responsible for the quantization of the Chern number such that it is restricted to integer values [123]. When the path in parameter space encircles the topological degeneracy point, the Chern number takes non-zero integer values, while if the degeneracy point is outside the closed path the Chern number is zero.

The observation, in simulations or experiments, of a quantized displacement after a completed pumping cycle requires that the variation of the parameters is kept adiabatic such that the evolution of the instantaneous state follows the evol-

ution of the Hamiltonian. Previous studies have shown that, despite the topological nature of the pumping, the phenomenon is not robust against non-adiabatic effects [130]. The adiabaticity criterion can be formulated as $T \gg 1/\Delta E_k$, where $\Delta E_k = \min(E_{k+} - E_{k-})$ is the minimal gap during the cycle.

Since the quantization of the Chern number only requires that the path in parameter space encircles the topological degeneracy point, the displacement after a pumping cycle is robust against any local disorder that deforms the path, but keeps the degeneracy point within its bounds as shown in Figure 3.7 illustrating the robustness of topological pumping.

3.5 Robust quantum state transfer

As we have seen in the previous section, topological pumping is a robust state transport mechanism relying on adiabatic evolution. However, the transport is limited, i.e. for quantized topological pumping the displacement after one adiabatic cycle is equal to one lattice constant. Transport of an initial state over long distances can be made possible by adiabatically connecting eigenstates of the Hamiltonian by varying system parameters. This is known as quantum state transfer.

Quantum state transfer can be split into two kinds: For systems where the parameters of the Hamiltonian is initially engineered in a desired way and then let freely evolve (time-independent state transfer) and for systems where the Hamiltonian parameters are varied in a controlled fashion throughout the adiabatic evolution (time-dependent state transfer). Quantum state transfer has been extensively studied in spin chains for both time-independent [131–133] and time-dependent protocols [133, 134].

The two factors that determines the efficiency of the quantum state transfer is the transfer time and robustness against decoherence or disorder. Quantum state transfer protocols rely on adiabatic evolution, i.e. long transfer times, leading to higher order of decoherence, lowering the transfer efficiency. However, as a tradeoff, quantum state transfer can be made robust against decoherence by applying adiabatic evolution in topological non-trivial systems. A prime example is using the Rice-Mele model [135–138]. For $\Delta = 0$ the Rice-Mele Hamiltonian reduces to the SSH Hamiltonian, which for $J'_1 = 0$ display two zero energy edge states, one on the left and one on the right side of the chain. By adiabatically varying the parameters Δ , J'_1 and J_1 smooth transitions between the left and right edge states can be achieved.

Quantum state transfer in the Rice-Mele model can be understood in the fol-

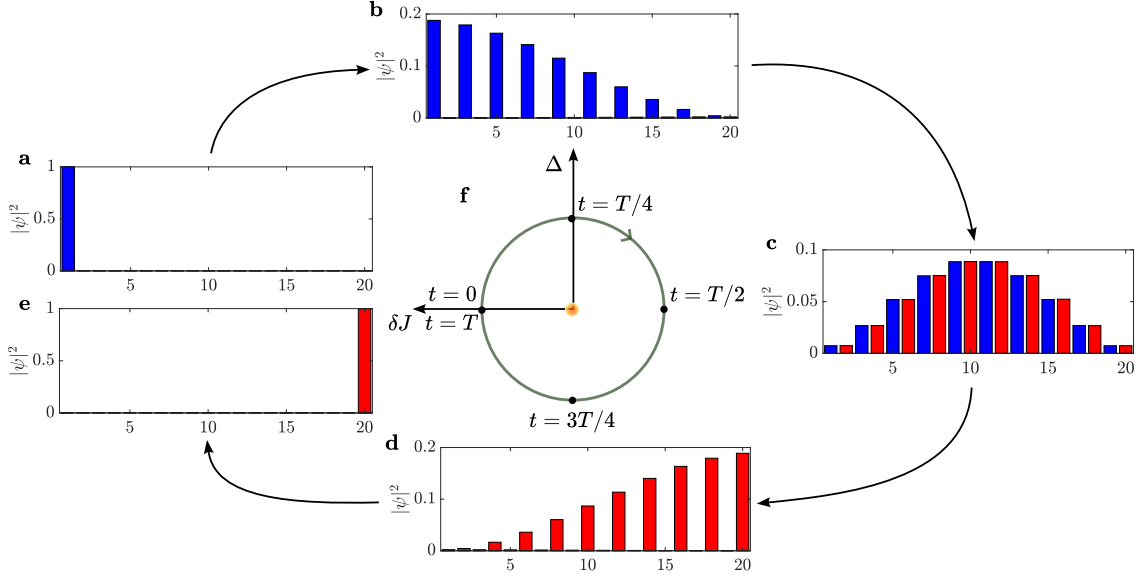


Figure 3.8: *Robust quantum state transfer in the Rice-Mele model.* **a:** Initially the state is localized on the left edge. **b:** After a time $t = T/4$, the state has moved into the bulk, but is occupying only sublattice A. **c:** In the middle of the cycle ($t = T/2$), the state is fully in the bulk spread evenly on sublattice A and B. **d:** At time $t = 3T/4$ the state is moving towards the right side of the chain occupying only sublattice B. **e:** In the end of the cycle ($t = T$), the state localizes on the right edge of the chain. **f:** The Hamiltonian parameters, $\Delta(t)$ and $\delta J(t) = J_1(t) - J'_1(t)$ are varied during the cycle such that the parameter curve encircles the origin.

lowing way. Initially the parameters $\Delta = 0$ and J'_1 is chosen such that the left edge state is an eigenstate of the Hamiltonian. Choosing this as an initial state and evolving the Hamiltonian parameters until $\Delta = \Delta_{\max}$ and $J'_1 = J_1$, the initial state has moved into the bulk of sublattice A as seen in Figure 3.8a. Evolving further such that $J'_1 > J_1$ and $\Delta = 0$, the state is symmetric around the center of the chain occupying both sublattices equally. Making $\Delta = -\Delta_{\max}$ and $J'_1 = J_1$, the state has moved towards the right edge, now only occupying the energetically favourable sublattice B. Finally, returning to the initial parameter values, the state fully localized on the right zero energy edge of the chain, completing the quantum state transfer from one zero energy edge to the other.

For quantum state transfer between the two edges of the Rice-Mele chain to be achieved three conditions needs to be met. First, initially the parameters $J'_1 = 0$ and $\Delta = 0$ such that the completely localized edge states are eigenstates of the Hamiltonian. Second, Δ has to change sign in the middle of the cycle. Last, in the middle of the cycle, the hopping parameters have to be non-zero such that there is a gap in the energy spectrum. The last condition ensures that the adiabatic condition is met without exaggerated transfer times, increasing the efficiency of the quantum state transfer.

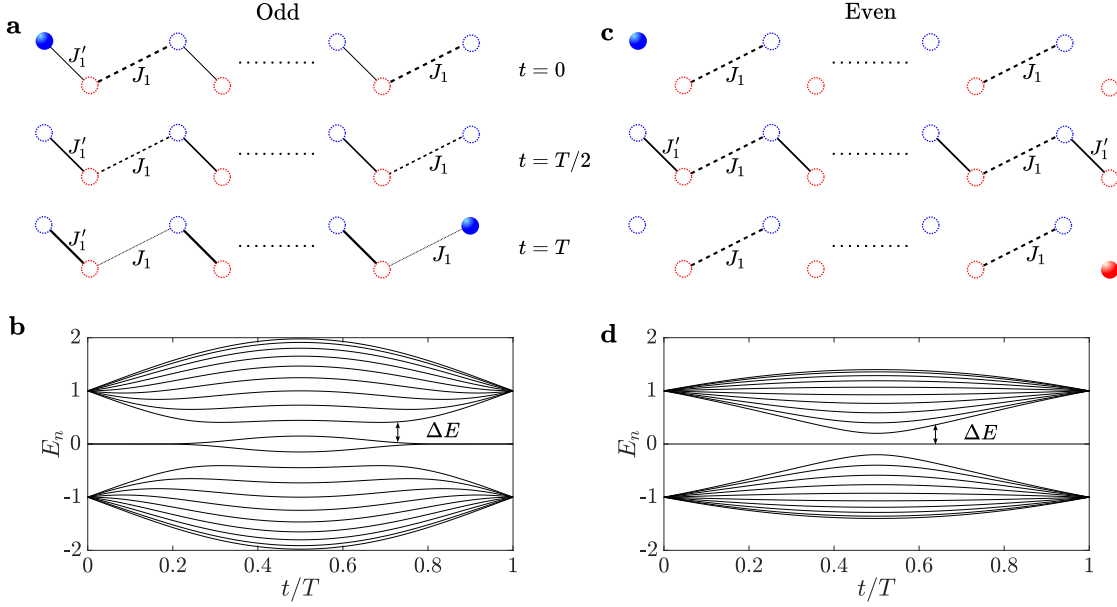


Figure 3.9: *Robust quantum state transfer in the SSH model.* **a:** A SSH chain with odd number of lattice sites display a left edge state for $J'_1 < J_1$. Evolving the parameters for a time $t = T/2$ where $J'_1 = J_1$, the initial edge state has moved into the bulk. Evolving further to $t = T$ where $J'_1 > J_1$, the state will localize again, but now on the right edge mode. **b:** The energy spectrum for odd number of sites during the cycle always display a gap between the initial edge state and the continuum states. **c:** For $J'_1 = 0$ an even number SSH chain display left and right edge states. Evolving until $t = T/2$ where $J'_1 = J_1$ the initial right edge state moves into the bulk. Evolving further to $t = T$ where the initial parameter configuration is reached, the state will localize on the right edge. **d:** The energy spectrum for even number of sites during the cycle always display a gap between the initial edge state and the continuum states.

Quantum state transfer between two zero mode edge states can also be performed in the SSH chain [139–142], i.e without introducing the additional sublattice energy shift. Similarly as to the protocol in the Rice-Mele model discussed above, quantum state transfer in the SSH model with an even number of sites requires a vanishing J'_1 initially and finally in the evolution in order to have edge eigenstates localized on a single boundary. Quantum state transfer in the SSH model puts an additional restriction on the hopping rates, namely that $J_1 > J'_1$ throughout the evolution except for $t = T/2$ where $J_1 = J'_1$, such that a transition from the left to the right edge occurs. This restriction makes robust quantum state transfer challenging to achieve in physical systems, since precise controllability of the hopping parameters is needed.

Quantum state transfer in a SSH chain with an odd number of sites eases these restrictions. The breaking of translational symmetry resulting from the odd number of sites leads to a left edge state for $J'_1 < J_1$, but also a right edge state for

$J'_1 > J_1$. Quantum state transfer between the two edges of the odd site SSH chain can occur by a adiabatic evolution of the hopping rates from $J'_1 < J_1$ to $J'_1 > J_1$. Here, vanishing J'_1 (J_1) in the beginning (end) of the evolution is not needed and the only necessary condition is that the two hopping rates cross at $t = T/2$.

A schematic for quantum state transfer in the SSH model with both odd and even sites is shown in Figure 3.9a and 3.9c. Figure 3.9b and 3.9d show the energy spectrum during the time evolution. For a finite number of lattice sites N , there is always a gap ΔE between the evolved edge states and the continuum states ensuring that the adiabaticity criterion can be met.

Chapter 4

Modified dipole-dipole interactions in waveguide QED

4.1 Introduction

Emitters coupled to nanophotonic waveguides have received significant interest due to the strong and homogeneous coupling between the emitters and long coherence times. As a result of the confined or guided field modes carried by these nanostructures the coherent dipole-dipole interactions between emitters are, in theory, infinite range (all-to-all). In this work, we provide a detailed recipe on how to calculate the dipole-dipole interactions and dissipation of emitters coupled to a nanophotonic waveguide through the electromagnetic Green's tensor. We start by reproducing the guided mode contribution to the dipole-dipole interaction and dissipation by analytically computing the Green's tensor using the technique of eigenmode decomposition. Then we, for the first time, introduce a numerical method for computing the unguided (radiation) mode contribution overcoming convergence issues that typically make the accurate numerical determination extremely challenging.

Finally, we show that due to the presence of the nanofiber, the radiation field in its vicinity can be significantly altered, giving rise to contributions to the dipole-dipole interactions that significantly differ from the free-field counterparts. Owing to the collective character of both coherent and incoherent interactions, when measuring experimentally observable properties such as the transmission signal of fiber-guided light, these differences are even more evident as the number of emitters is increased.

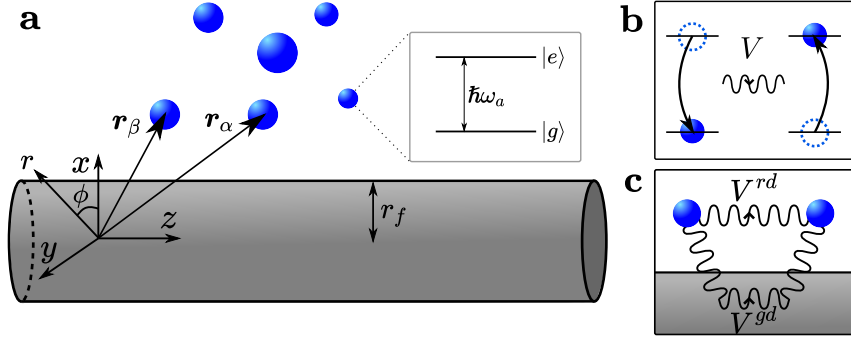


Figure 4.1: *Dipole-dipole interactions between emitters next to a nanofiber.* **a:** N emitters in vacuum are placed in the vicinity of a nanofiber with radius r_f . Each emitter is a two-level system with an excited ($|e\rangle$) and a ground ($|g\rangle$) state separated by an energy $\hbar\omega_a$. **b:** Due to their coupling to the electromagnetic field modes, the emitters interact through the exchange of virtual photons. **c:** These interactions have contributions stemming from the guided (V^{gd}) and the radiation (V^{rd}) modes.

4.2 System and master equation

We consider an ensemble of N identical emitters placed near the surface of a nanophotonic waveguide (see Fig. 4.1a). Each emitter is modelled as a two-level system with ground and excited states $|g\rangle$ and $|e\rangle$, respectively, separated by an energy $\hbar\omega_a$. Under the approximations discussed in Section 2.1, the dynamics of the reduced density matrix $\hat{\rho}$, which contains the internal degrees of freedom of the emitters, is determined by the master equation

$$\dot{\hat{\rho}} = i \sum_{\alpha \neq \beta} V_{\alpha\beta} [\hat{\sigma}_\alpha^\dagger \hat{\sigma}_\beta, \hat{\rho}] + \sum_{\alpha, \beta} \Gamma_{\alpha\beta} \left(\hat{\sigma}_\beta \hat{\rho} \hat{\sigma}_\alpha^\dagger - \frac{1}{2} \{ \hat{\sigma}_\alpha^\dagger \hat{\sigma}_\beta, \hat{\rho} \} \right), \quad (4.1)$$

where $\hat{\sigma}_\alpha = |g_\alpha\rangle\langle e_\alpha|$ is the spin-1/2 ladder operator for the α -th emitter. The first term in the master equation describes dipole-dipole or exchange interactions with magnitude $V_{\alpha\beta}$, which are mediated by the exchange of virtual photons between the emitters (see Fig. 4.1b). The second term of (2.1) describes incoherent photon emission or dissipation in the system, which in general displays a collective character. Separating the contributions from the guided modes of the waveguide and the radiation modes leads to the decomposition of the dipole-dipole and collective dissipation matrices: $V_{\alpha\beta} = V_{\alpha\beta}^{gd} + V_{\alpha\beta}^{rd}$ and $\Gamma_{\alpha\beta} = \Gamma_{\alpha\beta}^{gd} + \Gamma_{\alpha\beta}^{rd}$, see Fig. 4.1c.

Our aim is to obtain the coefficient matrices $V_{\alpha\beta}$ and $\Gamma_{\alpha\beta}$, which in turn fully determine all properties in the system. These can be determined via the electromagnetic Green's tensor $\tilde{G}(\mathbf{r}_\alpha, \mathbf{r}_\beta, \omega)$ of the environment evaluated at the emitter

positions \mathbf{r}_α and \mathbf{r}_β as [37, 38, 91]

$$V_{\alpha\beta} = \frac{\omega_a^2}{\hbar\epsilon_0 c^2} \mathbf{d}_\alpha^* \text{Re}\{\bar{G}(\mathbf{r}_\alpha, \mathbf{r}_\beta, \omega_a)\} \mathbf{d}_\beta^T,$$

$$\Gamma_{\alpha\beta} = \frac{2\omega_a^2}{\hbar\epsilon_0 c^2} \mathbf{d}_\alpha^* \text{Im}\{\bar{G}(\mathbf{r}_\alpha, \mathbf{r}_\beta, \omega_a)\} \mathbf{d}_\beta^T,$$

where \mathcal{P} denotes the principal value and \mathbf{d}_α is the transition dipole moment for the α -th emitter. In Section 2.2.2 we derived an integral expression, using eigenmode decomposition, for the guided and radiation mode contribution to the Green's tensor for a nanophotonic waveguide. In the following, we will aim to propose a comprehensive guide for solving these integrals, for the case of guided modes analytically, and for the radiation modes numerically, with high accuracy.

4.3 Green's tensor for a cylindrical nanofiber

As discussed in Section 2.2, the Green's tensor can be expressed in terms of the eigenmodes of the positive frequency part of the electric field as

$$\bar{G}(\mathbf{r}, \mathbf{r}', \omega) = \sum_n \frac{\mathbf{E}_n(\mathbf{r}, \omega) \mathbf{E}_n^\dagger(\mathbf{r}', \omega)}{\lambda_n}.$$

Here, $\mathbf{E}_n(\mathbf{r}, \omega)$ are the eigenvectors of the hermitian operator $\mathcal{H} = [k^2 - \frac{1}{\epsilon(\mathbf{r}, \omega)} \nabla \times \nabla \times]$ with eigenvalues λ_n . This representation allows us to easily split the contribution to the Green's tensor coming from the eigenmodes guided by the waveguide and the unguided (radiative) ones as $\bar{G}(\mathbf{r}, \mathbf{r}', \omega) = \bar{G}^{gd}(\mathbf{r}, \mathbf{r}', \omega) + \bar{G}^{rd}(\mathbf{r}, \mathbf{r}', \omega)$ [103, 104, 143]. Let us analyze these contributions separately for the case of a cylindrical dielectric nanofiber of radius r_f characterized by a refractive index n_1 placed in an infinite vacuum of refractive index $n_2 = 1$. To do so, we will use a cylindrical coordinate system (r, ϕ, z) , centered in the fiber core with the z -direction being along the fiber (see Fig. 4.1a).

4.3.1 Guided modes

Using eigenmode composition as detailed in Section 2.2.2, the guided contribution to the Green's tensor is given by

$$\bar{G}^{gd}(\mathbf{r}, \mathbf{r}', \omega') = \frac{1}{2\pi} \sum_{fl} \int_0^\infty d\beta \frac{\mathbf{e}^{(\mu)}(\mathbf{r}) \mathbf{e}^{(\mu)\dagger}(\mathbf{r}')}{k'^2 - (\beta^2 - q^2)} e^{il(\phi - \phi')} e^{if\beta(z - z')},$$

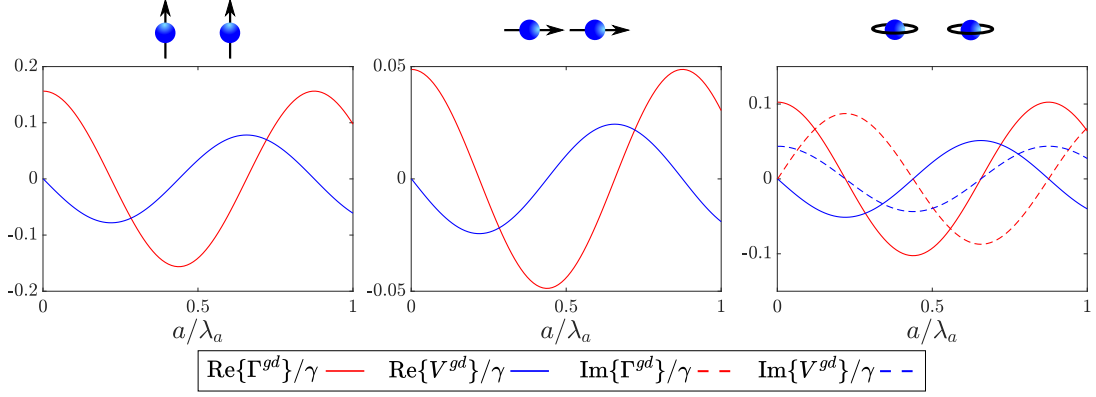


Figure 4.2: *Guided contribution to the coefficients.* The real and imaginary part of the guided contribution to the dissipation and dipole-dipole interactions between two emitters as a function of the separation a for different dipole orientations.

where $(\mu) \equiv (\beta, l, f)$ are the labels of the guided modes. Here, $l = \pm 1$ is the polarization of the mode, $f = \pm 1$ is the propagation direction for the guided modes in the fiber and $\mathbf{e}^{(\mu)}(\mathbf{r})$ are the guided profile functions (note, that we assume that the nanofiber supports only the fundamental HE₁₁ guided mode). In addition, β is the longitudinal propagation constant in the fiber, which for each value of ω is determined via the fiber eigenvalue equation given in Section 2.2.2, q is a variable associated to the field outside the nanofiber and $k' = \omega'/c$. The expression for the Green's tensor may be written in terms of the mode frequency ω by using the relation $q^2 = \beta^2 - k^2$, such that

$$\bar{G}^{gd}(\mathbf{r}, \mathbf{r}', \omega') = \frac{c^2}{2\pi} \sum_{fl} \int_0^\infty d\omega \frac{\mathbf{e}^{(\mu)}(\mathbf{r}) \mathbf{e}^{(\mu)\dagger}(\mathbf{r}')}{\omega'^2 - \omega^2} \beta'(\omega) e^{il(\phi-\phi')} e^{if\beta(\omega)(z-z')},$$

where $\beta'(\omega) = \frac{d\beta}{d\omega}$.

The guided contribution to the Green's tensor is purely transverse, i.e. it is holomorphic in the upper half complex plane including the real axis. We can therefore apply the Sokhotski–Plemelj theorem to find its imaginary part

$$\text{Im}\{\bar{G}^{gd}(\mathbf{r}, \mathbf{r}', \omega)\} = \frac{c^2}{4\omega} \sum_{fl} \mathbf{e}^{(\mu)}(\mathbf{r}) \mathbf{e}^{(\mu)\dagger}(\mathbf{r}') \beta'(\omega) e^{il(\phi-\phi')} e^{if\beta(\omega)(z-z')},$$

which gives a guided contribution to the collective decay matrix that reads

$$\Gamma_{\alpha\beta}^{gd} = \frac{\omega_a \beta'_a}{2\hbar\epsilon_0} \sum_{fl} \mathbf{d}_\alpha^* \cdot \mathbf{e}^{(\beta_a lf)}(\mathbf{r}_\alpha) \mathbf{d}_\beta \cdot \mathbf{e}^{(\beta_a lf)*}(\mathbf{r}_\beta) e^{il\phi_{\alpha\beta}} e^{if\beta_a z_{\alpha\beta}},$$

with $\beta_a = \beta(\omega_a)$, $z_{\alpha\beta} = z_\alpha - z_\beta$ and $\phi_{\alpha\beta} = \phi_\alpha - \phi_\beta$.

Since the guided mode contribution to the Green's tensor is purely transverse the usual Kramers-Kronig relations hold and we can express the real part as

$$\text{Re}\{\bar{G}^{gd}(\omega)\} = \frac{1}{\pi} \mathcal{P} \int_{-\infty}^{\infty} d\omega' \frac{\text{Im}\{\bar{G}^{gd}(\omega')\}}{\omega' - \omega}.$$

The principal value integral in this equation can be calculated analytically choosing an appropriate contour [53, 62], and one finds that

$$V_{\alpha\beta}^{gd} = i \frac{\omega_a \beta'_a}{4\hbar\epsilon_0} \sum_{fl} \mathbf{d}_\alpha^* \cdot \mathbf{e}^{(\beta_a lf)}(\mathbf{r}_\alpha) \mathbf{d}_\beta \cdot \mathbf{e}^{(\beta_a lf)*}(\mathbf{r}_\beta) \text{sgn}(f z_{\alpha\beta}) e^{il\phi_{\alpha\beta}} e^{if\beta_a z_{\alpha\beta}},$$

is the guided contribution to the dipole-dipole interaction, shown in Figure 4.2 for three different dipole orientations. The dipole-dipole interactions and collective decay rates are periodic with the distance a and are infinitely ranged. Their peak strength depends on the dipole orientation. For circularly polarized dipoles (right in Figure 4.2), the coefficients take imaginary values due to the complex dipole vector.

4.3.2 Radiation modes

The radiation modes of the electric field can be both transverse and longitudinal. However, as detailed in Section 2.2.2, only the transverse modes are affected by the presence of the waveguide. Using the expression for the transverse radiation modes of the electric field given in Section 2.2.2, the radiative contribution to the Green's tensor is given by

$$\bar{G}^{rd}(\mathbf{r}, \mathbf{r}', \omega') = \sum_{ml} \int_{-\infty}^{\infty} d\beta \int_0^{\infty} dq \frac{\mathbf{e}^{(\nu)}(\mathbf{r}) \mathbf{e}^{(\nu)\dagger}(\mathbf{r}')}{k'^2 - (\beta^2 + q^2)} e^{im(\phi - \phi')} e^{i\beta(z - z')} + \bar{G}^{0\parallel}(\mathbf{r}, \mathbf{r}', \omega'),$$

where $(\nu) \equiv (\beta, q, m, l)$ are the labels of the radiation modes, with $l = \pm 1$ and $m = 0, \pm 1, \pm 2, \dots$ labelling the polarization and order of the mode. In contrast to the guided mode case, $\beta = k \cos \theta$ is here a continuous variable for each value of the frequency ω and the variable $q = k \sin \theta$ is characteristic of the field outside the nanofiber. Finally, $\mathbf{e}^{(\nu)}(\mathbf{r})$ is the radiation profile function of the transverse electric field. The Green's tensor may be rewritten in terms of the mode frequency ω and the angle θ as

$$\bar{G}^{rd}(\mathbf{r}, \mathbf{r}', \omega') = \sum_{ml} \int_0^{\infty} d\omega \omega \int_0^{\pi} d\theta \frac{\mathbf{e}^{(\nu)}(\mathbf{r}) \mathbf{e}^{(\nu)\dagger}(\mathbf{r}')}{\omega'^2 - \omega^2} e^{im(\phi - \phi')} e^{i\frac{\omega}{c} \cos \theta (z - z')} + \bar{G}^{0\parallel}(\mathbf{r}, \mathbf{r}', \omega').$$

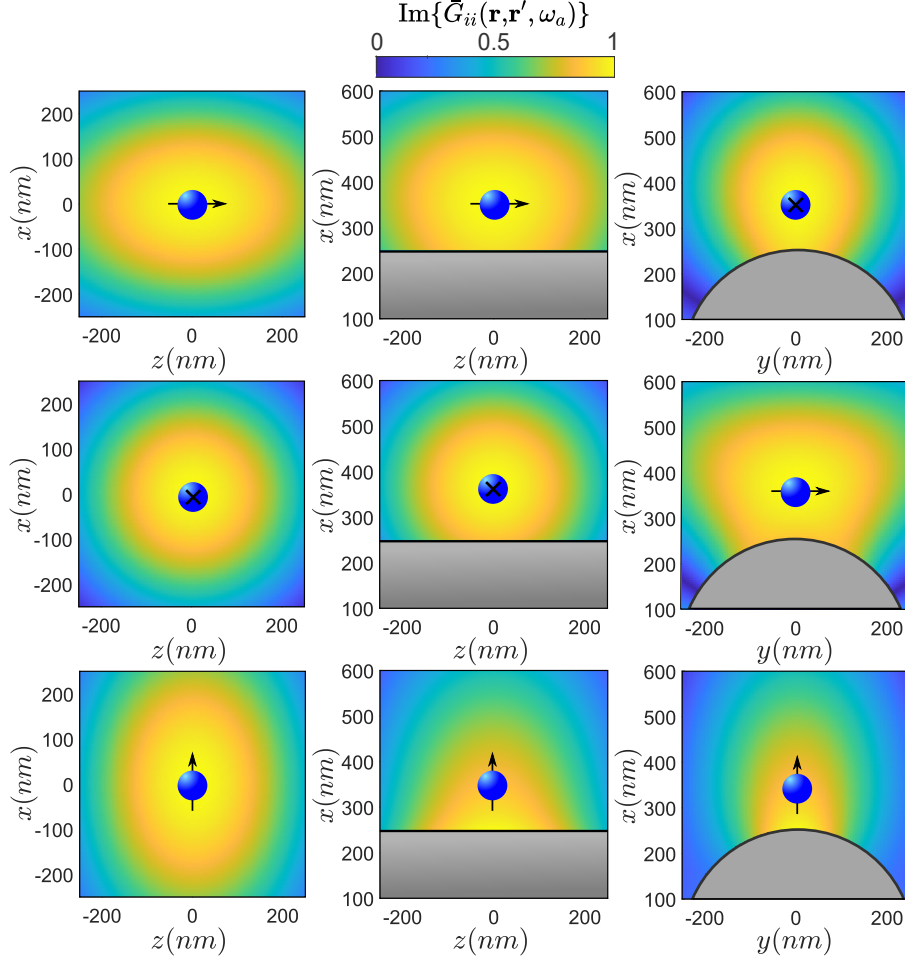


Figure 4.3: Modified radiation field near a nanofiber. Diagonal component of the imaginary part of the Green's tensor $\text{Im}\{G_{ii}(\mathbf{r}, \mathbf{r}', \omega_a)\}$ with $i = x, y, z$ (bottom, middle and upper row, respectively, all in arbitrary units) around a dipole placed at $\mathbf{r}' = 0$ as a function of the coordinate \mathbf{r} in the zx -plane (left and middle column) and in the yx -plane (right column). The cross in the middle of the dipole should be interpreted as the dipole pointing into the plane. The left column shows $\text{Im}\{G_{ii}^0\}$ in vacuum (free field), while the middle and right columns display $\text{Im}\{G_{ii}^{rd}\}$ at a distance of 100 nm from the surface of a silica nanofiber with $r_f = 250$ nm. The frequency $\omega_a = 2\pi c/\lambda_a$ corresponds to the D2 transition in Cs, with $\lambda_a = 852$ nm. The refractive index of the silica nanofiber is modeled using a Sellmeier equation [144].

Note that we have chosen specifically the eigenmode decomposition adopted in [103], which differs from, for example, the one adopted in [62] in the accompanying normalization factors. However, let us point out that the two formulations are equivalent and hence give the same results.

Similarly as for the guided modes, we use the Sokhotski–Plemelj theorem to find the imaginary part of the radiation Green's tensor using the fact that the transverse component is holomorphic in the upper half complex plane and well-

behaved on the real frequency axis. The imaginary part becomes then

$$\text{Im}\{\bar{G}^{rd}(\mathbf{r}, \mathbf{r}', \omega)\} = \frac{\pi}{2} \sum_{ml} \int_0^\pi d\theta \mathbf{e}^{(\nu)}(\mathbf{r}) \mathbf{e}^{(\nu)\dagger}(\mathbf{r}') e^{im(\phi-\phi')} e^{i\frac{\omega}{c} \cos \theta (z-z')},$$

such that the corresponding contribution to the dissipation matrix reads

$$\Gamma_{\alpha\beta}^{rd} = \frac{\pi\omega_a^2}{\hbar\epsilon_0 c^2} \sum_{ml} \int_0^\pi d\theta \mathbf{d}_\alpha^* \cdot \mathbf{e}^{(\beta_a q_a ml)}(\mathbf{r}_\alpha) \mathbf{d}_\beta \cdot \mathbf{e}^{(\beta_a q_a ml)*}(\mathbf{r}_\beta) e^{im\phi_{\alpha\beta}} e^{i\beta_a z_{\alpha\beta}},$$

where now $\beta_a = \frac{\omega_a}{c} \cos \theta$ and $q_a = \frac{\omega_a}{c} \sin \theta$ are both functions of the angle θ .

We use the imaginary part of the Green's tensor evaluated at $\omega = \omega_a$ to illustrate in Fig. 4.3 how much the presence of the nanofiber disturbs the field around a point dipole compared to the situation where the dipole is in free space. In particular, we can clearly observe that the field is most dramatically modified when the dipole moment is perpendicular to the axis of the nanofiber (y and x directions, second and third row in Fig. 4.3).

The real part of the radiation Green's tensor can be found by applying the Kramers-Kronig relation to the transverse part of the radiation Green's tensor,

$$\text{Re}\{\bar{G}^{rd}(\omega)\} = \frac{1}{\pi} \mathcal{P} \int_{-\infty}^{\infty} d\omega' \frac{\text{Im}\{\bar{G}^{rd}(\omega')\}}{\omega' - \omega} + \bar{G}^{0\parallel}(\omega),$$

such that the radiation contribution to the dipole-dipole interaction is given by

$$V_{\alpha\beta}^{rd} = \frac{\omega_a^2}{\pi\hbar\epsilon_0 c^2} \mathcal{P} \int_{-\infty}^{\infty} d\omega \frac{\mathbf{d}_\alpha^* \text{Im}\{\bar{G}^{rd}(\mathbf{r}_\alpha, \mathbf{r}_\beta, \omega)\} \mathbf{d}_\beta^T}{\omega - \omega_a} + \frac{\omega_a^2}{\hbar\epsilon_0 c^2} \mathbf{d}_\alpha^* \bar{G}^{0\parallel}(\mathbf{r}_\alpha, \mathbf{r}_\beta, \omega_a) \mathbf{d}_\beta^T. \quad (4.2)$$

Due to the complicated frequency dependence of the imaginary part of the radiation Green's tensor, an analytical treatment of the principal value integral in equation (4.2) is nontrivial and requires the introduction of branch cuts and the application of contour integration techniques [55]. Due to these complications, in the literature typically this contribution is approximated by its free-field counterpart, which is known analytically [53, 62] and derived in Section 2.2.1. However, as illustrated by Fig. 4.3, the field might actually be strongly modified by the presence of the nanofiber, and these modifications, even when small, may lead to large differences in observables when treating systems with many emitters. For these reasons, in the following, we describe how to efficiently calculate numerically the value of $V_{\alpha\beta}^{rd}$.

4.3.3 Numerical evaluation of the radiative dipole-dipole interactions

The first challenge one encounters to evaluate numerically the integral in (4.2) is the singularity in the integrand, happening at $\omega = \omega_a$. This singularity can be avoided by using a fast Fourier transform, as introduced in Refs. [145, 146], and using the Schwarz reflection principle, such that $V_{\alpha\beta}^{rd}$ may be written as

$$V_{\alpha\beta}^{rd} = \frac{2\omega_a^2}{\pi\hbar\epsilon_0 c^2} \left[\int_0^\infty d\omega \mathbf{d}_\alpha^* \text{Im}\{\bar{G}^{rd}(\mathbf{r}_\alpha, \mathbf{r}_\beta, \omega)\} \mathbf{d}_\beta^T \int_0^\infty d\tau \cos(\omega_a \tau) \sin(\omega \tau) \right. \\ \left. + \frac{\pi}{2} \mathbf{d}_\alpha^* \bar{G}^{0\parallel}(\mathbf{r}_\alpha, \mathbf{r}_\beta, \omega_a) \mathbf{d}_\beta^T \right]. \quad (4.3)$$

However, the main obstacle for the calculation of $V_{\alpha\beta}^{rd}$ lies in the imaginary part of the Green's tensor, in particular in its behavior at large values of ω . To illustrate this, let us consider again the Green's tensor in vacuum (2.15). In the limit of large ω compared to the separation $r_{\alpha\beta} = |\mathbf{r}_\alpha - \mathbf{r}_\beta|$, i.e. when $kr_{\alpha\beta} \gg 1$, the imaginary part of this tensor yields

$$\text{Im}\{\bar{G}^0(\mathbf{r}_\alpha, \mathbf{r}_\beta, \omega)\} \approx \frac{1}{4\pi r_{\alpha\beta}} \left[(\mathbb{1} - 3\hat{\mathbf{r}}_{\alpha\beta}^2) \frac{\cos kr_{\alpha\beta}}{kr_{\alpha\beta}} + (\mathbb{1} - \hat{\mathbf{r}}_{\alpha\beta}^2) \sin kr_{\alpha\beta} \right].$$

Here we can see that the integrand in the frequency integral in (4.3) for large $\omega \gg \omega_a$ is an oscillating function with period proportional to $\omega_a \lambda_a / r_{\alpha\beta}$, where $\lambda_a = \frac{2\pi c}{\omega_a}$ is the transition wavelength. The amplitude of the oscillations either decays very slowly, as $1/\omega$ (e.g. in vacuum when the dipoles are aligned with the displacement vector, i.e. $|\hat{\mathbf{d}}_\alpha \cdot \hat{\mathbf{r}}_{\alpha\beta}| = 1$, see Fig. 4.4a), or is constant. In the former case, reaching convergence of the integral over frequency requires then an extremely high cut-off frequency $\omega_c \gg \omega_a \lambda_a / r_{\alpha\beta}$, which grows the closer the emitters are to each other. Moreover, in general, even a large value for ω_c does not necessarily ensure convergence (see e.g. Fig. 4.4b for emitters in the free-field with $|\hat{\mathbf{d}}_\alpha \cdot \hat{\mathbf{r}}_{\alpha\beta}| = 0$, where the amplitude of the oscillations remains constant for large ω).

In addition to this issue, note that for the numerical calculation of the imaginary part of the Green's tensor in the presence of the cylindrical nanofiber, in principle an infinite sum of modes m should be considered. In practice, the sum is truncated at some finite value m_c . However, for a fixed distance of the emitters with respect to the nanofiber surface, the amount of modes necessary to ensure convergence grows dramatically with increasing ω . This means that the computational cost of increasing the cut-off frequency is enormous. In order to circum-

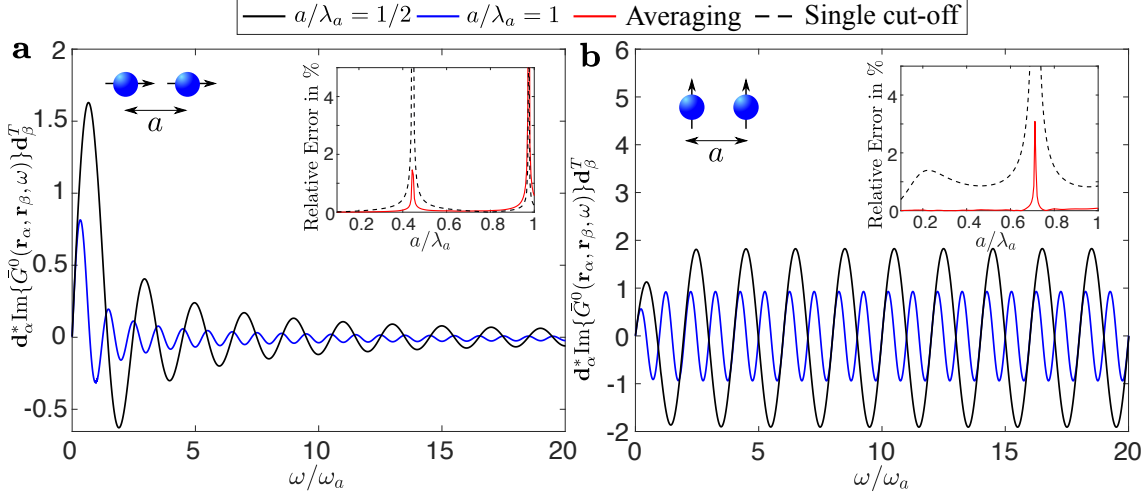


Figure 4.4: *Numerical integration.* Imaginary part of the Green's tensor in vacuum (in arbitrary units) as a function of ω/ω_a for two dipoles at a distance a from one another pointing parallel (a) and perpendicular (b) to the displacement vector between them for $a/\lambda_a = 1$ and $a/\lambda_a = 1/2$ (black and blue solid lines, respectively). The insets show the relative error in % when calculating the vacuum dipole-dipole interaction $V_{\alpha\beta}^0$ as a function of a/λ_a by using a direct numerical integration with a single cut-off frequency $\omega_c/\omega_a = 10\lambda_a/a$ (black dashed) and using the averaging method with a range of cut-offs $\omega_c/\omega_a \in [2\lambda_a/a, 10\lambda_a/a]$. The sharp peaks occur at the zeros of $V_{\alpha\beta}^0$.

vent this problem, we make use of the periodic nature of the integrand in the limit of large ω . This allows us to approximate the result of the frequency integral as the average of the outcomes for a range of cut-off frequencies comprising a few oscillations. This results in a much faster convergence of the integral when the integrand decays as $1/\omega$, as the maximum cut-off frequency necessary for convergence is relatively low. Most importantly, when the amplitude of the oscillations remains constant, this allows to obtain convergence, which would remain otherwise elusive.

In order to illustrate the power of this approach, we have applied it to calculate numerically the dipole-dipole interactions in vacuum. We show in the insets of Fig. 4.4 the relative error of the numerical calculation compared to the exact one (known analytically in this case), using a "single cut-off" direct integration of (4.2) and an "averaging" method for the frequency integration in expression (4.3). It is evident that the second approach gives dramatically better results, particularly when the dipoles are perpendicular to their displacement vector. This encourages us to apply this numerical method to the nanofiber case, where the main features of the Green's tensor as a function of the frequency are similar to the vacuum ones. Note that the sharp peaks in the errors occur due to the van-

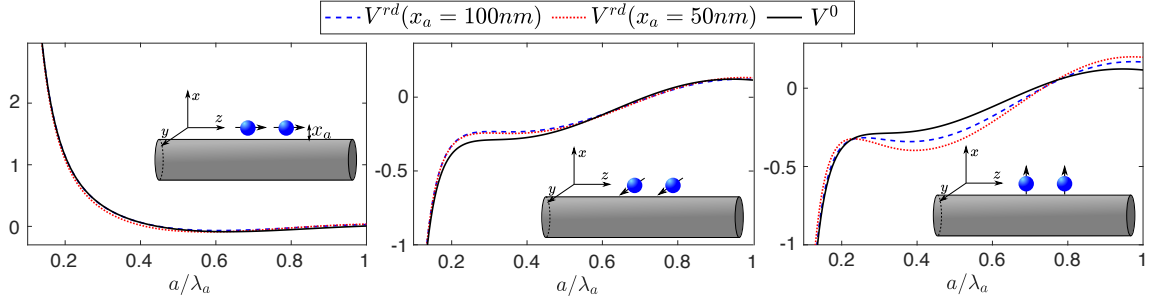


Figure 4.5: *Modified dipole-dipole interactions.* The radiation contribution to the dipole-dipole interaction V^{rd} (in units of the single particle decay rate γ) for a distance of $x_a = 50$ nm (red dotted) and $x_a = 100$ nm (blue dashed) from the fiber surface as a function a/λ_a . The black solid line is the analytic solution in the case of vacuum. Each panel displays the results for a different orientation of the dipoles with respect to the surface of the nanofiber: parallel, binormal and normal for the upper, middle and lower panel, respectively. The parameters are identical to those used in Fig. 4.3.

ishing dipole-dipole interaction at these particular values of the separation a .

4.3.4 Modified dipole-dipole interaction between two atoms near a nanofiber

We apply here the numerical method presented above to the simple case of two identical two-level atoms placed at a fixed distance from the fiber surface x_a , fixed azimuthal angle $\phi = 0$ and fixed separation a . Figure 4.5 shows the radiation contribution to the dipole-dipole interaction V^{rd} for distances $x_a = 50$ nm and $x_a = 100$ nm from the fiber surface compared to the vacuum counterpart V^0 as a function of a/λ_a for three different dipole orientations. The dipole-dipole interaction in all cases is normalized by the single-atom spontaneous decay rate in vacuum, $\gamma = |\mathbf{d}|^2 \omega_a^3 / (3c^3 \pi \epsilon_0 \hbar)$.

As expected from the results for the imaginary part of the Green's tensor (Fig. 4.3), the most important modifications of the dipole-dipole interactions are found when the atomic dipole moment orientation is perpendicular to both the axis and the surface of the nanofiber (bottom panel). Here, the differences between the calculated radiation components and their vacuum counterparts are not only large (e.g., 70% difference at $a/\lambda_a = 1$), but also persist at large distances between the atoms i.e. at $a \geq \lambda_a$.

Finally, to further illustrate the power of our approach, let us consider a pair of dipoles separated by $a = \lambda$ parallel to the displacement vector (Figs. 4.4a and 4.5a). Using our numerical method, here we calculate the vacuum interaction to a precision of 0.004% error using an upper cut-off frequency of $\omega_c = 10\omega_a$.

To get the same precision using a standard numerical integration method, a cut-off frequency of $\omega_c = 40\omega_a$ would be needed. For $\omega = 10\omega_a$ we have to include around $m_c = 90$ modes, while for $\omega = 40\omega_a$ around 260 modes are needed (needing about six times longer to calculate the imaginary part of the Green's tensor at that frequency point alone).

4.4 Effect of the collective interaction on the transmission of fiber-guided light

The effect of the modifications that we find in the dipole-dipole interaction between a pair atoms becomes greatly amplified when considering observables in a large ensemble of many emitters. The key to understand this amplification is that the emitters couple *collectively* to its environment. This in turn means that each of the N^2 terms $V_{\alpha\beta}$ and $\Gamma_{\alpha\beta}$ of the dipole-dipole and dissipation matrices play a role in the (collective) coherent and incoherent dynamics of the system. Hence, small variations of the coefficients $V_{\alpha\beta}$ and $\Gamma_{\alpha\beta}$ in the master equation (2.1) have a large effect on observables such as the photon emission rate or the spectrum of the light that is absorbed and emitted from the ensemble.

We illustrate this now by investigating the transmission signal of fiber-guided light when a periodic chain of N atoms is placed in the vicinity of the fiber surface (see Fig. 4.6). Here, in the cylindrical coordinate system, the coordinates of atom α are given by $\mathbf{r}_\alpha = (x_\alpha, 0, (\alpha - 1)a)$. The system is driven by a weak probing field of frequency ω_p detuned from the atomic resonance frequency by the detuning $\Delta = \omega_p - \omega_a$ and with Rabi frequency Ω and the driving term is given by

$$\hat{H}_{\text{Drive}} = -\hbar \sum_{\alpha} [\Delta \hat{\sigma}_{\alpha}^{\dagger} \hat{\sigma}_{\alpha} + \Omega e^{i\beta z_{\alpha}} \hat{\sigma}_{\alpha}^{\dagger}].$$

The light field enters the nanofiber from its left, is guided through the nanofiber, interacts with the atomic chain, and its transmitted signal is measured at a position z to the right of the chain in the fiber as [37, 55]

$$T = \frac{\langle \psi | \hat{E}_R^{g\dagger}(z) \hat{E}_R^{g\dagger}(z) | \psi \rangle}{\Omega^2}. \quad (4.4)$$

Here $\hat{E}_R^{g\dagger}$ is the right propagating component of the guided probe field, given by a sum of the input and scattering components as

$$\hat{E}_R^{g\dagger}(z) = \Omega e^{i\beta z} + i \frac{\gamma^{gd}}{2} \sum_{\alpha=1}^N \Theta(z - z_{\alpha}) e^{i\beta(z - z_{\alpha})} \hat{\sigma}_{\alpha},$$

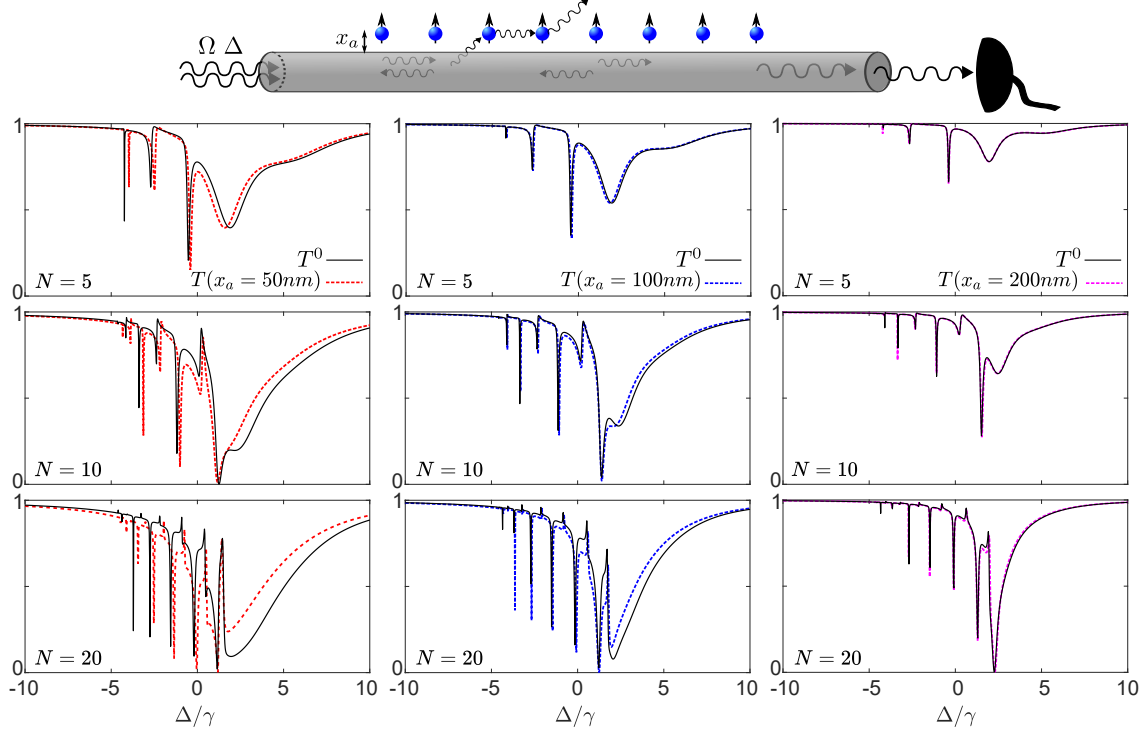


Figure 4.6: *Modified transmission signal.* Transmission signal T in the stationary state of fiber-guided light driving the atoms with Rabi frequency $\Omega = 0.1\gamma$ and detuning Δ for a chain of N atoms with lattice constant $a = 0.1\lambda_a$ placed at a distance x_a from the surface of the nanofiber. The black solid line represents the transmission T^0 using the vacuum instead of the full radiation dipole-dipole interactions.

where $\gamma^{gd} = \Gamma_{\alpha\alpha}^{gd}$ is the single-atom decay rate of each atom into the guided modes.

In the single excitation sector, the atomic wave function may be written as $|\psi(t)\rangle = c_G(t)|G\rangle + \sum_{\alpha=1}^N c_e^\alpha(t)|e_\alpha\rangle$, where $|G\rangle = |g_1\rangle \otimes |g_2\rangle \dots |g_N\rangle$ and $|e_\alpha\rangle = |g_1\rangle \dots \otimes |e_\alpha\rangle \otimes \dots |g_N\rangle$ [31, 147]. In the low saturation regime (weak probe laser), $c_G(t) \approx 1$, and inserting the ansatz into the master equation (2.1), the time evolution of the probability amplitude coefficients $c_e^\alpha(t)$ can be found to be determined by

$$\dot{c}_e(t) = i \left(\Delta + i \frac{\Gamma}{2} - \frac{1}{\hbar} \hat{H}^{\text{eff}} \right) c_e(t) + i\eta,$$

where the components of η are $\eta_\alpha = \Omega e^{i\beta z_\alpha}$ and $\Gamma = \Gamma_{\alpha\alpha}$ is the total single-atom decay rate (sum of the decay rates into guided and radiation modes). Finally, the effective Hamiltonian \hat{H}^{eff} given by

$$\hat{H}_{\alpha\beta}^{\text{eff}} = -\hbar \left(V_{\alpha\beta} + i \frac{\Gamma_{\alpha\beta}}{2} \right),$$

has been introduced for $\alpha \neq \beta$.

In Figure 4.6, we show the guided light transmission signal (4.4) as a function of Δ in the stationary state [where $\dot{c}_e(t) = 0$] when a periodic chain of $N = 5, 10$ and 20 atoms with nearest neighbor separation $a/\lambda_a = 0.1$ is placed at $x_a = 50, 100$ and 200 nm from the surface of the nanofiber. We compare in all cases the transmission with the result obtained under the approximation that the radiation component of the dipole-dipole interaction is given by the free-field $V_{\alpha\beta}^0$. One can easily observe here that indeed large deviations arise in the transmission spectrum. These differences become more evident the closer the atoms are to the nanofiber (where each element $V_{\alpha\beta}^{rd}$ differs more from $V_{\alpha\beta}^0$, see Fig. 4.5) and the larger the number N of atoms in the chain (where more elements $V_{\alpha\beta}^{rd}$ participate in the collective dynamics). In all cases one can observe, not only measurable shifts of the (subradiant) narrow and (superradiant) broad resonance peaks, but an overall deformation of the spectrum as N increases. Note, that in current experiments typically several hundreds of atoms can be trapped near the nanofiber [148], making the spectra differ even more substantially.

4.5 Conclusions and outlook

We have provided a detailed recipe for the analytical and numerical calculation of the interaction of an ensemble of emitters in the presence of a cylindrical nanofiber. In particular, we have shown that the dipole-dipole interactions mediated by the radiation modes outside the nanofiber differ significantly (up to a 70% in some of the cases considered) from the ones obtained in vacuum, specially when the emitters' transition dipole moments are oriented normal or binormal to the fiber surface. These differences affect substantially the collective properties of the system, such as the transmission signal of fiber-guided light, where large shifts in the resonances are observed as the number of emitters is increased. Note, however, that we have calculated the transmission in the single-excitation limit (linear optics regime). Beyond this limit, we expect that, while features related to superradiance will not dramatically affected by modifications in the dipole-dipole interactions [149], these will become crucial when studying the excitation and description of many-body long-lived (subradiant) states, e.g. for the realisation of quantum memories [150, 151].

Chapter 5

Topological photon pumping

5.1 Introduction

Topological pumping is a way of obtaining controlled and robust transport of particles in quantum systems through a slow modulation of the Hamiltonian parameters. So far, topological pumping has only been demonstrated in systems with short-range couplings, typically only nearest neighbour. In this work, we investigate and obtain the conditions necessary to realize topological pumping in systems with long-range couplings.

We start by deriving the equation for the displacement after a completed pumping cycle for an initial state, which is a superposition of Bloch waves with an arbitrary weight for each quasi-momenta. We find that this displacement can be either smaller, larger or equal to the Chern number of the relevant band. We discuss the dispersion of the initial state in the pumping cycle and present the criterion for dispersionless topological pumping based on the so-called time-integrated Berry curvature.

In the following section, we introduce the idea of topological pumping of a photon embedded in a quantum optical system consisting of a 1D chain of two-level emitters coupled to a common environment giving rise to long-range dipole-dipole interactions. We show that, in the single excitation regime, the Hamiltonian governing the dynamics of the system can be mapped onto an extended version of the Rice-Mele model with, in general, all-to-all couplings. We introduce three experimentally relevant quantum optical platforms to study topological pumping with different degrees of "long-rangeness" in the interactions. These are: Rydberg atom chains with short-range interactions, atoms in free space with long-range interactions and atoms coupled to a nanophotonic waveguide with all-to-all interactions. We show that topological pumping can be performed in each of the three systems with high fidelity, i.e. with low dispersion, over mul-

tiple pumping cycles.

Finally, we discuss and compare the robustness against dissipation and disorder for the three systems. We show that the pumping cycle can be performed well within the lifetime of the Rydberg atoms. Furthermore we show that the state of the atoms in free space and the atoms coupled to a waveguide can be made subradiant during the whole pumping cycle. All the systems show remarkable robustness against local disorder in the emitter positions resulting in high fidelity pumping in each system.

5.2 Topological pumping in one dimension with arbitrary initial state

In Section 3.4 we discussed the foundational theory of topological pumping in a one dimensional system, where after an adiabatic cycle of the Hamiltonian parameters yielded a displacement the initial state of a integer number of lattice sites. However, the quantized displacement is only guaranteed if the initial state is a uniform distribution in k -space translating to a single unit cell occupancy in real space. As we will see in the next section, for quantum optical systems, a uniform distribution in k -space will lead to dispersion of the initial state during the pumping cycle resulting in low fidelity pumping. To circumvent this issue, we will consider non-uniform distribution of the initial state in momentum space, which requires a slight modification to the equation for the displacement after one completed cycle given in equation (3.16).

We consider a one-dimensional system governed by a generic Hamiltonian \hat{H} that hosts topological phases. The parameters of the Hamiltonian can be varied in time, and we consider a cyclic variation such that at the end of the cycle with period T the Hamiltonian is again the initial one, i.e., $\hat{H}(t = T) = \hat{H}(t = 0)$. Furthermore, we consider an adiabatic evolution, such that after each cycle the initial state $|\Psi_0\rangle = \sum_m f_m |u_m(t=0)\rangle$, which is a superposition of the Hamiltonian's eigenstates $|u_m(t=0)\rangle$ with amplitude f_m , reaches a final state that reads $|\Psi_T\rangle = \sum_m f_m e^{i\gamma_m} |u_m(t=0)\rangle$. As discussed in Section 3.2, the initial state will pick up a Berry phase after a completed cycle given by

$$\gamma_m = i \int_0^T dt \langle u_m(t) | \partial_t u_m(t) \rangle, \quad (5.1)$$

where $|u_m(t)\rangle$ are the instantaneous eigenstates of the Hamiltonian. This geometric phase can cause a displacement of the average position of the state in real space after the cycle given by $\Delta x = \langle \hat{x} \rangle_T - \langle \hat{x} \rangle_0$, where $\langle \hat{x} \rangle_t \equiv \langle \Psi_t | \hat{x} | \Psi_t \rangle$, which

constitutes the so-called charge pumping.

In this work we consider one-dimensional lattice systems with spatial period a . The eigenstates of the Hamiltonian are Bloch waves of the form $|\psi_{kn}(x, t)\rangle \propto e^{ikx}|x\rangle \otimes |u_{kn}(t)\rangle$, parametrized by their band index n and the crystal quasi-momentum k . Here, $|x\rangle$ is the position eigenstate ($\hat{x}|x\rangle = x|x\rangle$), and $|u_{kn}(t)\rangle$ the cell-periodic part of the wave function. We consider the state of the system throughout the dynamics to be a superposition of Bloch waves, i.e.

$$|\Psi_t(x)\rangle = \frac{1}{\sqrt{N}} \sum_{k=-\pi/a}^{\pi/a} f(k) |\psi_{kn}(x)\rangle,$$

where N is the number of unit cells, $f(k)$ is the quasi-momentum distribution normalized such that

$$\int_{\text{FBZ}} |f(k)|^2 dk = \frac{2\pi}{a},$$

and

$$|\psi_{kn}(x)\rangle = \frac{1}{\sqrt{N}} e^{ikx} |x\rangle \otimes |u_{kn}(t)\rangle.$$

In the limit of an infinite system, i.e., $N \rightarrow \infty$, k becomes a continuous variable. Thus, we can substitute the sum over k , $\sum_{k=-\pi/a}^{\pi/a}$, by the corresponding integral, $\frac{Na}{2\pi} \int_{\text{FBZ}} dk$, such that the state reads

$$|\Psi_t(x)\rangle = \frac{a}{2\pi} \int_{\text{FBZ}} dk f(k) e^{ikx} |x\rangle \otimes |u_{kn}(t)\rangle.$$

The expectation value of the position as a function of time is given by

$$\begin{aligned} \langle \hat{x} \rangle_t &= \sum_{x=-\infty}^{\infty} \langle \Psi_t(x) | \hat{x} | \Psi_t(x) \rangle \\ &= \left(\frac{a}{2\pi} \right)^2 \sum_x \int_{\text{FBZ}} \int_{\text{FBZ}} dk dk' f(k) f^*(k') \times \langle u_{nk'}(t) | x e^{ix(k-k')} | u_{kn}(t) \rangle. \end{aligned}$$

Using partial integration we get

$$\begin{aligned} \langle \hat{x} \rangle_t &= i \left(\frac{a}{2\pi} \right)^2 \sum_x \int_{\text{FBZ}} dk' f^*(k') \langle u_{nk'}(t) | e^{-ik'x} \\ &\quad \times \int_{\text{FBZ}} dk e^{ikx} \{ [\partial_k f(k)] |u_{kn}(t)\rangle + f(k) \partial_k |u_{kn}(t)\rangle \}. \end{aligned}$$

Using the Fourier decomposition of the Dirac delta function $\sum_{x=-\infty}^{\infty} e^{i(k-k')x} = \frac{2\pi}{a} \delta(k - k')$, we obtain

$$\langle \hat{x} \rangle_t = \frac{ia}{2\pi} \int_{\text{FBZ}} dk \left[f^*(k) \partial_k f(k) + |f(k)|^2 \langle u_{kn}(t) | \partial_k u_{kn}(t) \rangle \right].$$

After one full cycle of time T , the center of mass of the wave packet is displaced by

$$\Delta x = \langle \hat{x} \rangle_T - \langle \hat{x} \rangle_0 = \frac{a}{2\pi} \int_{\text{FBZ}} dk |f(k)|^2 [A_{kn}(T) - A_{kn}(0)],$$

where we have introduced the Berry connection $A_{kn}(t) = i \langle u_{kn}(t) | \partial_k u_{kn}(t) \rangle$. Considering that, after a full adiabatic cycle, the time-evolved eigenstates only pick up a phase, i.e. $|u_{kn}(T)\rangle = e^{i\gamma(k)}|u_{kn}(0)\rangle$, where

$$\gamma(k) = i \int_0^T dt \langle u_{kn}(t) | \partial_t u_{kn}(t) \rangle, \quad (5.2)$$

as introduced in (5.1), is the geometric Berry phase for eigenstates in momentum space. Using this, one can easily find that

$$\Delta x = -\frac{a}{2\pi} \int_{\text{FBZ}} |f(k)|^2 \partial_k \gamma(k) dk.$$

Making use of the relation between Berry phase and Berry curvature Ω_{kt}

$$\mathcal{W}_k^n \equiv \int_0^T dt \Omega_{tk}^n = -\partial_k \gamma(k), \quad (5.3)$$

we arrive at the final expression for the displacement

$$\Delta x = \frac{a}{2\pi} \int_{\text{FBZ}} |f(k)|^2 \mathcal{W}_k^n dk, \quad (5.4)$$

where we have defined time-integrated Berry curvature \mathcal{W}_k^n . In the limit of a uniformly filled band, i.e. $|f(k)|^2 = 1$, the above expression for the displacement reduces to the standard one given in (3.16). The displacement for a general $f(k)$ can either be smaller or larger than the Chern number of the relevant band depending on the specific shape of the Berry curvature as a function of the quasi-momentum k and time t .

Note that, in general, also a dynamical phase may be present, which is proportional to the usual group velocity. This in turn may lead to a further displacement of the average position, given by the convolution of the group velocity with the quasi-momentum distribution, integrated over the FBZ. In this work, however, we are interested in the *anomalous displacement* arising from the topological properties and an adiabatic change of the system. We keep this effect dominant by restricting ourselves to symmetric wave packets placed in the center of the FBZ of a time-reversal symmetric Hamiltonian, which leads to a zero contribution to the displacement of the dynamical phase.

5.2.1 Topological pumping and dispersion

While equation (5.4) tells us about the displacement of the center of mass of a given initial state, it does not contain any other information about its evolution in real space. However, in this work we are not only interested in realizing topological charge pumping of the center of mass, but we aim to realize this in a dispersionless way, i.e. keeping the value of the fidelity $\mathcal{F}(T) = |\langle \Psi_0(x + \Delta x) | \Psi_T(x) \rangle|^2$ as close to one as possible. Hence, here we analyze this dispersion for different combinations of initial states and Berry curvatures.

Let us start by analysing the dispersion of the initial wave packet in real space $|\Psi_0(x)\rangle \propto \sum_k f(k) |\psi_{kn}(x, 0)\rangle$. After a full period, the state becomes $|\Psi_T(x)\rangle \propto \sum_k f(k) e^{i\gamma(k)} |\psi_{kn}(x, 0)\rangle$, where the Berry phase $\gamma(k)$ is defined in equation (5.2). Importantly, note that if this phase is linear in k , i.e. $\gamma(k) \approx k\Delta x$, for all k where $f(k) \neq 0$, then $|\Psi_T(x)\rangle \approx |\Psi_0(x + \Delta x)\rangle$, so that the wave function remains unchanged except for a shift of its center. Otherwise, the wave packet disperses and the fidelity quickly drops below one. Since the time-integrated Berry curvature \mathcal{W}_k^n is directly given by the gradient of the Berry phase (see (5.3)), the dispersion of the wave packet is minimal when the integrated Berry curvature is constant, or ‘flat’ in quasi-momentum space.

For the standard case of topological pumping the initial state is such that $|f(k)|^2$ constant for all k (Fig. 5.1a) [152, 153], the charge displacement is quantized in the form of $\Delta x = aC_n$. However, in general, \mathcal{W}_k^n is not flat, which leads to a quick dispersion of an initially localized wave packet in real space (see Fig. 5.1b). Conversely, as discussed above, if \mathcal{W}_k^n is constant throughout the full FBZ (see Fig. 5.1c), quantized and dispersionless pumping will be achieved independently of the specific shape of the wave packet in k space (see Fig. 5.1d). This is, however, hard to achieve in practice in a real physical system, and even harder for a long-ranged Hamiltonian, which develops sharp structures in the Berry curvature.

In this work, we resort to an intermediate approach, typically called *geometric pumping* [127]. For each system, we identify a path that leads to a time-integrated Berry curvature \mathcal{W}_k^n that is constant *on a finite region of the FBZ*. We consider then a localized quasi-momentum distribution $f(k)$ such that $f(k) \neq 0$ only in the region where \mathcal{W}_k^n is constant (see Fig. 5.1e) [128]. This condition is much easier to fulfill than a fully flat \mathcal{W}_k^n [153], and allows an approximately dispersionless transport of the wave packet in real space. Instead of obtaining a displacement Δx that is quantized, its value will depend on the specific geometrical properties of the underlying Hamiltonian (e.g., short versus long-ranged) as well as on the choice of the pumping cycle, since this determines the shape and value of \mathcal{W}_k^n (see Fig. 5.1f). By choosing different protocols one can then achieve dispersionless

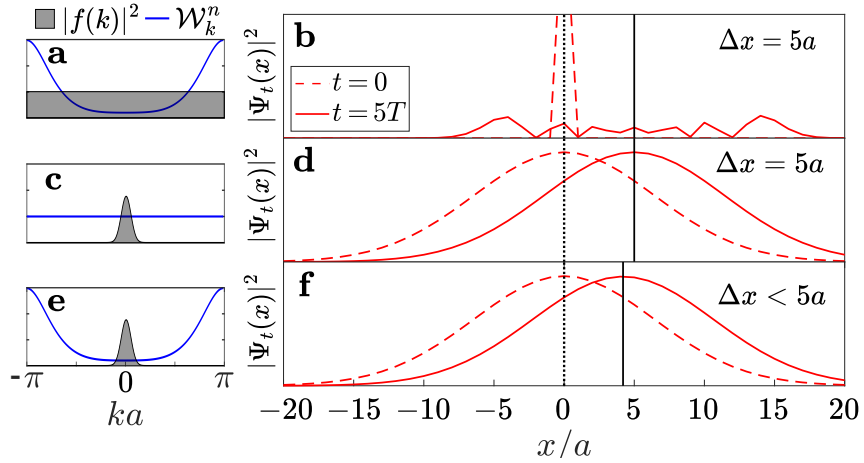


Figure 5.1: *Topological pumping and dispersion.* **Left column:** Time-integrated Berry curvature \mathcal{W}_k^n and quasi-momentum distribution density $|f(k)|^2$. **Right column:** Spatial probability density of the state, $|\Psi_t(x)|^2 \equiv \langle \Psi_t(x) | \Psi_t(x) \rangle$, at times $t = 0$ and $t = 5T$, obtained from the numerical simulation of the Schrödinger equation under a time-dependent Rice-Mele Hamiltonian, with the quasi-momentum distribution density and time-integrated Berry curvature shown in the corresponding left panel. The vertical points and solid lines indicate the center of mass of the wave packet at $t = 0$ and $5T$, respectively. **a** and **b**: In standard topological pumping, where the band is uniformly filled, the non-flat shape of \mathcal{W}_k^n across the FBZ leads to dispersion of the wave packet in real space. Dispersionless topological pumping can be achieved either by making \mathcal{W}_k^n constant (**c** and **d**), or by constraining $|f(k)|^2$ to a domain in momentum space where \mathcal{W}_k^n is approximately constant (**e** and **f**).

transport of the wave packet where Δx is larger or smaller than the one achieved in topological pumping.

5.3 Long-range hopping in quantum optics: the extended Rice-Mele model

In this work we focus on the realization of topological pumping using quantum optics platforms and, in this section, we present the general equation that describes the dynamics of these systems. We then introduce a mapping onto a generalized version of the Rice-Mele model with long-range hopping parameters, which we refer to as the *extended Rice-Mele model*, and discuss its topological properties.

All three quantum optics platforms we discuss here share the following description (see Fig. 5.2a): An ensemble of N two-level emitters in the Lamb-Dicke regime with ground state $|g\rangle$ and excited state $|e\rangle$ separated by an energy $\hbar\omega_a$, are

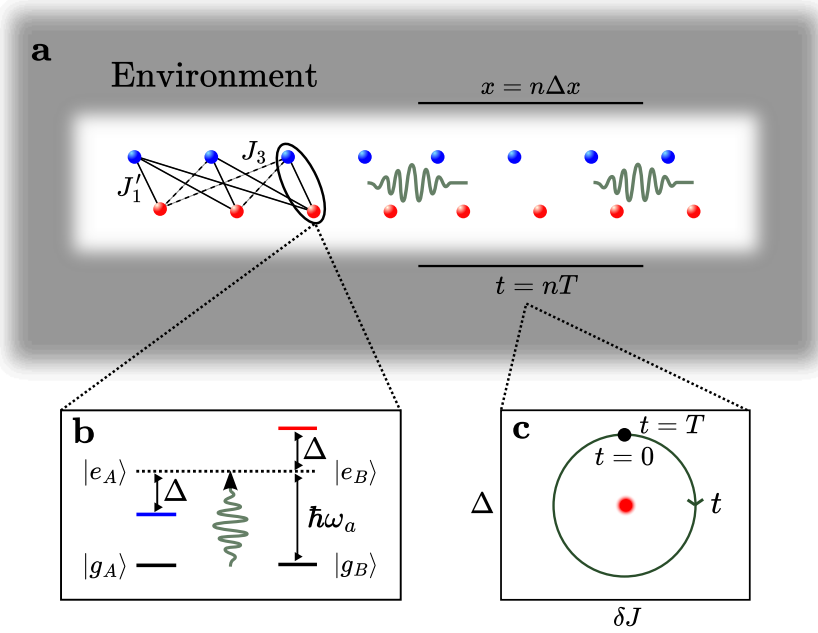


Figure 5.2: *Topological photon pumping on a quantum optical system.* **a:** All systems we consider can be generally described as a one-dimensional chain of emitters coupled to a common (Markovian) environment. The chain is formed by $N/2$ unit cells with two sublattices, A and B (blue and red, respectively). **b:** The emitters are considered to be identical two-level systems with ground ($|g\rangle$) and excited ($|e\rangle$) states separated by an energy $\hbar\omega_a$. **c:** By varying time-dependently the parameters of the system (here generically called Δ and δJ) in a periodic manner around a topological degeneracy point (red dot), a single photon is transported (topologically pumped) across the lattice minimizing its dispersion.

coupled to a common environment. Within the approximation outlined in Section 2.1, the quantum master equation that describes the evolution of the emitter's internal degrees of freedom is

$$\dot{\hat{\rho}} = -\frac{i}{\hbar} [\hat{H}, \hat{\rho}] + \mathcal{D}(\hat{\rho}), \quad (5.5)$$

where $\hat{\rho}$ is the density operator. The first term of this master equation represents the coherent evolution of the system under the Hamiltonian $\hat{H} = \hat{H}_{dd} + \hat{H}_\Delta$, which reads

$$\hat{H} = \hbar \sum_{i \neq j=1}^N V_{ij} \hat{\sigma}_i^\dagger \hat{\sigma}_j + \hbar \Delta \sum_{j=1}^N (-1)^j \hat{\sigma}_j^\dagger \hat{\sigma}_j, \quad (5.6)$$

with the spin-1/2 ladder operators $\hat{\sigma}_i = |g_i\rangle \langle e_i|$ and $\hat{\sigma}_i = |e_i\rangle \langle g_i|$. This Hamiltonian drives an exchange (dipole-dipole) interaction between the emitters. The strength and range of the exchange, encoded in the matrix elements V_{ij} , will be determined by the Green's tensor, which depends on the specific system at hand as outlined in Section 2.2. The second term, \hat{H}_Δ , is an on-site potential, which

leads to an offset $2\hbar\Delta$ between even and odd sites (see Fig. 5.2b). The dissipation in the system (second term of the master equation) also depends on the system at hand, and its action on the dynamics will be considered separately for each system in Sec. 5.5.1.

We assume that the emitters are placed on a bipartite one-dimensional lattice (see Fig. 5.2a). A Jordan-Wigner transformation of the form

$$\hat{\sigma}_j = e^{i\pi \sum_{l=1}^{j-1} \hat{f}_l^\dagger \hat{f}_l} \hat{f}_j, \quad (5.7)$$

$$\hat{\sigma}_i^\dagger = e^{-i\pi \sum_{l=1}^{i-1} \hat{f}_l^\dagger \hat{f}_l} \hat{f}_i^\dagger, \quad (5.8)$$

allows us to express the spin operators in terms of the spinless fermionic creation and annihilation operators \hat{f}_l^\dagger and \hat{f}_l , respectively. Applying this transformation to Hamiltonian (5.6), and imposing the constraint of staying in the single excitation (fermion) sector, it becomes

$$\hat{H} = \hbar \sum_{i \neq j=1}^N V_{ij} \hat{f}_i^\dagger \hat{f}_j + \hbar\Delta \sum_{j=1}^N (-1)^j \hat{f}_j^\dagger \hat{f}_j. \quad (5.9)$$

In the next step, we make the bipartite lattice explicit by denoting $\hat{a}_q = \hat{f}_{2q-1}$ and $\hat{b}_q = \hat{f}_{2q}$ where $q = 1 \dots N/2$ labels the unit cells. Accordingly, we categorize V_{ij} into three different hopping parameters: from sublattice A to B, from B to A, and within the same sublattice, which we denote J'_{2p-1} , J_{2p-1} and J_{2p} , respectively, where p denotes again the unit cell (see Fig. 5.4a). The extended Rice-Mele Hamiltonian is then given by

$$\begin{aligned} \hat{H} = \hbar & \left\{ \sum_{q=1}^{N/2} \sum_{p=1}^{N/2-q} \left[J'_{2p-1} \hat{a}_q^\dagger \hat{b}_{q+p-1} + J_{2p-1} \hat{b}_q^\dagger \hat{a}_{q+p} + J_{2p} (\hat{a}_q^\dagger \hat{a}_{p+q} + \hat{b}_q^\dagger \hat{b}_{p+q}) \right] \right. \\ & \left. + J'_{N-1} \hat{a}_1^\dagger \hat{b}_{N/2} + \text{h.c.} \right\} + \hbar\Delta \sum_{q=1}^{N/2} (\hat{a}_q^\dagger \hat{a}_q - \hat{b}_q^\dagger \hat{b}_q). \end{aligned} \quad (5.10)$$

Note that, when restricting hopping to solely nearest neighbors, this Hamiltonian reduces to the standard Rice-Mele mode discussed in Section 3.4.

5.3.1 Topological properties of the extended Rice-Mele model

Let us here analyze the bulk properties of the extended Rice-Mele model. Considering periodic boundary conditions, Hamiltonian (5.10) may be written

in terms of its irreducible matrix form in momentum space $h(k)$ as

$$\hat{H} = \sum_{\substack{k \in FBZ \\ \alpha, \beta \in A, B}} \hat{c}_\alpha^\dagger(k) h_{\alpha\beta}(k) \hat{c}_\beta(k), \quad (5.11)$$

where

$$\hat{c}_\alpha(k) = \frac{1}{\sqrt{\lfloor N/4 \rfloor}} \sum_{p=1}^{\lfloor N/4 \rfloor} e^{-ikpa} \hat{c}_\alpha(p), \quad (5.12)$$

with $\hat{c}_A(p) \equiv \hat{a}_p$ and $\hat{c}_B(p) \equiv \hat{b}_p$ and

$$h(k) = \begin{pmatrix} n_0(k) + \hbar\Delta & n(k) \\ n^*(k) & n_0(k) - \hbar\Delta \end{pmatrix}. \quad (5.13)$$

Here, we have defined the functions

$$\begin{aligned} n_0(k) &= 2\hbar \sum_{p=1}^{\lfloor N/4 \rfloor} J_{2p} \cos(kpa), \\ n(k) &= \hbar \sum_{p=1}^{\lfloor N/4 \rfloor} (J_{2p-1} e^{ikpa} + J'_{2p-1} e^{-ik(p-1)a}) \end{aligned} \quad (5.14)$$

that contain the intra-sublattice and inter-sublattice hopping parameters respectively. Diagonalizing $h(k)$ we obtain the dispersion relation $E_\pm(k) = n_0(k) \pm \sqrt{|n(k)|^2 + \Delta^2}$ for the upper (+) and lower (-) band, respectively. The two eigenvectors of $h(k)$ corresponding to the two bands can be expressed as

$$\begin{aligned} |u_{k-}\rangle &= \frac{1}{\mathcal{N}} \begin{pmatrix} n(k) \\ -\sqrt{|n(k)|^2 + \Delta^2} - \Delta \end{pmatrix}, \\ |u_{k+}\rangle &= \frac{1}{\mathcal{N}} \begin{pmatrix} \sqrt{|n(k)|^2 + \Delta^2} + \Delta \\ n(k)^* \end{pmatrix}. \end{aligned} \quad (5.15)$$

Similarly to the standard Rice-Mele model, the extended Rice-Mele Hamiltonian with $\Delta \neq 0$ does not host topological phases. However, for vanishing energy offset $\Delta = 0$, the Hamiltonian reduces to the extended SSH Hamiltonian [71,74]. This Hamiltonian can be allocated to the BDI symmetry class, which possesses a \mathbb{Z} -type topological invariant in one dimension, like the standard SSH model [154], when the sublattice symmetry is conserved, i.e. when $n_0(k) = 0$, which can be accomplished by setting $J_{2p} = 0$ for all p . Note, however, that even though we impose here, where possible, sublattice symmetry, the model described by (5.10) is inversion symmetric and hence $J_{2p} = 0$ is not a necessary condition for the pumping to take place.

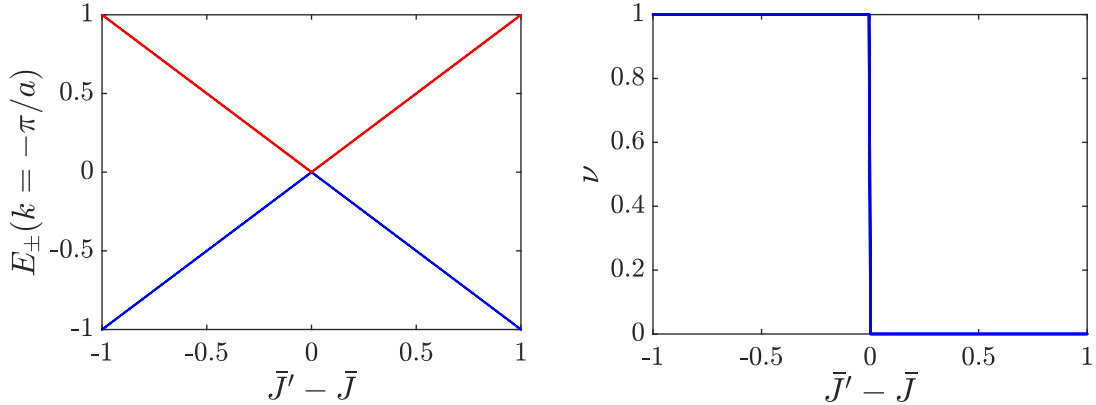


Figure 5.3: *Gap closing and winding number.* **a:** Energy bands E_{\pm} at the edge of the FBZ as a function of the extended hopping parameters. **b** The winding number ν of the extended SSH model as a function of the extended hopping parameters.

To calculate the topological degeneracy points in the extended Rice-Mele model we look for the points in the FBZ where the energy gap closes and the argument of the complex function $n(k)$ is discontinuous. The imaginary part of $n(k)$ is equal to zero when $k = \pm\pi/a$ and $k = 0$. At those points, also the real part of $n(k)$ is zero when

$$\sum_{p=1}^{\lfloor N/4 \rfloor} (-1)^{p+1} (J'_{2p-1} - J_{2p-1}) = 0 \quad (5.16)$$

for $k = \pm\pi/a$ and

$$\sum_{p=1}^{\lfloor N/4 \rfloor} (J'_{2p-1} + J_{2p-1}) = 0 \quad (5.17)$$

for $k = 0$, making the argument of $n(k)$ undefined and the energy gap zero. Note, that there are further specific fine-tuned combinations of the parameters J_{2p-1} and J'_{2p-1} that lead to topological degeneracy points at other points of the FBZ. However, in the pumping cycles and physical systems that we propose in this work the gap only closes at $k = \pm\pi/a$. Thus, we introduce the extended hopping parameters

$$\begin{aligned} \bar{J}' &= \sum_{p=1}^{\lfloor N/4 \rfloor} (-1)^{p+1} J'_{2p-1}, \\ \bar{J} &= \sum_{p=1}^{\lfloor N/4 \rfloor} (-1)^{p+1} J_{2p-1}, \end{aligned} \quad (5.18)$$

and realize cyclic variations in the extended Rice-Mele Hamiltonian parameters such that the curve $\xi(t) = (\Delta, \delta\bar{J} = \bar{J}' - \bar{J})$ encircles the origin. Figure 5.3a shows how the gap closes in the edge of the FBZ ($k = \pm\pi/a$) when $\bar{J}' = \bar{J}$. The closing

of the gap corresponds to a change in the winding number of the extended SSH model as seen in Figure 5.3b.

5.4 Topological photon pumping in quantum optical systems

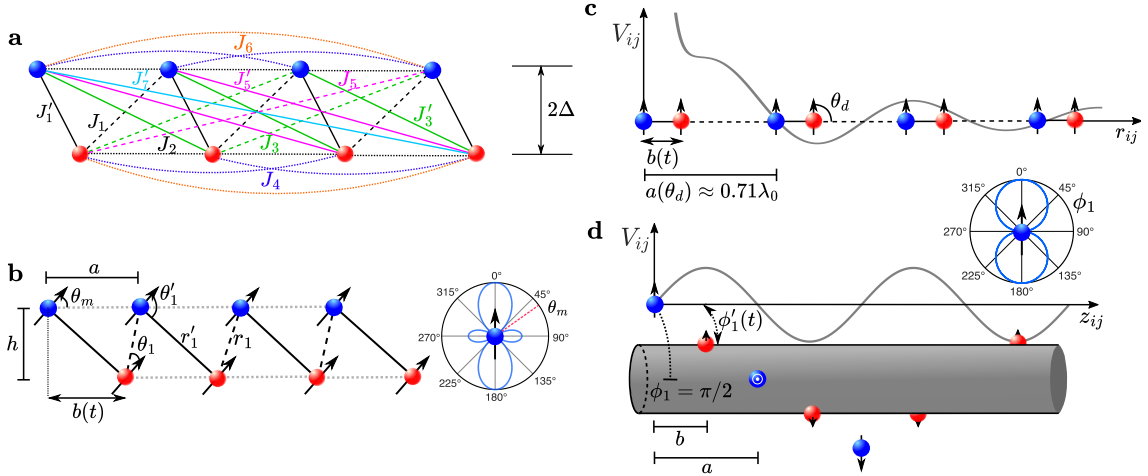


Figure 5.4: *Realizations of the extended Rice-Mele model.* **a:** In the extended Rice-Mele model, we consider in general, non-zero hopping parameters between all sites. Here, an example for a system with $N = 8$ sites. **b:** In the Rydberg system, the two sublattices are separated by a perpendicular distance h and a horizontal offset $b(t)$, which can be changed in time to realize the photon pumping. Here, the nearest neighbor hoppings dominate and we exploit the dependence of the couplings on dipole moment orientation (right panel) to make the intra-sublattice hoppings (J_{2p}) negligible. **c:** Similarly, on a dense chain of atoms excited to low-lying electronic states, J_2 is put to zero by fixing a value of a that depends on the angle θ_d of the dipoles, while the rest of the hoppings (determined by V_{ij}) are non-zero in general. **d:** In a lattice of atoms coupled to a waveguide (here a cylindrical nanofiber), the atoms of sublattice A are fixed forming a helix around the fiber, while the atoms of sublattice B change their relative angle to sublattice A, $\phi'_1(t)$, time-dependently to realize the pumping. Sublattice symmetry is preserved by choosing $a = \pi/\beta$, where β is the wave vector of the light propagating inside the fiber.

Having set up the stage for the realization of dispersionless topological pumping in the extended Rice-Mele model (see Fig. 5.4a), we now examine three quantum optics platforms of current experimental relevance. These platforms enable the pumping of photons stored in the excited state of two-level emitters and encompass: a Rydberg lattice, a dense lattice gas of atoms in low-lying electronic states, and atoms coupled to a nanophotonic waveguide as sketched in Fig. 5.4b - d. These three platforms all present long-range interactions, but the

different shape and strength of the couplings lead to differences in their effective range. E.g. in a Rydberg lattice system the nearest neighbor hopping parameters dominate the dynamics, while in the waveguide system all atoms are coupled to all other atoms with similar strength, such that excitation hopping stretches across all distances.

In all cases, we numerically simulate the dynamics of the Schrödinger equation with a time-dependent Hamiltonian of the form (5.10) for a system with open boundary conditions. Note that the cycle period T needs to be sufficiently long to ensure adiabaticity. This is fulfilled when $T \gg \hbar/\Delta E$, where ΔE is the minimum energy gap between neighboring bands during the cycle. Conversely, our transport protocols aim to minimize dispersion, requiring that the cycle is fast enough to prevent non-linearities in the Berry phase $\gamma(k)$ from introducing wave packet dispersion. Throughout this work, we have found cycle periods that approximately optimize these two conditions (we fix $T = 300/\Delta E$), although this still leads to a small degree of dispersion.

5.4.1 Short-range hopping: Rydberg atoms

The first system we consider is an ensemble of Rydberg atoms trapped in two lattices with lattice constant a and offset by a distance b with respect to each other as shown in Fig. 5.4b [81, 155]. Atoms excited to a Rydberg state are known for possessing exaggerated properties, such as long lifetimes and, most importantly, extremely large transition dipole moments between neighboring Rydberg states, which can lead to strong long-range dipole-dipole interactions [156, 157]. The dynamics of the system is determined by the Hamiltonian (5.6), where both ground and excited states of the two-level system are Rydberg states. The dipole-dipole interaction is here given generally by the expression

$$V_{ij} = \frac{d^2}{4\pi\epsilon_0\hbar} \frac{3\cos^2\theta_{ij} - 1}{r_{ij}^3}, \quad (5.19)$$

where $\mathbf{r}_{ij} = r_{ij}\hat{\mathbf{r}}_{ij}$ is the distance between the atoms, $\mathbf{d} = d\hat{\mathbf{d}}$ is the transition dipole moment, and $\cos\theta_{ij} = \hat{\mathbf{r}}_{ij} \cdot \hat{\mathbf{d}}$. To avoid breaking sublattice symmetry, we set the intra-sublattice parameters J_{2p} to zero by aligning the dipoles such that they form an angle $\theta_m = \arccos(1/\sqrt{3})$ with the unit separation vector between atoms of the same sublattice (see Fig. 5.4b) [81]. Moreover, the dipole-dipole interactions (excitation hopping parameters) between neighboring atoms (lattice

sites) dominate the dynamics, such that $\bar{J}' \approx J'_1$ and $\bar{J} \approx J_1$ with

$$J'_1 = \frac{d^2}{4\pi\epsilon_0\hbar} \frac{3\cos^2\theta'_1 - 1}{r'_1^3}, \quad (5.20)$$

$$J_1 = \frac{d^2}{4\pi\epsilon_0\hbar} \frac{3\cos^2\theta_1 - 1}{r_1^3}. \quad (5.21)$$

Here, $r'_1 = \sqrt{b^2 + h^2}$, $r_1 = \sqrt{(a-b)^2 + h^2}$, $\cos\theta'_1 = (b\cos\theta_m - h\sin\theta_m)/r'_1$ and $\cos\theta_1 = [(a-b)\cos\theta_m + h\sin\theta_m]/r_1$. Adding an on-site potential offset between the even and odd sites, the Hamiltonian is very close to the standard Rice-Mele model (3.15). Note, however, that this is only an approximation, and the actual long-ranged character of the interactions in the Rydberg system is fully taken into account in the following, in our numerical calculations.

Photon pumping on a Rydberg chain

While the qualitative results do not depend on the specific choice of parameters, as an illustrative example we consider a similar regime to the one realized in Ref. [81], i.e., rubidium atoms in the 60S (ground) and 60P (excited) states. The atoms form a chain such that the unit cells are separated by $a = 12 \mu\text{m}$ and the distance between the two sublattices is $h = 7.4 \mu\text{m}$ (chosen here to optimize the flatness of the time-integrated Berry curvature \mathcal{W}_k^-). The winding number of the Rydberg chain can then be changed from $v = 0$ to 1 and vice-versa by varying b , which in turn changes the values of \bar{J} and \bar{J}' . Specifically, as shown in Fig. 5.5a, in our case when $b \lesssim 0.16a$ the system is in a topologically trivial (dimerized) phase, while for $b \gtrsim 0.16a$ the system possesses topologically non-trivial properties such as the existence of edge states [81].

For the photon pumping to take place, we vary time dependently the relative position of the two lattices $b(t)$ (effectively sliding sublattice B keeping it parallel to sublattice A) and the energy offset $\Delta(t)$ as shown in Fig. 5.5b and c, respectively. Initially, the two sublattices are arranged such that $\delta\bar{J}(t=0) < 0$ and $\Delta(t=0) = \Delta_{\max} > 0$ and the photon is localized completely on sublattice B. Adiabatically varying Δ until it reaches the value $\Delta(t=T/2) = -\Delta_{\max}$ going past $\Delta(t=T/4) = 0$, where the Hamiltonian has winding number $v = 1$, will localize the photon on sublattice A. To surround the topological singularity we decrease $b(t)/a$ and $|\Delta|$ until we reach the point $(\Delta(t=3T/4) = 0, \delta\bar{J}(t=3T/4) > 0)$, where the Hamiltonian has winding number $v = 0$, before closing the loop.

We simulate the dynamics starting from a wave packet on the lower band, with a Gaussian quasi-momentum distribution $|f(k)|^2$ of width w_k . Here, we are able to find an optimized path in parameter space that leads to a particularly flat

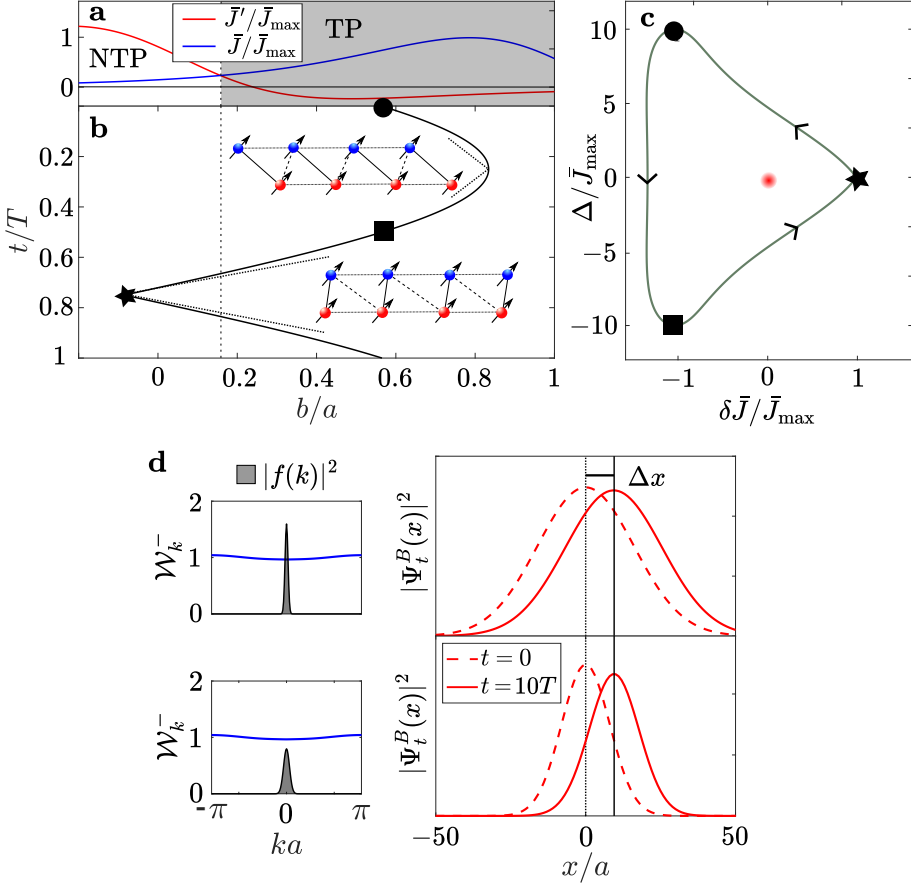


Figure 5.5: *Photon pumping on a Rydberg chain.* **a:** Dependence of the extended hopping parameters \bar{J}' and \bar{J} with the ratio b/a (all parameters are normalized to the maximal value $\bar{J}_{\max} \equiv |\max\{\bar{J}(t)\}|$ during the cycle). The gray shaded area represents $\delta\bar{J} < 0$, where the winding number of the extended SSH model is $\nu = 1$ (TP: topological phase). **b:** Variation of the intracell distance $b(t)$ during the pumping cycle. Importantly, twice during the cycle the extended hopping parameters coincide, such that $\delta\bar{J} = 0$. **c:** We vary the energy offset as $\Delta(t) = \Delta_{\max} \sin(2\pi t/T + \pi/2)$ such that the path in parameter space encircles the topological degeneracy point ensuring the displacement of the center of mass after a completed cycle. **d:** The left column shows the time-integrated Berry curvature of the lower band \mathcal{W}_k^- and quasi-momentum distribution density $|f(k)|^2$ (in arbitrary units). The right column shows the spatial probability density of the wave packet in real space (on the B sublattice), initially (dashed line) and after its numerical evolution for ten pumping cycles (solid line). The width of the Gaussian wave packet in momentum space, w_k , is doubled from the upper ($w_k a = 2\pi/100$) to the lower row ($w_k a = 2\pi/50$), leaving the displacement of the photon's center of mass $\Delta x = 10 \cdot 0.966a$ unchanged, but leading to an increase of the dispersion, such that the fidelity per cycle $\mathcal{F}(T) = 0.999$ and after ten cycles $\mathcal{F}(10T) = 0.988$ decreases to 0.997 and 0.964, respectively. Here, $T = 168/\bar{J}_{\max}$.

time-integrated Berry curvature across all the FBZ. As one can also see in Figure 5.5d, the cyclic pumping indeed leaves the shape of the photon mostly un-

changed except for its average position, which is displaced by an amount Δx . This displacement is in agreement with the one based on the time-integrated Berry curvature and the quasi-momentum distribution predicted by Equation (5.4). Notably, here we are able to achieve a fidelity per cycle well above 99.9%, which goes down as we increase the width of the wave packet in k -space and dispersion plays a more prominent role.

5.4.2 Long-range hopping: Atoms in free space

We now move to study a chain of atoms in low-lying electronic states coupled to the radiation field, such as the D-lines in alkaline atoms. Note that the main difference between this system and the Rydberg one lies on the scales: we consider here an optical dipole transition instead of a microwave one (hundreds of nm versus a few cm in wavelength). The atoms form again two chains (sublattices), but in this case they are placed on a single line as shown in Fig. 5.4c. The nearest neighbor distances are now smaller, but on the same order of magnitude as the transition wavelength λ_0 [158, 159]. As a consequence, as sketched in Fig. 5.4c, the dipole-dipole interaction is given generally by the expression

$$V_{ij} = \frac{3\gamma}{4} \left[y_0(k_a r_{ij}) - \frac{y_1(k_a r_{ij})}{k_a r_{ij}} + y_2(k_a r_{ij})(\hat{\mathbf{d}} \cdot \hat{\mathbf{r}}_{ij})^2 \right], \quad (5.22)$$

where y_n are spherical Bessel functions of the second kind, $\gamma = \frac{d^2 k_0^3}{3\pi\epsilon_0\hbar}$ is the single atom spontaneous decay rate, and $k_0 = \omega_a/c = 2\pi/\lambda_0$ is the wave number of the transition, respectively [160]. This interaction can no longer be realistically approximated to be nearest neighbor only, as it was the case in the Rydberg system. Thus, the corresponding extended Rice-Mele model (5.10) contains all hopping parameters J'_{2p-1} , J_{2p-1} and J_{2p} . While the sublattice symmetry is in general broken in this system, we minimize this effect by choosing the distance a between neighboring atoms of the same sublattice at a value $a(\theta_d)$, where θ_d is the angle between the atomic dipoles and the chain, i.e. $\cos \theta_d = \hat{\mathbf{r}}_{ij} \cdot \hat{\mathbf{d}}$, such that $J_2 = 0$ (see Fig. 5.4c for the $\theta_d = \pi/2$ case). Given that the hopping parameters slowly decrease with the distance between atoms, the values of the subsequent symmetry-breaking hopping parameters J_4 , J_6 , are almost negligible, and the sublattice symmetry is only slightly broken.

Photon pumping on a two-level atom chain

Again for illustration, here we choose a lattice constant $a = 0.7\lambda_0$ and the dipole moments oriented perpendicularly to the chain with $\theta_d = \pi/2$, which

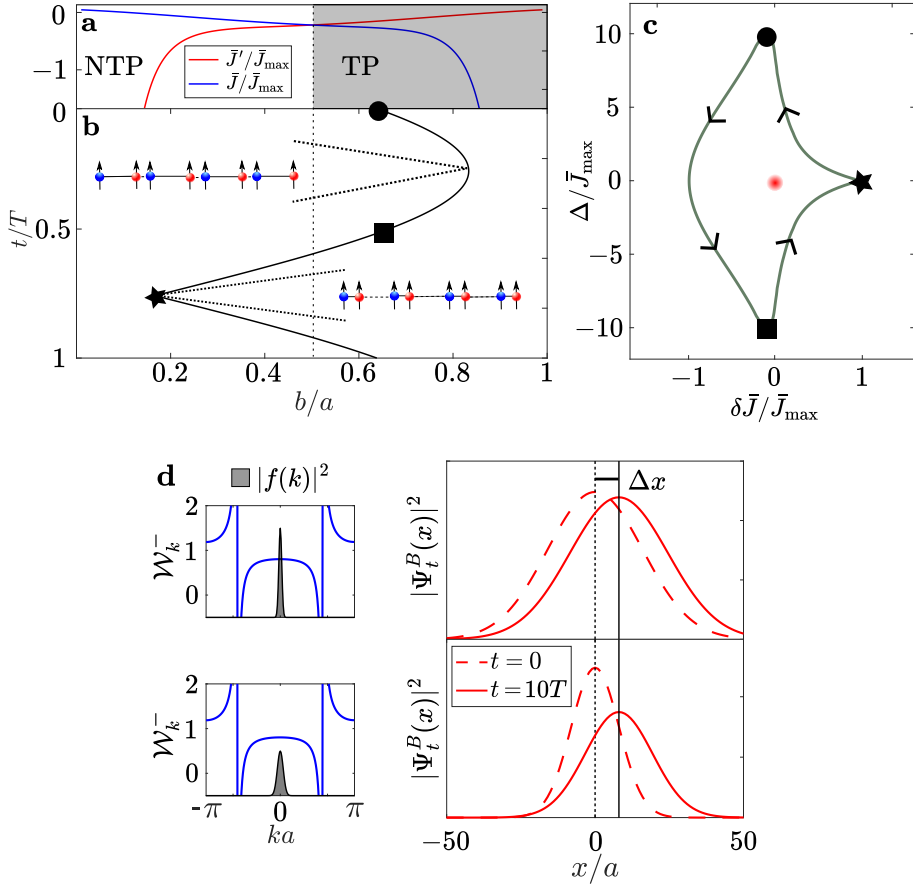


Figure 5.6: *Photon pumping on a two-level atom chain.* **a:** Dependence of the extended hopping parameters \bar{J}' and \bar{J} with the ratio b/a (normalized to $\bar{J}_{\max} \equiv |\max\{\bar{J}(t)\}|$ during the cycle). The gray shaded area represents $\delta\bar{J} < 0$, where the winding number of the extended SSH model is $v = 1$ (TP: topological phase). **b:** Variation of the intracell distance $b(t)$ during the pumping cycle. **c:** We vary the energy offset as $\Delta(t) = \Delta_{\max} \sin(2\pi t/T + \pi/2)$ such that the path in parameter space encircles the topological degeneracy point ensuring the displacement of the center of mass after a completed cycle. **d:** The left column shows the time-integrated Berry curvature of the lower band \mathcal{W}_k^- and quasi-momentum distribution density $|f(k)|^2$ (in arbitrary units). The right column shows the spatial probability density of the wave packet in real space (on the B sublattice), initially (dashed line) and after its numerical evolution for ten pumping cycles (solid line). The width of the Gaussian wave packet in momentum space w_k (the same as in Fig. 5.5) is doubled from the upper to the lower row, leaving the displacement of the photon's center of mass $\Delta x = 10 \cdot 0.803a$ unchanged, but leading to an increase of the dispersion, such that the fidelity per cycle $\mathcal{F}(T) = 0.999$ and after ten cycles $\mathcal{F}(10T) = 0.986$ decreases to 0.986 and 0.890, respectively. Here, $T = 190/\bar{J}_{\max}$.

leads to a negligible intra sub-lattice hopping $J_2 = 0$. As was shown in [71], the winding number of the extended SSH model, which is reproduced by the system when the on-site potential $\Delta = 0$, again changes with the ratio b/a (see Fig. 5.6a). Hence, the photon pumping is realized again by sliding the atoms trapped in the

sublattice B with respect to sublattice A, i.e., making $b(t)$ time-dependent (see Fig. 5.6b).

The pumping cycle shown in Fig. 5.6c is very similar to the one used for the Rydberg chain, designed to encircle the topological degeneracy point and to maximize the region in k space where \mathcal{W}_k^- can be considered constant. As shown in Fig. 5.6d, the long-ranged character of the couplings introduces two discontinuities in \mathcal{W}_k^- at the so-called light lines [32, 55], which are located at $k_d a = \pm 2\pi \left(1 - \frac{a}{\lambda_0}\right)$. This sets a hard constraint for the width of $|f(k)|^2$ that allows for a dispersionless topological pumping, namely $w_k \ll 2k_d$. As shown Fig. 5.6d, however, dispersionless pumping can be still realized, with a fidelity per cycle as high as 99.9%.

5.4.3 All-to-all hopping: Waveguide system

Finally, we discuss a chain of emitters coupled to a waveguide. This setup can be realized, for instance, with cold atoms trapped in the vicinity of a tapered optical fiber [161–163]. In this system, the coherent interactions between atoms are mediated by the fundamental guided modes of the waveguide. Note, that we limit the discussion in this work, to cases where the coupling efficiency of the emitters to the guided modes is almost 100%, as it can be achieved, for example, with artificial atoms in semiconductors (quantum dots) [164, 165]. In general, however, one needs to consider the coupling through the radiation or unguided modes. In the case of atoms placed around a cylindrical nanofiber (see Fig. 5.4d), the interactions between atoms separated by an angle $\phi_{ij} = \phi_j - \phi_i$ and a distance $z_{ij} = z_j - z_i$, as derived in Chapter 5, are given by

$$V_{ij} = i \frac{\omega_a \beta'}{4\hbar\epsilon_0} \sum_{fl} \mathbf{d}_i^* \cdot \mathbf{e}^{(\beta lf)}(r_i) \mathbf{d}_j \cdot \mathbf{e}^{(\beta lf)*}(r_j) \text{sgn}(f z_{ij}) e^{il\phi_{ij}} e^{if\beta z_{ij}}, \quad (5.23)$$

where $\mathbf{e}^{(\beta lf)}(r) = (e_r, -le_\phi, fe_z)$ is the profile function of the fundamental guided mode with propagation constant β , polarization l and propagation direction f at a distance r from the waveguide core, $\mathbf{d}_i = (d_i^r, d_i^\phi, d_i^z)$ is the transition dipole moment of atom i and $\beta' = \frac{d}{d\omega}\beta$. For simplicity, we consider the dipole moments of all emitters to point in the radial direction, and all of the atoms at the same radial distance from the waveguide core. In this case, the dipole-dipole interaction is given by the simple expression

$$V_{ij} = \frac{\gamma}{2} \cos(\phi_{ij}) \sin(\beta z_{ij}), \quad (5.24)$$

where $\gamma = \frac{2|d|^2\omega_a\beta'}{\hbar\epsilon_0}|e_r|^2$ is the rate of a photon to be emitted into the waveguide for a single atom. Moreover, we consider in particular the situation where the atomic cells are positioned as a helix around the waveguide as shown in Fig. 5.4d [166]. The hopping parameters in this case are given by

$$\begin{aligned} J_{2p} &= \frac{\gamma}{2} \sin(\beta ap) \cos(p\phi_1), \\ J_{2p-1} &= \frac{\gamma}{2} \sin[\beta(pa - b)] \cos(p\phi_1 - \phi'_1), \\ J'_{2p-1} &= \frac{\gamma}{2} \sin[\beta((p-1)a + b)] \cos[(p-1)\phi_1 + \phi'_1] \end{aligned} \quad (5.25)$$

where ϕ_1 and ϕ'_1 are the angle between atoms in neighboring cells of the same sublattice, and between atoms of different sublattices within the same cell, respectively. In order to ensure that the chiral symmetry is not broken, we fix the value of a to $a = \pi/\beta$. We also fix the values of $b = a/2 = \pi/(2\beta)$ and $\phi_1 = \pi/2$, such that $J_{2p} = 0$ and the remaining hopping parameters read

$$\begin{aligned} J_{2p-1} &= -\frac{\gamma}{2}(-1)^p \cos\left(\phi'_1 - \frac{p\pi}{2}\right), \\ J'_{2p-1} &= -\frac{\gamma}{2}(-1)^p \sin\left(\phi'_1 + \frac{p\pi}{2}\right), \end{aligned} \quad (5.26)$$

having lost all dependence on the distance between the atoms in the longitudinal direction, thus being exclusively dependent on the angular offset between sublattices ϕ'_1 .

Photon pumping on a waveguide system

As shown in Fig. 5.7a, the transition from a topological to a non-topological phase occurs in this system when the angle $\phi'_1 = \pi/4$, since at this point $J_{2p-1} = J'_{2p-1}$ for all values of p . A pumping scheme can then be established by adiabatically rotating sublattice B by an angle $\phi'_1(t)$, which after a time T returns to the initial configuration (Figs. 5.7b and c). As it was discussed for atoms in free space (sec Sec. 5.4.2), due to the long-ranged character of the couplings the time-integrated Berry curvature \mathcal{W}_k^- shows a discontinuity at the light lines at $k_da = \pm\pi/2$ (see Fig. 5.7d). This again constrains the width of the Gaussian wave packet in momentum space, which must satisfy $w_k \ll \pi/a$ in order to achieve dispersionless pumping. Here, the role of the flatness of \mathcal{W}_k^- is made particularly clear: since the light lines are closer to $k = 0$ than in the case of low-lying two-level systems, the curvature of \mathcal{W}_k^- within the region of the Gaussian wave packet is larger, which in turn reduces the fidelity of the pumping process. Finally, we note that in the waveguide case the pumping occurs in the opposite

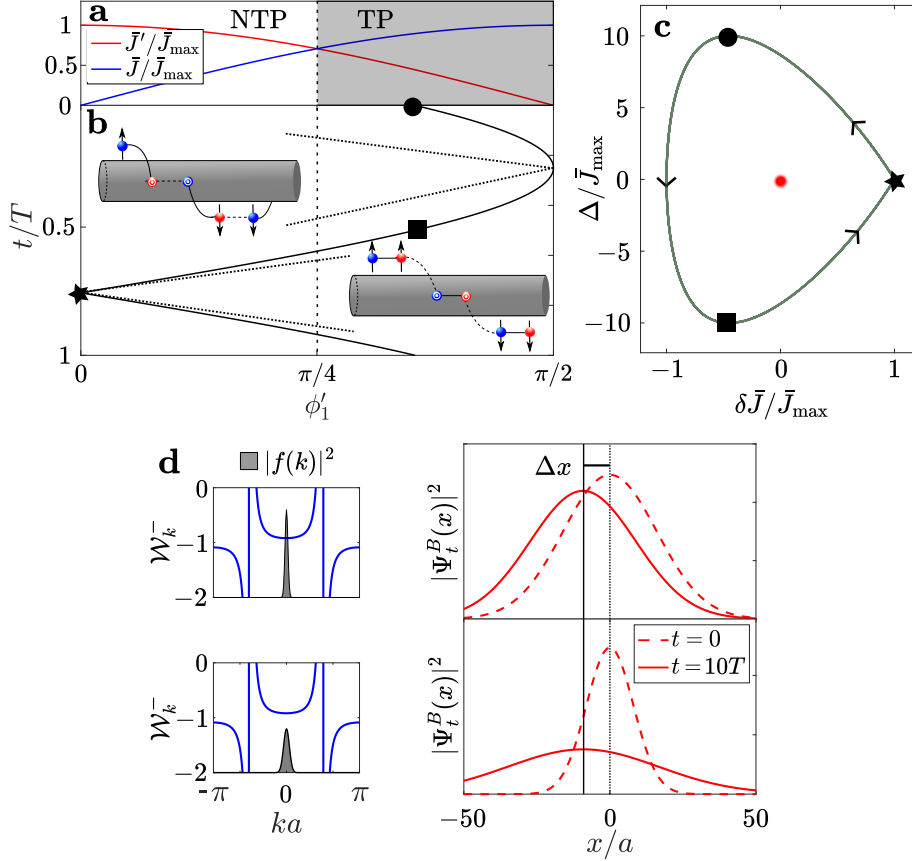


Figure 5.7: *Photon pumping on a waveguide system.* **a:** Dependence of the extended hopping parameters \bar{J}' and \bar{J} with the angle ϕ'_1 (all parameters are normalized to the maximal value $\bar{J}_{\max} \equiv |\max\{\bar{J}(t)\}|$ during the cycle). The gray shaded area represents $\delta\bar{J} < 0$, where the winding number of the extended SSH model is $\nu = 1$ (TP: topological phase). **b:** Variation of the angle $\phi'_1(t)$ during the pumping cycle. Importantly, twice during the cycle the extended hopping parameters coincide, such that $\delta\bar{J} = 0$. **c:** We vary the energy offset as $\Delta(t) = \Delta_{\max} \sin(2\pi t/T + \pi/2)$ such that the path in parameter space encircles the topological degeneracy point ensuring the displacement of the center of mass after a completed cycle. **d:** The left column shows the time-integrated Berry curvature of the lower band \mathcal{W}_k^- and quasi-momentum distribution density $|f(k)|^2$ (in arbitrary units). The right column shows the spatial probability density of the wave packet in real space (on the B sublattice), initially (dashed line) and after its numerical evolution for ten pumping cycles (solid line). The width of the Gaussian wave packet in momentum space w_k (the same as in Figs. 5.5 and 5.6) is doubled from the upper to the lower row, leaving the displacement of the photon's center of mass $\Delta x = 10 \cdot 0.919a$ unchanged, but leading to an increase of the dispersion, such that the fidelity per cycle $\mathcal{F}(T) = 0.998$ and after ten cycles $\mathcal{F}(10T) = 0.962$ decreases to 0.987 and 0.540, respectively. Here, $T = 150/\bar{J}_{\max}$.

direction compared with the two previous cases studied. This is due to the sign of \mathcal{W}_k^- , which is negative around $k = 0$, while the Chern number of the band, i.e., the integral of \mathcal{W}_k^- over the full FBZ, is the same as in all systems, namely $C_- = +1$. Note, that in principle the direction of pumping is arbitrary and de-

pends on the orientation of the path around the singularity, i.e. the excitation moves in opposite direction by reversing the path shown in Fig. 5.5-5.7c.

5.5 Robustness against dissipation and disorder

Up until now, we have shown that the topological pumping of a photon in a system with long-range couplings is possible. However, these quantum optical systems also suffer from dissipation, e.g. radiative decay of the photon into the environment, as introduced in equation (5.5). Moreover, experimental systems have a degree of disorder due to, for example, imperfect trapping of the atoms, which leads to disorder in the hopping parameters. In this section, we will analyze the effect of these two potentially detrimental sources on the topological photon pumping protocols.

5.5.1 Dissipation

Dissipation has a different character for the three platforms we have studied here. In all three, however, one can encode it in a general form as the action of the dissipator

$$\mathcal{D}(\hat{\rho}) = \sum_{k=1}^N \Gamma_k \left[\hat{J}_k \hat{\rho} \hat{J}_k^\dagger - \frac{1}{2} \left\{ \hat{J}_k^\dagger \hat{J}_k, \hat{\rho} \right\} \right], \quad (5.27)$$

where \hat{J}_k is a so called jump operator and Γ_k is the rate at which this jump occurs. Here, the *jumps* are emissions of a photon into the environment.

For the chain of Rydberg atoms, the main emission channel is the independent decay with the same rate, i.e. $\Gamma_k = \Gamma$, from the Rydberg states into the atomic ground state [167]. As an illustration, the comparison between the lifetime of the 60P rubidium Rydberg state, $\tau_R \approx 500 \mu\text{s}$, and an optimal pumping period of $T \approx 22 \mu\text{s}$ means that the pumping process is likely to survive dissipation at least for a few cycles. However, to overcome this constraint one can think of, for example, leveraging the remarkable lifetimes afforded by circular Rydberg states [168], which exhibit exceptional decoupling from optical dipole transitions.

In the second case we considered, i.e., atoms in low-lying energy states, the nearest neighbor distances are comparable to λ_0 and the dissipation acquires a collective character. Here, the dissipator reads

$$\mathcal{D}(\hat{\rho}) = \sum_{i,j=1}^N \Gamma_{ij} \left[\hat{\sigma}_i \hat{\rho} \hat{\sigma}_j^\dagger - \frac{1}{2} \left\{ \hat{\sigma}_i^\dagger \hat{\sigma}_j, \hat{\rho} \right\} \right], \quad (5.28)$$

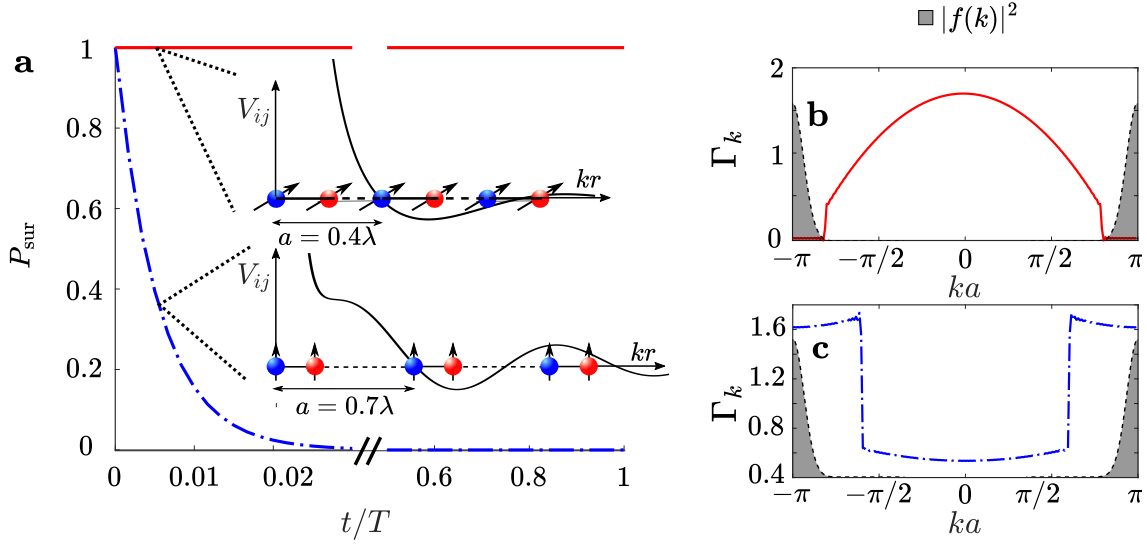


Figure 5.8: *Collective dissipation.* **a:** Survival probability for the photon as a function of time during the pumping cycle for a chain with $a/\lambda_0 = 0.4$ (red solid line) and $a/\lambda_0 = 0.7$ (blue dash-dotted line). **b:** For $a/\lambda_0 = 0.4$, $|f(k)|^2$ is nonzero only in a region of the FBZ where $\Gamma_k = 0$, leading to a survival probability $P_{\text{sur}}(t) = 1$ for the full cycle. **c:** The same wave packet for $a/\lambda_0 = 0.7$ has a large decay rate, apparent from the quick decay of the survival probability. Note, that in both cases we choose an angle θ_d such that, as discussed previously, $J_2 = 0$ and the sublattice symmetry is approximately conserved.

where the Γ_{ij} is, in general, not diagonal and reads

$$\Gamma_{ij} = \frac{3\gamma}{2} \left[j_0(k_a r_{ij}) - \frac{j_1(k_a r_{ij})}{k_a r_{ij}} + j_2(k_a r_{ij})(\hat{\mathbf{d}} \cdot \hat{\mathbf{r}}_{ij})^2 \right], \quad (5.29)$$

where j_n are spherical Bessel functions of the first kind. As in the case of the dipole-dipole interactions (5.22), Γ_{ij} depends strongly on the ratio between the interatomic distance and the transition wavelength, the precise external geometry of the system and the orientation of the transition dipole moments [160]. The (collective) jump operators and rates can be found by diagonalizing this matrix, such that $\Gamma_k = \sum_{ij} M_{ki} \Gamma_{ij} M_{jk}^*$ and $\hat{J}_k = \sum_j M_{kj} \hat{\sigma}_j$. Here one can see that the jump operators are then in general, superpositions of all single atom spin operators $\hat{\sigma}_j = |g\rangle\langle e|$, with rates that can be larger (superradiant) or smaller (subradiant) than the single atom decay rate. In the regime we consider here, a small number of superradiant states with $N\gamma > \Gamma_k$ are present. The region of the FBZ where these superradiant states appear, however, depends strongly on the specific value of the ratio between nearest neighbor distance and λ_0 . In particular, due to the large sublattice energy shifts Δ that are present for most of the pumping cycle,

the two sublattices are effectively decoupled dynamically, which means that the reduced distance that determines the dissipation properties is a/λ_0 . As can be observed in Figs. 5.8b and c, the superradiant rates can be found at the center and the border of the FBZ for $a/\lambda_0 < 1/2$ and $a/\lambda_0 > 1/2$, respectively. This in turn means that, as shown in Fig. 5.8b, choosing a value $a/\lambda_0 < 1/2$, one can create a wave packet centered at $k = \pm\pi/a$ with support exclusively in the subradiant region, which in turn leads to a survival probability of the photon P_{sur} equal to one for all experimentally relevant times. For comparison, the same wave packet created on a chain where $a/\lambda_0 > 1/2$ will decay fast (in the example we show in Fig. 5.8a with $a/\lambda_0 = 0.7$, $\Gamma_{\text{eff}} = 1.6183\gamma$).

Finally, in the case of an ensemble of atoms coupled to a waveguide, the dissipation is described by the same dissipator (5.28), where now the dissipation coefficient matrix, as derived in Chapter 5, is given by

$$\Gamma_{ij} = \frac{\omega_a \beta'}{2\hbar\epsilon_0} \sum_{fl} \mathbf{d}_i^* \cdot \mathbf{e}^{(\beta lf)}(r_i) \mathbf{d}_j \cdot \mathbf{e}^{(\beta lf)*}(r_j) e^{il\phi_{ij}} e^{if\beta z_{ij}}. \quad (5.30)$$

In the parameter regime we have considered in the previous section, this expression reduces to

$$\Gamma_{ij} = \gamma \cos(\phi_{ij}) \cos(\beta z_{ij}). \quad (5.31)$$

The diagonalization of this matrix shows that only two collective decay channels possess non-zero decay rates. Since the Gaussian wave packet that constitutes our initial state has no overlap with these two superradiant states, dissipation in this case has virtually no effect on the topological pumping process. Note, that again we have assumed that the dissipation only occurs into the guided modes on the waveguide, neglecting the effect of unguided modes.

5.5.2 Disorder

Finally, we analyze the robustness against disorder of the topological pumping realized on the three quantum optical platforms considered. In particular, we consider the unavoidable disorder on the positions of the atoms by adding random Gaussian noise to each atom position with standard deviation $\sigma(\mathbf{r})$ around the equilibrium position \mathbf{r} . The corresponding standard deviation of the distribution of distances between any two emitters in the chain $r_{ij} = |\mathbf{r}_j - \mathbf{r}_i|$ is then given by

$$\sigma(r_{ij}) = \sqrt{2} \frac{\mathbf{r}_{ij} \cdot \sigma(\mathbf{r})}{r_{ij}}.$$

Such a Gaussian disorder in the distance r_{ij} translates into a disorder in the hopping parameters $J(r_{ij}, t)$ as

$$\sigma[J(r_{ij}, t)] = \frac{\partial J(r_{ij}, t)}{\partial r_{ij}} \sigma(r_{ij}).$$

Due to the form of the extended hopping parameters \bar{J}' and \bar{J} , the disorder propagates when considering the full path in parameter space. Using the theory of error propagation we derive the disorder in the extended hopping parameter difference $\delta\bar{J}$, which is given by

$$\sigma[\delta\bar{J}] = \sqrt{\sigma[\mathbf{J}] \cdot \sigma[\mathbf{J}] + \frac{1}{2} \sum_{p \neq q}^{2[N/4]} K_{pq}(t)},$$

where we have introduced the extended hopping vector \mathbf{J} with odd components $\mathbf{J}_{2p-1} = (-1)^{(p+1)} J'_{2p-1}$ and even components $\mathbf{J}_{2p} = (-1)^p J_{2p-1}$ and the covariance matrix $K = \sigma[\mathbf{J}^T] \sigma[\mathbf{J}]$.

Considering that the disorder varies along the path, we introduce the time-integrated function

$$\delta\mathcal{J} \equiv \int_0^T dt \delta\bar{J}(t), \quad (5.32)$$

and its standard deviation

$$\sigma(\delta\mathcal{J}) \equiv \sqrt{\int_0^T dt \sigma[\delta\bar{J}(t)]}, \quad (5.33)$$

as a common measure of disorder for the three systems. Hence, in order to get a fair comparison, we choose the same value of the time-integrated disorder $\sigma(\delta\mathcal{J})/\delta\mathcal{J}$ for all systems. Note, however, that as a result of propagation of disorder the Rydberg system with short-range couplings requires a larger disorder in the position compared to the two other systems to reach an equivalent disorder in the path.

To measure the effect of disorder, we calculate the fidelity

$$\mathcal{F}_\sigma(T) = \left(\text{Tr} \sqrt{\sqrt{\rho_T^0} \rho_T^\sigma \sqrt{\rho_T^0}} \right)^2,$$

where ρ_T^σ is the disordered state averaged over a number of realizations of random Gaussian disorder in the emitter positions and $\rho_T^0 = |\Psi_T^0\rangle\langle\Psi_T^0|$ is the non-disordered state after one cycle. Figure 5.9 shows this fidelity for the three different systems as a function of the time-integrated disorder $\sigma(\delta\mathcal{J})/\delta\mathcal{J}$ up to 10%.

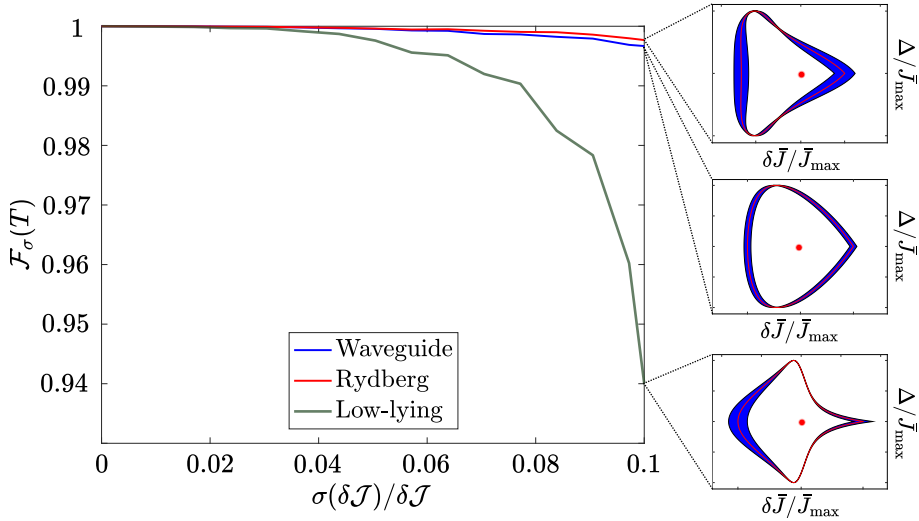


Figure 5.9: *Robustness against disorder.* Fidelity after one pumping cycle $\mathcal{F}_\sigma(T)$ between the disordered and non-disordered states as a function of the time-integrated disorder in the extended hopping parameters $\sigma(\delta\mathcal{J})/\delta\mathcal{J}$. The insets show the disordered paths in parameter space for the three systems with a time-integrated disorder of 10%. The unperturbed path in parameter space is shown by the red line, while the blue shaded area shows the propagated disorder given a Gaussian disorder in each emitter position in the chain.

We can observe that the pumping is indeed very robust in all three cases, with the atoms in low-lying states being the most affected, likely due to the slight breaking of the sublattice symmetry present in this case, i.e. the presence of $J_{2p} \neq 0$ terms, which effectively double the amount of couplings affected by the disorder.

5.6 Conclusions and outlook

This study establishes for the first time a framework for topological photon pumping in quantum optical systems with long-range couplings. This framework allows for the controlled and robust transport of photonic excitations over a one-dimensional emitter chain. Notably, the atoms are only displaced over short distances within a single unit cell, while the excitation is transported with high fidelity over many lattice sites. We discuss its realization in different experimental platforms, such as Rydberg atoms, in a dense atomic lattice gas, and atoms coupled to waveguides. For each system we establish a counter-intuitive protocol that displaces only half of the atoms, but allows to transport the photonic excitation with a fidelity reaching 99.9%. Our results underscore that this scheme not only shifts the center-of-mass of the excitation, but also maintains the shape of the wave packet (dispersionless) and we show that it is robust against both local disorder and dissipation.

While in our work we found a parameter trajectory that is suitable for realizing pumping, we did not use any optimization procedure to obtain an optimal path. Depending on the context, such strategies could be employed to optimize the displacement Δx per cycle, or the speed of the pumping, while maintaining adiabaticity, e.g. faster when gap is large and slower when gap is narrow. Moreover, the parameters of the system could be optimized to realize flatter time-integrated Berry curvatures, which in turn minimize the dispersion.

While our results are obtained in 1D systems, these concepts can be generalized to higher dimensional systems [169]. Finally, such charge pump could be extended to intriguing *spin* pumping schemes that include different light polarizations corresponding to coupling to different transitions. This could mimic a Fu-Kane pump [170], which in condensed matter systems allow for a spin transport without charge transport.

Chapter 6

Topological phases in a 2D Rydberg lattice

6.1 Introduction

Recently, the extension of the well known SSH model to a 2D lattice has been extensively studied [9, 171–174]. Due to the many variants of the model, including different types of couplings giving rise to specific symmetries, the 2D SSH model allows for the study of both rich gapless topological physics, including the observation of Dirac cones [175], semi-metallic phases [176–178], and gapped topological phases with robust edge and/or corner states [179–182]. Due to the coexistence of time-reversal and inversion symmetries in some of variants of the 2D SSH model, the Berry curvature vanishes throughout the 2D FBZ, resulting in a zero Chern number. Surprisingly, contrary to Chern insulators, non-trivial topological phases can be found attributed to another topological invariant, the 2D Zak phase, which arises from a non-zero Berry connection [183–185].

In this work we aim to realize a specific version of the 2D SSH model consisting of Rydberg atoms with exchange dipole-dipole interactions. First we analyze the bulk properties of the model and identify a phase diagram with two tunable parameters. We find a semi-metallic phase characterized by a pair of oppositely topologically charged and tunable Dirac points and associated tilted anisotropic cones, which for specific parameters collapse into nodal lines. Furthermore, we identify and characterize three distinct gapped topological phases with non-zero 2D Zak phase. Two are weak topological insulating phases with one non-zero component of the 2D Zak phase manifested by edge states on the corresponding borders. The final gapped topological phase is a weakly broken higher order topological insulating phase. Here, we find corner-like states for specific parameter choices.

6.2 The 2D SSH model with Rydberg atoms: Bulk properties

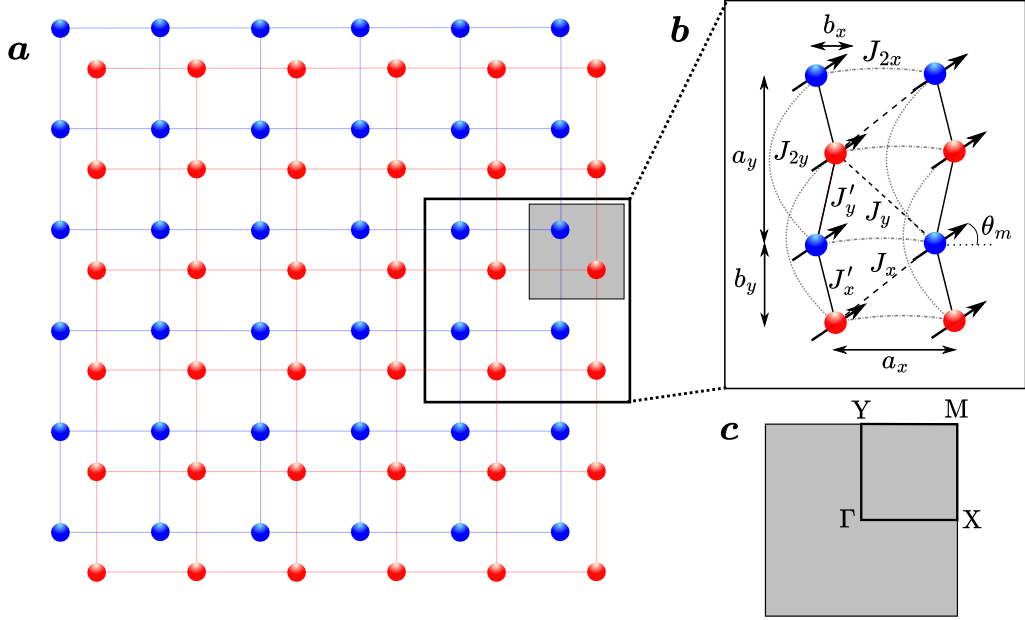


Figure 6.1: *The 2D SSH model with Rydberg atoms.* **a:** The 2D SSH model consisting of two sublattices A and B denoted by blue and red dots. **b:** The sublattices have an internal spacing given by a_x and a_y in the x and y -direction respectively. Sublattice B is offset with respect to sublattice A by b_x and b_y in the x and y -direction respectively. Each lattice site contains a Rydberg atom with dipole orientation indicated by the black arrows. The dipoles are tilted with an angle θ_m with respect to the x -axis. Hopping can occur between each site on one sublattice to the four nearest neighbors of the other sublattice with hopping parameters J'_x , J_x , J'_y and J_y . Hopping can also occur within the same sublattice to the nearest neighbour with hopping parameter in the x -direction J_{2x} and in the y -direction J_{2y} . **c:** The first Brillouin zone of the 2D SSH model and the high symmetry points Γ , X , Y and M .

We consider a 2D lattice consisting of two offset rectangular sublattices. The lattice can be regarded as M vertically stacked SSH chains with N sites in each chain. Each SSH chain is a bipartite lattice consisting of two-site unit cells hosting one site of sublattice A and one site of sublattice B depicted in Figure 6.1a by red and blue dots respectively. Both sublattices have a lattice constant a_x and a_y in the x and y -direction respectively. Furthermore, sublattice B is offset with respect to sublattice A by a distance b_x and b_y in the x and y -direction respectively. The 2D lattice can equivalently be considered as $N/2$ vertical SSH chains with $2M$ sites stacked from left to right.

Each site is populated by a Rydberg atom, which we will model as identical two-level systems where both the ground and excited state are Rydberg states

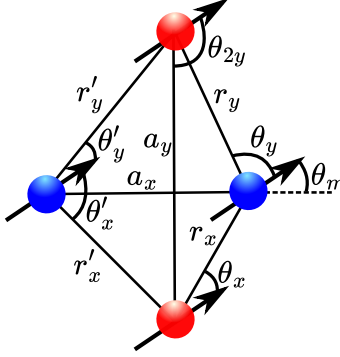


Figure 6.2: *Geometry of the Rydberg lattice.* The distances and angles between the Rydberg atoms in the lattice.

denoted by $|r\rangle$ and $|e\rangle$ respectively. Each Rydberg atom has a dipole transition moment aligned along the angle θ_m with respect to the x -axis illustrated by the arrows in Figure 6.1b. Within each SSH chain, a Rydberg excitation can hop within its cell with a rate J'_x and between neighbouring cells with a rate J_x . Moreover, hopping can occur between neighbouring chains with rates J'_y and J_y . Finally, we will consider a weak intrasublattice hopping in the x and y -direction given by the rates J_{2x} and J_{2y} respectively. The Hamiltonian of the system is given by

$$\hat{H} = \hbar \left\{ \sum_{n=1}^{N/2} \sum_{m=1}^{M/2} J'_x \hat{a}_{nm}^\dagger \hat{b}_{nm} + \sum_{n=1}^{N/2-1} \sum_{m=1}^{M/2} J_x \hat{b}_{nm}^\dagger \hat{a}_{n+1m} \right. \\ + \sum_{n=1}^{N/2} \sum_{m=1}^{M/2-1} J'_y \hat{a}_{nm}^\dagger \hat{b}_{nm+1} + \sum_{n=1}^{N/2-1} \sum_{m=1}^{M/2-1} J_y \hat{b}_{nm+1}^\dagger \hat{a}_{n+1m} \\ + \sum_{n=1}^{N/2-1} \sum_{m=1}^{M/2} J_{2x} (\hat{a}_{nm}^\dagger \hat{a}_{n+1m} + \hat{b}_{nm}^\dagger \hat{b}_{n+1m}) \\ \left. + \sum_{n=1}^{N/2} \sum_{m=1}^{M/2-1} J_{2y} (\hat{a}_{nm}^\dagger \hat{a}_{nm+1} + \hat{b}_{nm}^\dagger \hat{b}_{nm+1}) + \text{h.c.} \right\}, \quad (6.1)$$

where $\hat{a}_{nm}^{(\dagger)}$ is the annihilation (creation) operator for sublattice A at cell (n, m) and $\hat{b}_{nm}^{(\dagger)}$ is the annihilation (creation) operator for sublattice B at cell (n, m) . The hopping parameters are given by the Rydberg dipole-dipole interactions

$$J'_x = \frac{d^2}{4\pi\epsilon_0\hbar} \frac{3\cos^2\theta'_x - 1}{r'_x^3}, \quad J_x = \frac{d^2}{4\pi\epsilon_0\hbar} \frac{3\cos^2\theta_x - 1}{r_x^3}, \\ J'_y = \frac{d^2}{4\pi\epsilon_0\hbar} \frac{3\cos^2\theta'_y - 1}{r'_y^3}, \quad J_y = \frac{d^2}{4\pi\epsilon_0\hbar} \frac{3\cos^2\theta_y - 1}{r_y^3}, \\ J_{2x} = \frac{d^2}{4\pi\epsilon_0\hbar} \frac{3\cos^2\theta_m - 1}{a_x^3} \quad J_{2y} = \frac{d^2}{4\pi\epsilon_0\hbar} \frac{3\cos^2\theta'_{2y} - 1}{a_y^3}. \quad (6.2)$$

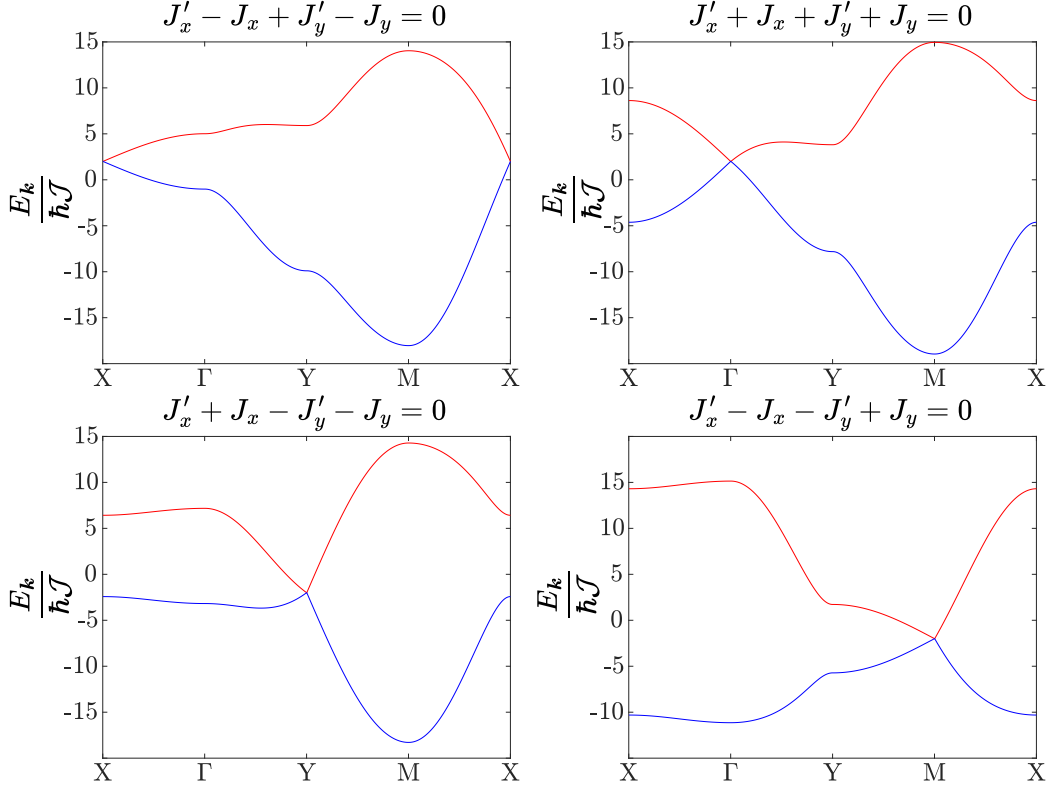


Figure 6.3: *Bulk spectra*. The bulk energy gap closes at the high symmetry points (X, Γ , Y and M) in the FBZ for different values of the hopping parameters given above and for $\theta_m = \arccos(1/\sqrt{3})$ and $a_x = a_y = a$. The bulk energy is normalized by the factor $\hbar\mathcal{J} = \frac{d^2}{4\pi\epsilon_0 a^3}$.

Here $r'_x = \sqrt{b_x^2 + b_y^2}$, $r_x = \sqrt{(a_x - b_x)^2 + b_y^2}$, $r'_y = \sqrt{b_x^2 + (a_y - b_y)^2}$ and $r_y = \sqrt{(a_x - b_x)^2 + (a_y - b_y)^2}$. The angles are given by

$$\begin{aligned} \cos \theta'_x &= (b_x \cos \theta_m - b_y \sin \theta_m) / r'_x, \\ \cos \theta_x &= ((a_x - b_x) \cos \theta_m + b_y \sin \theta_m) / r_x, \\ \cos \theta'_y &= (b_x \cos \theta_m + (a_y - b_y) \sin \theta_m) / r'_y, \\ \cos \theta_y &= ((a_x - b_x) \cos \theta_m - (a_x - b_y) \sin \theta_m) / r_y, \\ \cos \theta_{2y} &= \cos(\pi/2 - \theta_m). \end{aligned} \quad (6.3)$$

The different distances and angles between the Rydberg atoms in the lattice are shown in Figure 6.2.

Considering periodic boundary conditions, the Hamiltonian (6.1) may be written in terms of its irreducible matrix form in momentum space $\hat{h}(\mathbf{k})$ as

$$\hat{H} = \sum_{\substack{\mathbf{k} \in 2D \text{ FBZ} \\ \alpha, \beta \in A, B}} \hat{c}_\alpha^\dagger(\mathbf{k}) \hat{h}_{\alpha\beta}(\mathbf{k}) \hat{c}_\beta(\mathbf{k}), \quad (6.4)$$

where $\hat{c}_\alpha(\mathbf{k}) = \hat{a}_k$ for $\alpha = A$ and $\hat{c}_\alpha(\mathbf{k}) = \hat{b}_k$ for $\alpha = B$, where \hat{a}_k (\hat{a}_k^\dagger) and \hat{b}_k (\hat{b}_k^\dagger) are the Fourier transformed annihilation (creation) operators on sublattice A and B, respectively. The bulk momentum space Hamiltonian is given by

$$\hat{h}(\mathbf{k}) = \begin{pmatrix} n_0(\mathbf{k}) & n(\mathbf{k}) \\ n^*(\mathbf{k}) & n_0(\mathbf{k}) \end{pmatrix}. \quad (6.5)$$

The functions that define the topological properties are

$$n(\mathbf{k}) = \hbar(J'_x + J'_y e^{ik_y a_y} + J_x e^{-ik_x a_x} + J_y e^{-i(k_x a_x - k_y a_y)}), \quad (6.6)$$

and

$$n_0(\mathbf{k}) = \hbar(2J_{2x} \cos(k_x a_x) + 2J_{2y} \cos(k_y a_y)). \quad (6.7)$$

The two energy bands of the bulk momentum space Hamiltonian are given by $E_k^\pm = n_0(\mathbf{k}) \pm |n(\mathbf{k})|$.

The form of the bulk momentum space Hamiltonian (6.5) exhibits time-reversal symmetry $\hat{T}\hat{h}(\mathbf{k})\hat{T}^{-1} = \hat{h}(-\mathbf{k})$ and inversion symmetry $\hat{\mathcal{I}}\hat{h}(\mathbf{k})\hat{\mathcal{I}}^{-1} = \hat{h}(-\mathbf{k})$ however the chiral and particle-hole symmetry are broken due to the diagonal $n_0(\mathbf{k})$ -term. Due to the coexistence of both time-reversal and inversion symmetry, the Berry curvature is zero throughout the 2D FBZ, resulting in a zero Chern number typically associated with a trivial topological phase. However, topological phases in the 2D SSH model can be characterized by another \mathbb{Z}_2 topological invariant, the 2D Zak phase [186]

$$\mathbf{Z}_n = \int \int dk_x dk_y \langle u_{kn} | i\partial_k | u_{kn} \rangle, \quad (6.8)$$

where $|u_{kn}\rangle$ is the eigenstate of $\hat{h}(\mathbf{k})$ associated with the n -th band. In this work we restrict ourselves to the lower band and drop the band index. The 2D Zak phase is a vector with components Z_x and Z_y in the x and y -direction respectively. A non-zero component of the 2D Zak phase is manifested by the existence of edge states.

In the following, we choose $a_x = a_y = a$ and $\theta_m = \arccos(1/\sqrt{3})$ such that $J_{2x} = 0$. The 2D FBZ takes the form of a square with four high symmetry points, $\Gamma = (0, 0)$, $X = (\pi/a, 0)$, $M = (\pi/a, \pi/a)$ and $Y = (0, \pi/a)$. The bulk energy spectrum, normalized by the factor $\hbar\mathcal{J} = \frac{a^2}{4\pi\epsilon_0 a^3}$, through the high symmetry points in the FBZ is shown in Figure 6.3. Four different values of the hopping parameters indicated in the Figure results in a closing of the gap, marking a phase transition. By evaluating the 2D Zak phase and the energy spectrum we identify a phase diagram for the 2D SSH model with Rydberg atoms in Figure 6.4.

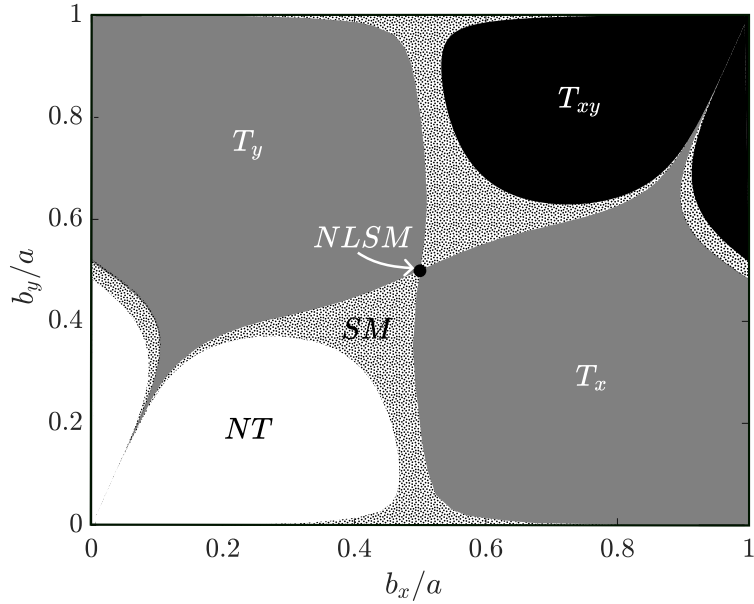


Figure 6.4: *Phase diagram of the 2D SSH model with Rydberg atoms.* Phases are determined by the sublattice offsets b_x and b_y . NT is the non-topological region, while SM is a semi-metallic phase and $NLSM$ is a nodal-line semi-metallic phase. T_x and T_y are topological regions with a topological invariant in the x and y -direction respectively, while T_{xy} is a topological region with with a topological invariant in both directions. Here the value $\theta_m = \arccos(1/\sqrt{3})$ is chosen.

A non-topological (NT) phase occurs where the 2D Zak phase is zero, however three gapped topological phases emerge when the Zak phase is non-zero, T_x with $Z_x = \pi$ and $Z_y = 0$, T_y with $Z_x = 0$ and $Z_y = -\pi$ and T_{xy} with $Z_x = \pi$ and $Z_y = -\pi$. In addition to the gapped topological phases we find a gapless semi-metallic (SM) phase manifested by a pair of topologically charged Dirac points associated with an anisotropic Dirac cone tilted as a result of broken chiral symmetry. For $b_x = b_y = a/2$, the Dirac points collapse into hyperbolic lines, which we will call the nodal-line semi-metallic ($NLSM$) phase. In the following, we will analyze these phases in detail.

6.3 Semi-metallic phase: Tunable Dirac points, tilted Dirac cones and nodal lines

Specific values of b_x and b_y in the 2D SSH model gives rise to a semi-metallic phase characterized by the emergence of a pair of Dirac points, which are singular touching points in the band structure as seen in Figure 6.5. Each Dirac point carry

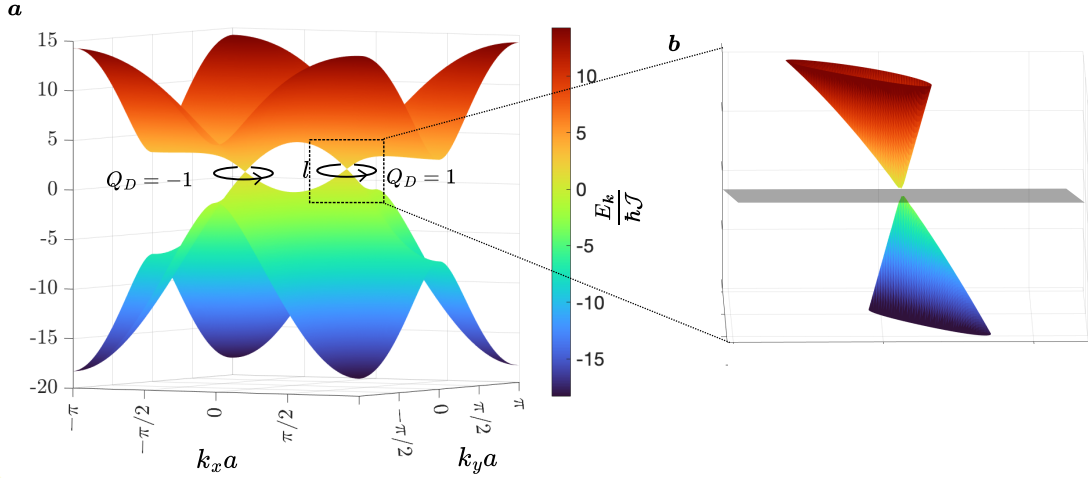


Figure 6.5: *Tilted Dirac cones* **a**: The semi-metallic phase (here $b_x = b_y = 0.6a$) characterized by a pair of Dirac points with opposite topological charge $Q_D = \pm 1$. l indicates the integration loop. **b**: The Dirac cones are both anisotropic and tilted.

a topological charge given by

$$Q_D^\pm = \frac{1}{2\pi i} \oint_L d\mathbf{k} \cdot \mathbf{n}(\mathbf{k})^{-1} \partial_{\mathbf{k}} n(\mathbf{k}), \quad (6.9)$$

where l is a path encircling a singular Dirac point. The two Dirac points always have quantized opposite charges (or chirality) of ± 1 .

Dirac points show a remarkable robustness since they can only be annihilated as they merge in either the edge or the center of the FBZ, requiring large perturbations. Dirac points are generally characterized by an isotropic, linear dispersion relation in the vicinity of the touching point. Here however, we find a dispersion relation where the linearity is not isotropic in all directions. Anisotropic Dirac cones have already been reported in graphene with external modulations including periodic potentials or uniaxial strain and intrinsically in hydrogenated graphene [187–189]. Interestingly, the Dirac cones are not only anisotropic, but also tilted [190–193] due to the slight breaking of sublattice symmetry stemming from the J_{2y} coupling (see Figure 6.5). The anisotropic and tilted nature do not change the topological features of the Dirac cones, i.e. the quantization of the topological charge is not broken, but are known to impact quantum transport properties of the system [194]. The anisotropy, tilt and the exact position of the cones in the FBZ can all be tuned in our system by changing the sublattice offsets b_x and b_y within the semi-metallic region of the phase diagram.

Typically a merging of Dirac points marks a transition into a topological trivial phase. Here however, the merging signifies either a transition into a topological non-trivial phase or a trivial phase depending on the exact values of the sublattice

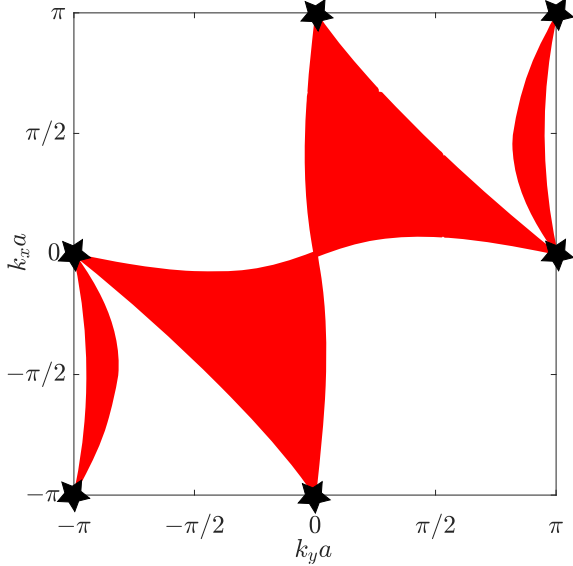


Figure 6.6: *Dirac points position*. The possible position of the Dirac points in the 2D FBZ marked by the red area. The black stars indicate the merging positions of the Dirac points in the FBZ.

offsets as seen in the phase diagram. At the exact merging point the Dirac cones have a linear dispersion relation in one direction and a parabolic dispersion relation in the orthogonal direction, similar to what has been previously studied in honeycomb lattices [195, 196] and in a variant of the 2D SSH model [176]. The uniqueness of our model lies in the exact tunability of the position of the Dirac points and the features of the associated Dirac cone by simply changing the sub-lattice offsets b_x and b_y (see Figure 6.6). The position of the Dirac points is not fully tunable over the entire 2D FBZ, but can take the positions indicated by the red area. Merging events of the Dirac cones occurs in all the high symmetry points in the 2D FBZ indicated by the black stars.

A unique instance of the semi-metallic phase occurs when $b_x = b_y = a/2$. Here, the Dirac cones points collapse, as a consequence of mirror symmetry, into nodal lines, i.e. extended gapless lines in the 2D FBZ, as seen in Figure 6.7 a. These lines come in the shape of hyperbolas and meet in the borders of the FBZ (see Figure 6.7 b). The nodal lines have a non-zero dispersion relation due to the breaking of sublattice symmetry.

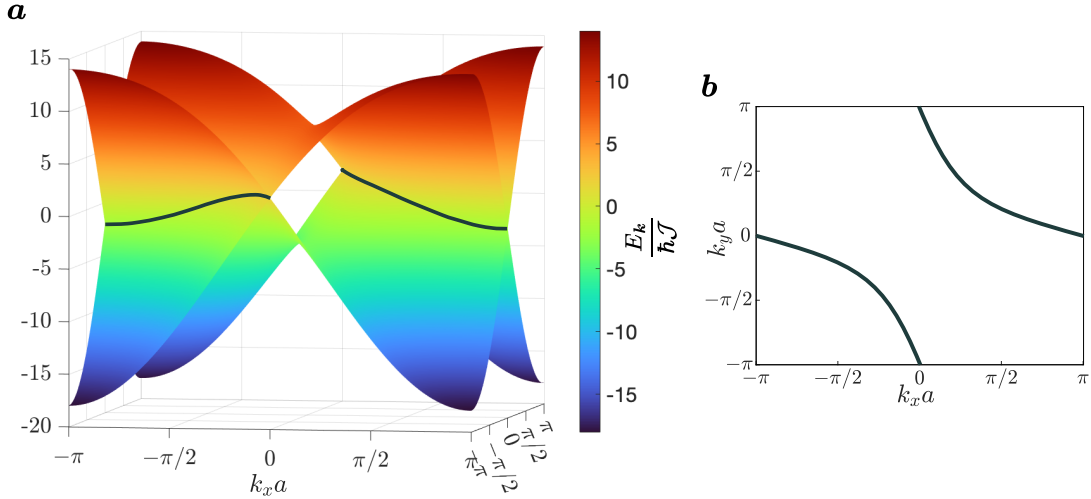


Figure 6.7: *Nodal lines* **a**: In the limit of the semi-metallic phase where $b_x = b_y = 0.5a$ the Dirac cones collapse into nodal lines, i.e. gapless lines in the FBZ. **b**: The nodal lines takes the shape of hyperbolas in the FBZ.

6.4 Topological gapped phases: Characterization of edge states

In addition to the gapless topological semi-metallic and nodal line semi-metallic phases, our model also possesses three gapped topological phases each associated by a non-zero 2D Zak phase giving rise to edge states. Due to the slight breaking of chiral symmetry, the edge states are not necessarily at zero energy, but at some finite energy still well separated from the bulk energies. Note that, due to inversion symmetry, the edge states will be doubly degenerate. Two of the gapped topological phases T_x and T_y are weak topological insulating (WTI) phases, called weak as they can be considered as weakly interacting topologically non-trivial chains. The T_x and T_y WTI phases correspond to a single non-zero component of the 2D Zak phase in the x and y -direction respectively. WTI phases are manifested by the existence of edge states occupying only one directional boundary. Contrary to what the name suggests WTIs actually display a remarkable robustness against disorder [197].

6.4.1 Semi-infinite system

To investigate the existence of edge states in a 2D system, it is useful to start by considering a semi-infinite system, i.e. keep one of the two dimensions small and the other infinite. For illustration purposes, we consider here a system of $M = 16$ atoms in the y -direction and an infinite number of atoms in the x -direction. Doing

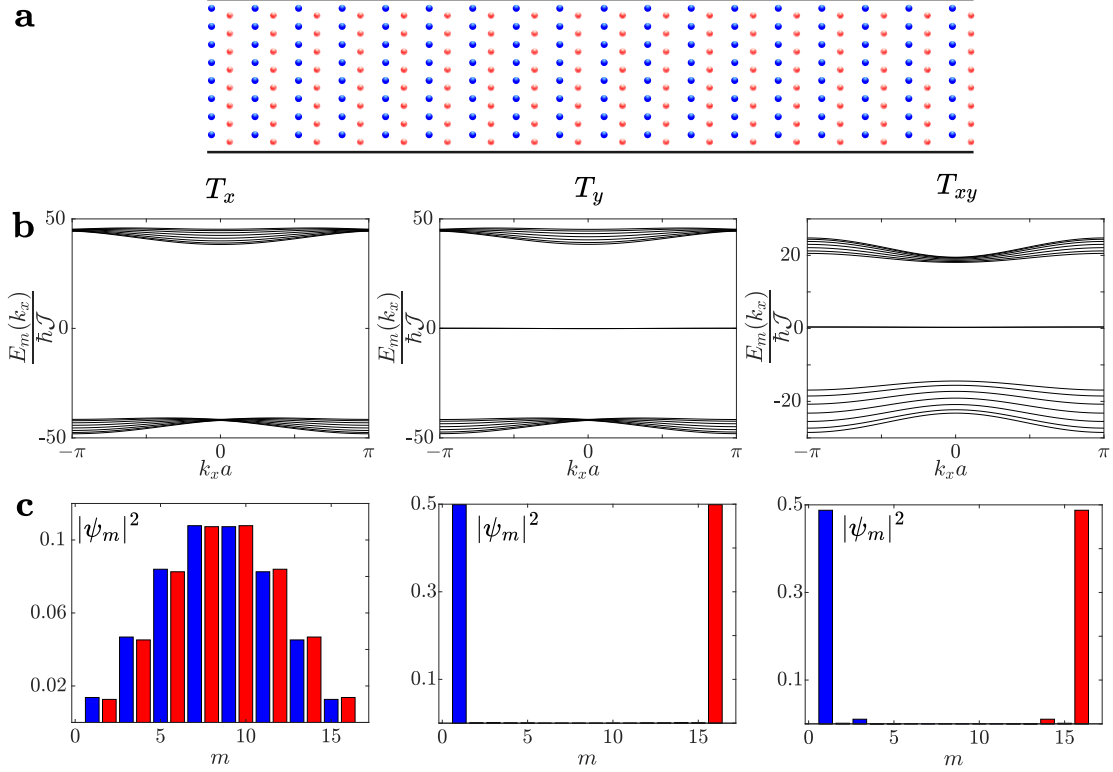


Figure 6.8: *Semi-infinite system in the x-direction.* **a:** The lattice is infinite in the x -direction and finite in the y -direction with $M = 16$ atoms. The black lines indicate the boundary. **b:** The energies $E_m(k_x)$ of the partial Fourier transformed Hamiltonian $H(k_x)$ in the three topological gapped regions T_x , T_y and T_{xy} . **c:** Magnitude of the corresponding eigenstates $|\psi_m|^2$ where blue/red bars correspond to sites on sublattice A/B. The sublattice offsets are $b_x = 0.8a$ and $b_y = 0.2a$ in the T_x phase, $b_x = 0.2a$ and $b_y = 0.8a$ in the T_y phase and $b_x = 0.8a$ and $b_y = 0.8a$ in the T_{xy} phase.

so allows us to take a partial Fourier transform in the x -direction of the operators in the Hamiltonian given in equation (6.1)

$$\begin{aligned}\hat{a}_{nm} &= \frac{1}{\sqrt{N/2}} \sum_{k_x} e^{ik_x x_n} \hat{a}_{k_x m}, \\ \hat{b}_{nm} &= \frac{1}{\sqrt{N/2}} \sum_{k_x} e^{ik_x x_n} \hat{b}_{k_x m}.\end{aligned}\tag{6.10}$$

The partial Fourier transformed Hamiltonian may be written in a simplified form $\hat{H} = \sum_{k_x} \hat{H}(k_x)$, where

$$\begin{aligned}\hat{H}(k_x) &= \hbar \left\{ \sum_{m=1}^M (J'_x + J_x e^{-ik_x a_x}) \hat{a}_{k_x m}^\dagger \hat{b}_{k_x m} + (J'_y + J_y e^{ik_x a_x}) \hat{b}_{k_x m+1}^\dagger \hat{a}_{k_x m} \right. \\ &\quad \left. + J_{2y} (\hat{a}_{k_x m}^\dagger \hat{a}_{k_x m} + \hat{b}_{k_x m}^\dagger \hat{b}_{k_x m}) + \text{h.c.} \right\},\end{aligned}\tag{6.11}$$

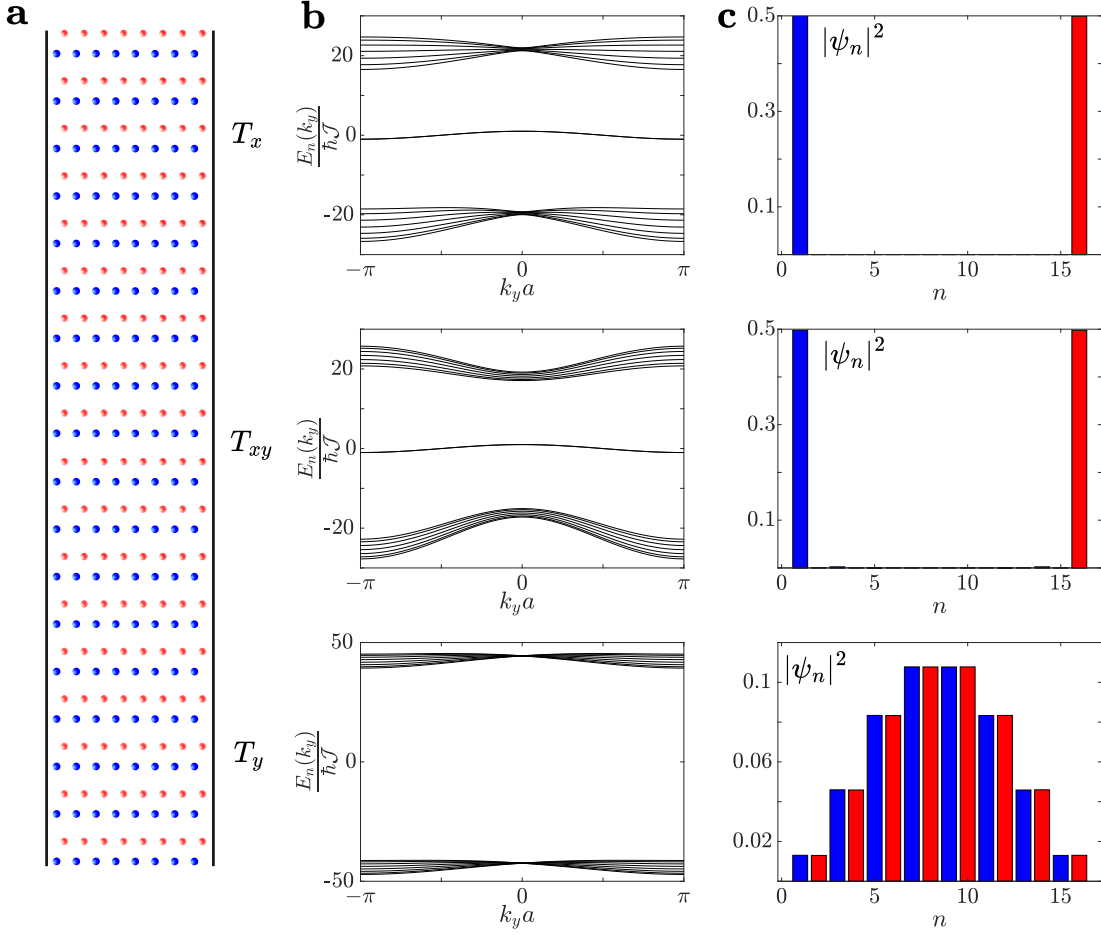


Figure 6.9: *Semi-infinite system in the y -direction.* **a:** The lattice is infinite in the y -direction and finite in the x -direction with $N = 16$ atoms. The black lines indicate the boundary. **b:** The energies $E_n(k_y)$ of the partial Fourier transformed Hamiltonian $H(k_t)$ in the three topological gapped regions T_x , T_y and T_{xy} . **c:** Magnitude of the corresponding eigenstates $|\psi_n|^2$ where blue/red bars correspond to sites on sublattice A/B. The sublattice offsets are $b_x = 0.8a$ and $b_y = 0.2a$ in the T_x phase, $b_x = 0.2a$ and $b_y = 0.8a$ in the T_y phase and $b_x = 0.8a$ and $b_y = 0.8a$ in the T_{xy} phase.

where J_{2y} now acts as an on-site constant energy and k_x acts as a parameter. Edge states can now be identified by diagonalizing the above Hamiltonian and inspecting the edge occupancy of the eigenstates. Figure 6.8 shows the eigenenergies E_m as a function of k_x in the three different gapped topological regions. The T_y and T_{xy} regions show edge states ψ_m at the energy $\hbar J_{2y} = \hbar J$ well separated from the bulk energies, exponentially localized to both edges, while in the T_x region only bulk states appear since the chains in the x -direction are infinite.

The same partial Fourier transform can be performed when considering an infinite number of atoms in the y -direction and a finite number in the x -direction (here $N = 16$ for illustration purposes). Using a partial Fourier transform in the

y-direction

$$\begin{aligned}\hat{a}_{nm} &= \frac{1}{\sqrt{M/2}} \sum_{k_y} e^{ik_y y_m} \hat{a}_{nk_y}, \\ \hat{b}_{nm} &= \frac{1}{\sqrt{M/2}} \sum_{k_y} e^{ik_y y_m} \hat{b}_{nk_y},\end{aligned}\quad (6.12)$$

the partial Fourier transformed Hamiltonian $\hat{H} = \sum_{k_y} \hat{H}(k_y)$ can be expressed as

$$\begin{aligned}\hat{H}(k_y) &= \hbar \left\{ \sum_{n=1}^N (J'_x + J'_y e^{ik_y a_y}) \hat{a}_{nk_y}^\dagger \hat{b}_{nk_y} + (J_x + J_y e^{-ik_y a_y}) \hat{b}_{nk_y}^\dagger \hat{a}_{n+1k_y} \right. \\ &\quad \left. + J_{2y} e^{ik_y a_y} (\hat{a}_{nk_y}^\dagger \hat{a}_{nk_y} + \hat{b}_{nk_y}^\dagger \hat{b}_{nk_y}) + \text{h.c.} \right\}.\end{aligned}\quad (6.13)$$

Equivalently to the previous case we can calculate the eigenstates of this Hamiltonian in the three topological gapped regions of the phase diagram (see Figure 6.9). As expected, edge states appear in the T_x and T_{xy} regions while the eigenstates in the T_y region are bulk states. Since the edge states occupy the boundaries in the *x*-direction, the intra-sublattice interactions along this edge J_{2y} induces a non-zero dispersion relation for the edge state energies as seen in Figure 6.9, i.e. the edge state energy $E_n(k_y)$ is not flat as a function of the momentum k_y .

6.4.2 Finite system

Now we will consider a finite system with $M = N = 24$. The eigenstates of the full Hamiltonian given in equation (6.1) is on the form $|\psi\rangle = \sum_{n,m} c_{n,m} |e_{n,m}\rangle$ where $c_{n,m}$ are constants and $|e_{n,m}\rangle = |r_{1,1}\rangle \otimes |r_{1,2}\rangle \otimes \dots \otimes |e\rangle_{n,m} \otimes |r_{n,m+1}\rangle \otimes \dots \otimes |r_{N,M}\rangle$ is a Rydberg atom on site (n, m) excited to the upper state with all other Rydberg atoms in the lower state. Figure 6.10 shows the lattice (indicated by black dots) for different values of the sublattice offsets within the three gapped topological regimes given in the figure text. Figure 6.10a-d shows two selected edge states in the T_x and T_y phase where the blue/red dots indicate lattice sites where the wavefunction $|\psi\rangle$ is non-zero on sublattice A/B with the size of the dot corresponding to the magnitude of the wavefunction. In the T_x phase edge states appear on either side of the *x*-boundaries of the system, while in the T_y phase the edge states appear on the boundary in the *y*-direction and correspond to WTI edge states.

The last topological gapped phase, T_{xy} , is characterized by both components of the 2D Zak phase being non-zero. In contrast to the WTI phases, here, edge states can occupy both the boundaries in the *x* and *y*-direction as seen in Figure

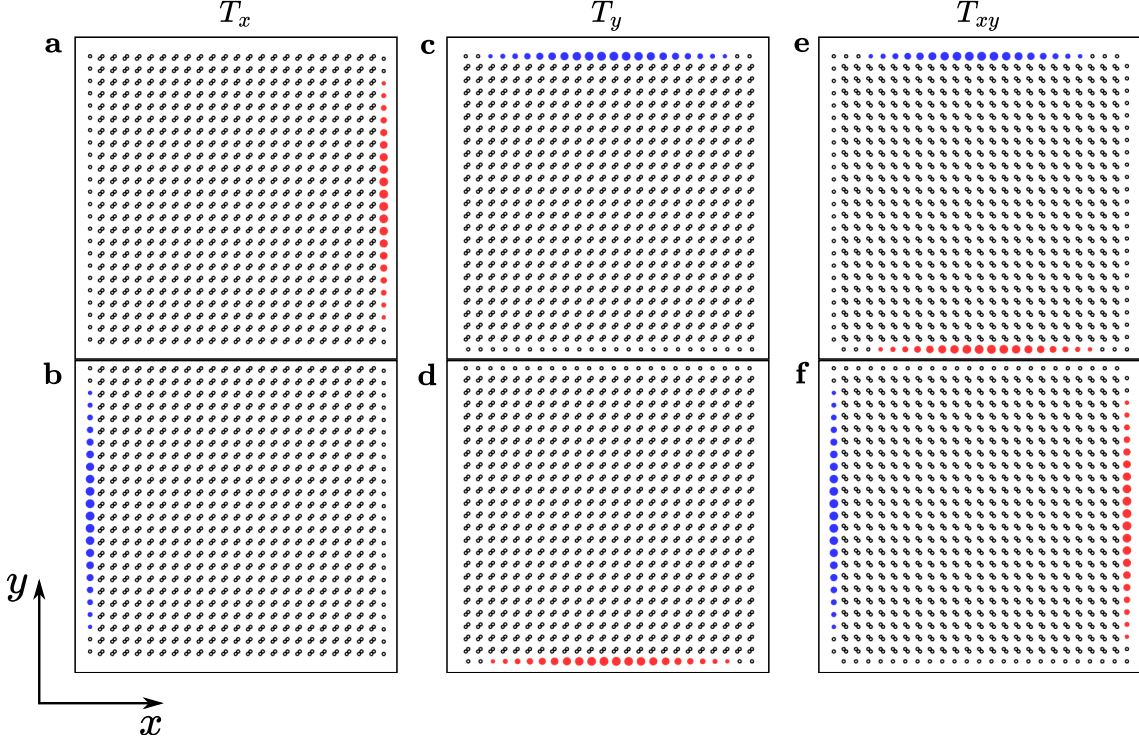


Figure 6.10: *Edge states in topologically gapped phases.* The black dots indicate the lattice sites and the blue/red dots indicate lattice sites where the wavefunction is non-zero on sublattice A/B with the size of the dot corresponding to the magnitude of the wavefunction. In the T_x phase, here $b_x = 0.8a$ and $b_y = 0.2a$, edge states occur on the boundary in x -direction (a and b). In the T_y phase, here $b_x = 0.2a$ and $b_y = 0.8a$, edge states occur on the boundary in y -direction (c and d). In the T_{xy} region, here $b_x = 0.8a$ and $b_y = 0.8a$, the edge states can be on either the y -boundary (e) or the x -boundary (f).

6.10e-f.

In the literature, topological phases associated with a two-component topological invariant are typically called higher order topological insulators (HOTI). While the WTI phase was associated with having edge states or occupation localized on the boundary, HOTI phases have occupation localized on the boundary of the boundaries, which in two dimensions are the corners. In HOTI phases corner states are protected by the coexistence of time-reversal, particle-hole and chiral symmetries [198, 199]. Due to the breaking of chiral and particle hole symmetry induced by the J_{2y} term, corner states are not present in the 2D Rydberg lattice for $\theta_m = \arccos(1/\sqrt{3})$ and the T_{xy} phase resembles a WTI phase.

However, tilting the dipole angle θ_m such that chiral symmetry is equally, but weakly broken in both the x and y -direction, i.e. $J_{2y} = J_{2x} = \mathcal{J}/2$, reveals corner-like states in the T_{xy} region (see Figure 6.11a). The corner states are not exponentially localized, which is the case for chiral HOTI phases, but display a polynomial localization. Although not realizable in our model, Figure 6.11b shows a

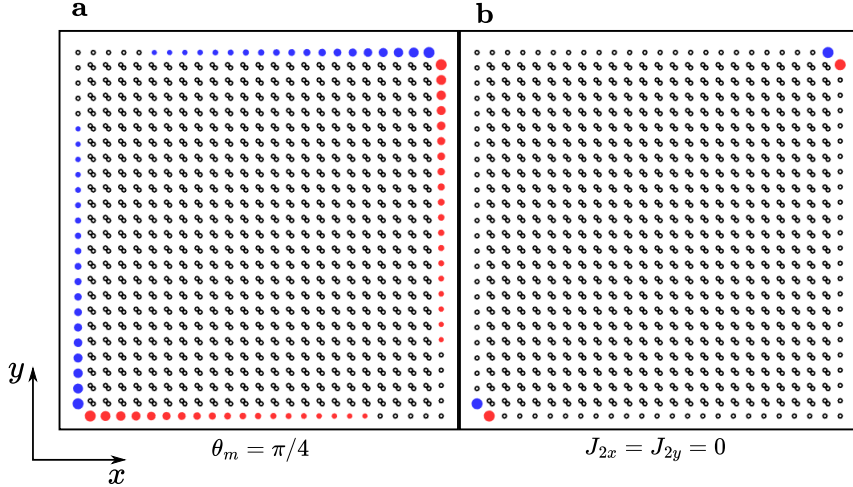


Figure 6.11: *Corner-like states in the T_{xy} phase.* **a:** For the dipole angle $\theta_m = \pi/4$, corner-like states appear. **b:** Setting $J_{2y} = J_{2x} = 0$ reveals perfect corner states.

perfect corner state by setting $J_{2y} = J_{2x} = 0$ by hand. The top left and bottom right corners are shared edges of a horizontal and vertical SSH chain. Due to the opposite phase of the wavefunction at these shared edges, corner states are not excited here.

The three gapped topological phases are all connected through an extended semi-metallic phase, meaning there are no transitions between the three phases without an intermediate transition to a semi-metallic phase.

6.4.3 Edge excitation dynamics

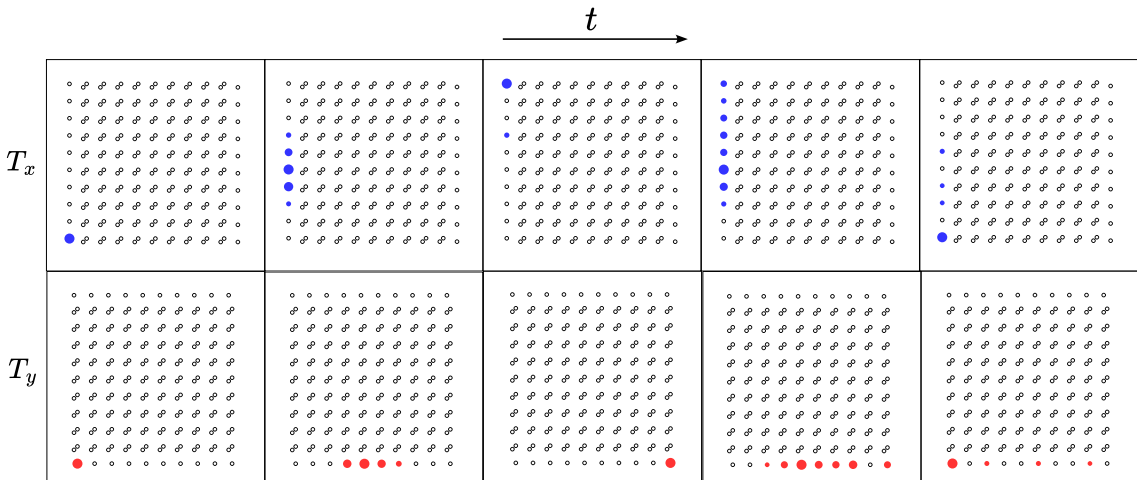


Figure 6.12: *Edge excitation dynamics in the T_x and T_y phase.* In the T_x phase, $b_x = 0.8a$ and $b_y = 0.2a$ is chosen while in the T_y phase, $b_x = 0.2a$ and $b_y = 0.8a$ is chosen.

Here, we study the excitation dynamics for $N = M = 20$ when initially exciting a single Rydberg atom to the upper state $|e\rangle$ on the edge and evolve the

state using the full Hamiltonian (6.1). As expected, an excitation created in on an edge in the WTI phases, T_x and T_y , evolves like a wavepacket on the respective boundaries and localizes and bounces back when reaching the corners as seen in Figure 6.12. After hitting the corner the state interferes with itself and leading to non-perfect localization when returning to the initial corner.

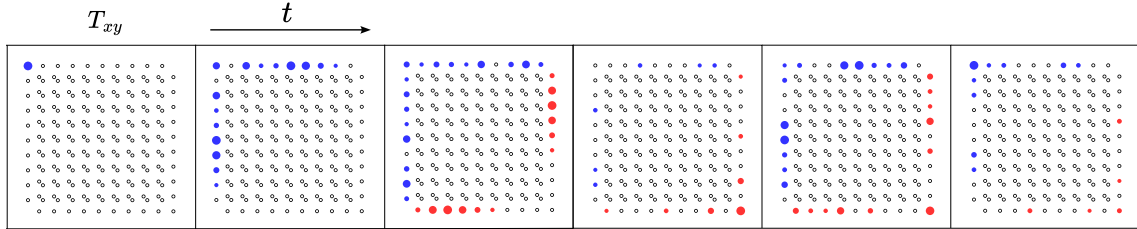


Figure 6.13: *Edge excitation dynamics in the T_{xy} phase.* An initial excitation is prepared in the top left corner. Here, $b_x = b_y = 0.75a$ is chosen.

In the T_{xy} phase (here with $\theta_m = \pi/4$), an initial corner excitation evolves bidirectional and bounces as they meet in the opposite corner as seen in Figure 6.13. Here we do not achieve chiral excitation edge currents as realized in previous studies [66, 200].

6.4.4 Robustness against defects

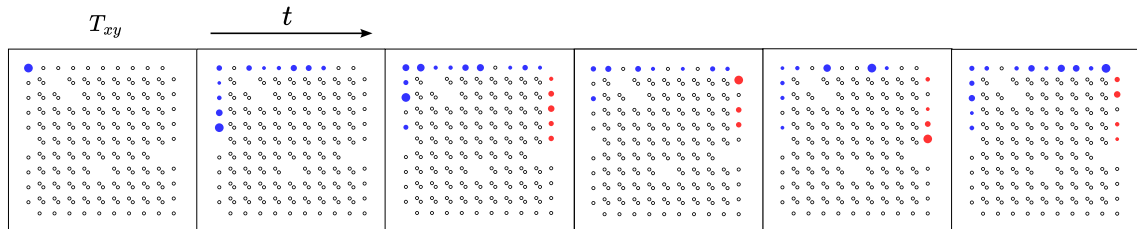


Figure 6.14: *Robustness in the T_{xy} phase.* An initial excitation is prepared in the top left corner in a lattice with 5% defects. Here, $b_x = b_y = 0.75a$ is chosen.

Topological phases display a remarkable robustness against local perturbations. Here, we quantify the robustness of the T_{xy} phase against defects in the lattice. To do so we randomly remove cells from the lattice and study the edge excitation dynamics in the presence of these lattice defects. When the lattice defects are located in the bulk of the lattice, their presence does not alter the edge dynamics. However, when a defect is present on the boundary the propagation of the excitation is interrupted. However, the excitation does not leak into the bulk, but stays on the edge where the defect acts as a hard wall and reflects the incoming wavepacket as seen in Figure 6.14 showing the robustness of the topological phases. Similar results can be obtained in the WTI phases.

6.5 Conclusion and outlook

Both gapped and gapless topological phases display robust properties that are not only interesting theoretically, but can also be harvested for applications in quantum technologies. In this study we have presented an experimentally realizable platform using Rydberg atoms in offset square sublattices, that display both gapped and gapless topological phases connected by the sublattice offset parameters. Directional edge states, where the edge states only appear on the boundaries in the x or y -direction, are found in the gapped weak topological insulating phases protected by a quantized component of the 2D Zak phase. In one parameter regime we find a higher order topological insulating phase, manifested by edge states present on all boundaries. Tweaking the Hamiltonian parameters reveals corner-like states, not with exponential localization, but with polynomial due to the inherent broken chiral symmetry of the system. The gapless semi-metallic phase is characterized by a pair of topologically charged, anisotropic Dirac cones. The breaking of chiral symmetry is manifested by an induced tilt of the cones. Anisotropic and tilted Dirac cones are known modulate the systems quantum transport properties. In the highest symmetry point of the phase diagram we find a nodal-line semi-metallic phase protected by mirror symmetry.

A natural outlook of this work is a potential experimental observation of edge states in the gapped topological phases. The setup outlined in this work is a 2D extension of a previous experimental setup [81]. Considering, like in the reference, ^{87}Rb atoms individually trapped in an array of optical tweezers, the Rydberg atoms can be modeled as two-level systems with a two-level ground state being the $|60S_{1/2}\rangle$ state and excited state being the $|60P_{1/2}\rangle$ state. With the lattice parameter $a = 12 \mu\text{m}$ in the T_{xy} phase with $b_x = b_y = 0.8a$, the nearest neighbour couplings is given by $J_x/\hbar = 1.94\text{Mhz}$, $J'_x/\hbar = -0.42\text{Mhz}$, $J_y/\hbar = 27.20\text{Mhz}$ and $J'_y/\hbar = 0.89\text{Mhz}$.

Chapter 7

Conclusion and outlook

In this Thesis we studied the topological properties of many-body quantum optical systems consisting of emitters interacting through dipole-dipole exchange interactions from short-range to all-to-all couplings in one and two dimensional arrays realized with Rydberg atoms, atoms in low-lying electronic states and emitters coupled to a nanophotonic waveguide. We demonstrated how to analytically calculate the guided part of the dipole-dipole interactions for emitters coupled to a nanophotonic waveguide and provided a numerical recipe for the calculation of the radiation part of the interactions. We showed that the radiation part differed significantly from its free space counterpart especially when the emitters are close to the waveguide surface, or when the number of emitters is increased. Through the dipole-dipole exchange interactions we demonstrated that the concept of topological pumping can be extended to systems with long-range and even all-to-all interactions. We showed high fidelity topological pumping of a photon embedded in the three quantum optical systems above using experimentally relevant parameters. The pumping process displayed a remarkable robustness against disorder in the emitter positions as a result of topological protection. Finally, we presented a 2D lattice model with Rydberg atoms displaying multiple topological phases with zero Berry curvature, resulting in a zero Chern number, but protected by the quantized 2D Zak phase. In some parameter regimes a semimetallic phase appears manifested by the existence of topologically charged, tilted and anisotropic Dirac cones. Both the position and properties of the Dirac cones are tunable with the system parameters. For specific values of the system parameters, the Dirac points collapse into nodal lines due to mirror symmetry. We also find topological insulator phases characterized by edge states. The edge states were found to be directional, connected to weak topological insulator phases in condensed matter physics, or corner like states for specific parameter choices resembling a higher order topological insulator. However, perfectly loc-

alized corner states are only possible when the chiral symmetry is not broken.

A natural extension to the work presented in this Thesis is to consider robust quantum state transfer in the three systems discussed in Chapter 5 to study the possibility of edge mode transfer in systems with long-range interactions, allowing for transport over longer distances compared to topological pumping. This could be done in even or odd length SSH chains or in the Rice-Mele model [135–142] as discussed in Section 3.5 and analyses can be performed in order to find which protocol gives the highest transfer efficiency, which will both depend on the transfer time and the transfer fidelity. The Rice-Mele model and odd-site SSH model would be the easiest to implement for edge state transfer in the three systems as the restrictions in the parameter values is not as strict as for the even-site SSH model. The Rydberg chain with dipole-dipole exchange interactions can be mapped directly to existing protocols in nearest neighbour SSH chains or Rice-Mele model. Here however, the transfer time is crucial as the transfer is limited by the lifetime of the Rydberg excitation. For atom chains in low-lying states and atoms coupled to a waveguide, the chains can be made subradiant as outlined in Chapter 5, which overcomes the issue of losing excitations.

Quantum state transfer has also been realized in two and three dimensional systems, mainly in spin-models [131, 201, 202]. However, the possibility of robust quantum state transfer of edge states in higher dimensional topological models is still an open question. The 2D SSH model with Rydberg atoms presented in Chapter 6 could potentially be a platform to achieve this. In the 2D SSH model we found different topological phases, by tuning the position of the Rydberg atoms, that supported directional edge states, i.e. the supported edge eigenstates only occupied single boundaries. Adiabatically connecting two of these topological phases by changing the sublattice offsets would allow for a transfer of an initial state on one boundary supported in one topological phase to another boundary state supported in the other topological phase. The main problem here are the degeneracy or nearly degenerate edge eigenstates on the opposite boundaries in the same topological phase. However, the opposite boundaries are formed by sites only on opposite sublattices. Introducing a sublattice energy shift, as for example is the case in the Rice-Mele model, this degeneracy will be lifted. Furthermore, robust quantum state transfer requires adiabatic evolution of the parameters, meaning that the lifetime of the Rydberg excitation may be a limitation.

Finally, despite the zero Chern number, topological pumping in two-dimensions could be studied in the 2D SSH Rydberg model. Deep in the T_x and T_y phase, the lattice can be considered as weakly coupled, independent SSH chains. This would allow us, similarly as to what is considered in a previous work [169], to assign Berry curvatures in two directions with one of the momenta as one para-

meter and introduce time as the other parameter. This would allow for controlled and robust transport of excitations in the bulk of the lattice.

Bibliography

- [1] P. A. M. Dirac, "Quantised singularities in the electromagnetic field," *Proceedings: Math. and Phys.*, vol. 133, no. 821, pp. 60–72, 1931.
- [2] K. v. Klitzing, G. Dorda, and M. Pepper, "New method for high-accuracy determination of the fine-structure constant based on quantized hall resistance," *Phys. Rev. Lett.*, vol. 45, pp. 494–497, 1980.
- [3] B. Q. Lv, H. M. Weng, B. B. Fu, X. P. Wang, H. Miao, J. Ma, P. Richard, X. C. Huang, L. X. Zhao, G. F. Chen, Z. Fang, X. Dai, T. Qian, and H. Ding, "Experimental discovery of weyl semimetal TaAs," *Phys. Rev. X*, vol. 5, p. 031013, 2015.
- [4] S. M. Young, S. Zaheer, J. C. Y. Teo, C. L. Kane, E. J. Mele, and A. M. Rappe, "Dirac semimetal in three dimensions," *Phys. Rev. Lett.*, vol. 108, p. 140405, 2012.
- [5] A. A. Burkov and L. Balents, "Weyl semimetal in a topological insulator multilayer," *Phys. Rev. Lett.*, vol. 107, p. 127205, 2011.
- [6] Z. K. Liu, B. Zhou, Y. Zhang, Z. J. Wang, H. M. Weng, D. Prabhakaran, S.-K. Mo, Z. X. Shen, Z. Fang, X. Dai, Z. Hussain, and Y. L. Chen, "Discovery of a three-dimensional topological dirac semimetal, Na₃Bi," *Science*, vol. 343, no. 6173, pp. 864–867, 2014.
- [7] M. Sato and Y. Ando, "Topological superconductors: a review," *Rep. Prog. Phys.*, vol. 80, no. 7, p. 076501, 2017.
- [8] Y.-B. Yang, J.-H. Wang, K. Li, and Y. Xu, "Higher-order topological phases in crystalline and non-crystalline systems: a review," *J. Phys. Condens. Matter*, vol. 36, no. 28, p. 283002, 2024.
- [9] X.-J. Luo, X.-H. Pan, C.-X. Liu, and X. Liu, "Higher-order topological phases emerging from su-schrieffer-heeger stacking," *Phys. Rev. B*, vol. 107, p. 045118, 2023.

- [10] W. A. Benalcazar and A. Cerjan, "Chiral-symmetric higher-order topological phases of matter," *Phys. Rev. Lett.*, vol. 128, p. 127601, 2022.
- [11] D. Călugăru, V. Juričić, and B. Roy, "Higher-order topological phases: A general principle of construction," *Phys. Rev. B*, vol. 99, p. 041301, 2019.
- [12] J. Alicea, "New directions in the pursuit of majorana fermions in solid state systems," *Rep. Prog. Phys.*, vol. 75, no. 7, p. 076501, 2012.
- [13] T. Ozawa, H. M. Price, A. Amo, N. Goldman, M. Hafezi, L. Lu, M. C. Rechtsman, D. Schuster, J. Simon, O. Zilberberg, and I. Carusotto, "Topological photonics," *Rev. Mod. Phys.*, vol. 91, p. 015006, 2019.
- [14] H. Bachmair, E. O. Göbel, G. Hein, J. Melcher, B. Schumacher, J. Schurr, L. Schweitzer, and P. Warnecke, "The von Klitzing resistance standard," *Phys. E: Low-Dimens. Syst. Nanostructures*, vol. 20, no. 1, pp. 14–23, 2003.
- [15] M. Lohse, C. Schweizer, O. Zilberberg, M. Aidelsburger, and I. Bloch, "A Thouless quantum pump with ultracold bosonic atoms in an optical superlattice," *Nat. Phys.*, vol. 12, no. 4, pp. 350–354, 2016.
- [16] S. Nakajima, T. Tomita, S. Taie, T. Ichinose, H. Ozawa, L. Wang, M. Troyer, and Y. Takahashi, "Topological Thouless pumping of ultracold fermions," *Nat. Phys.*, vol. 12, no. 4, pp. 296–300, 2016.
- [17] Y. Xia, E. Riva, M. I. N. Rosa, G. Cazzulani, A. Erturk, F. Braghin, and M. Ruzzene, "Experimental observation of temporal pumping in electromechanical waveguides," *Phys. Rev. Lett.*, vol. 126, p. 095501, 2021.
- [18] I. H. Grinberg, M. Lin, C. Harris, W. A. Benalcazar, C. W. Peterson, T. L. Hughes, and G. Bahl, "Robust temporal pumping in a magneto-mechanical topological insulator," *Nat. Commun.*, vol. 11, no. 1, p. 974, 2020.
- [19] Z. Fedorova, H. Qiu, S. Linden, and J. Kroha, "Observation of topological transport quantization by dissipation in fast Thouless pumps," *Nat. Commun.*, vol. 11, no. 1, p. 3758, 2020.
- [20] D. Dreon, A. Baumgärtner, X. Li, S. Hertlein, T. Esslinger, and T. Donner, "Self-oscillating pump in a topological dissipative atom–cavity system," *Nature*, vol. 608, no. 7923, pp. 494–498, 2022.
- [21] Y. E. Kraus, Y. Lahini, Z. Ringel, M. Verbin, and O. Zilberberg, "Topological states and adiabatic pumping in quasicrystals," *Phys. Rev. Lett.*, vol. 109, p. 106402, 2012.

- [22] M. Verbin, O. Zilberberg, Y. Lahini, Y. E. Kraus, and Y. Silberberg, "Topological pumping over a photonic fibonacci quasicrystal," *Phys. Rev. B*, vol. 91, p. 064201, 2015.
- [23] R. H. Dicke, "Coherence in spontaneous radiation processes," *Phys. Rev.*, vol. 93, pp. 99–110, 1954.
- [24] P. Tighineanu, R. S. Daveau, T. B. Lehmann, H. E. Beere, D. A. Ritchie, P. Lodahl, and S. Stobbe, "Single-photon superradiance from a quantum dot," *Phys. Rev. Lett.*, vol. 116, p. 163604, 2016.
- [25] P. Lodahl, A. Floris van Driel, I. S. Nikolaev, A. Irman, K. Overgaag, D. Vanmaekelbergh, and W. L. Vos, "Controlling the dynamics of spontaneous emission from quantum dots by photonic crystals," *Nature*, vol. 430, no. 7000, pp. 654–657, 2004.
- [26] Y. Chen, Z. Yu, and H. Zhai, "Superradiance of degenerate fermi gases in a cavity," *Phys. Rev. Lett.*, vol. 112, p. 143004, 2014.
- [27] J. A. Mlynek, A. A. Abdumalikov, C. Eichler, and A. Wallraff, "Observation of Dicke superradiance for two artificial atoms in a cavity with high decay rate," *Nat. Commun.*, vol. 5, no. 1, p. 5186, 2014.
- [28] D. Schneble, Y. Torii, M. Boyd, E. W. Streed, D. E. Pritchard, and W. Ketterle, "The onset of matter-wave amplification in a superradiant bose-einstein condensate," *Science*, vol. 300, no. 5618, pp. 475–478, 2003.
- [29] S. Inouye, A. P. Chikkatur, D. M. Stamper-Kurn, J. Stenger, D. E. Pritchard, and W. Ketterle, "Superradiant rayleigh scattering from a bose-einstein condensate," *Science*, vol. 285, no. 5427, pp. 571–574, 1999.
- [30] D. Pavolini, A. Crubellier, P. Pillet, L. Cabaret, and S. Liberman, "Experimental evidence for subradiance," *Phys. Rev. Lett.*, vol. 54, pp. 1917–1920, 1985.
- [31] J. A. Needham, I. Lesanovsky, and B. Olmos, "Subradiance-protected excitation transport," *New J. Phys.*, vol. 21, no. 7, p. 073061, 2019.
- [32] M. Cech, I. Lesanovsky, and B. Olmos, "Dispersionless subradiant photon storage in one-dimensional emitter chains," *Phys. Rev. A*, vol. 108, p. L051702, 2023.
- [33] J. Kim, D. Yang, S. hoon Oh, and K. An, "Coherent single-atom superradiance," *Science*, vol. 359, no. 6376, pp. 662–666, 2018.

- [34] R. Jones, J. A. Needham, I. Lesanovsky, F. Intravaia, and B. Olmos, "Modified dipole-dipole interaction and dissipation in an atomic ensemble near surfaces," *Phys. Rev. A*, vol. 97, p. 053841, 2018.
- [35] K. Sinha, B. P. Venkatesh, and P. Meystre, "Collective effects in casimir-polder forces," *Phys. Rev. Lett.*, vol. 121, p. 183605, 2018.
- [36] S. Fuchs and S. Y. Buhmann, "Purcell-dicke enhancement of the casimir-polder potential," *Europhys. Lett.*, vol. 124, no. 3, p. 34003, 2018.
- [37] A. Asenjo-Garcia, J. D. Hood, D. E. Chang, and H. J. Kimble, "Atom-light interactions in quasi-one-dimensional nanostructures: A green's-function perspective," *Phys. Rev. A*, vol. 95, p. 033818, 2017.
- [38] D. Dzsotjan, A. S. Sørensen, and M. Fleischhauer, "Quantum emitters coupled to surface plasmons of a nanowire: A green's function approach," *Phys. Rev. B*, vol. 82, p. 075427, 2010.
- [39] E. M. Purcell, H. C. Torrey, and R. V. Pound, "Resonance absorption by nuclear magnetic moments in a solid," *Phys. Rev.*, vol. 69, pp. 37–38, 1946.
- [40] P. Goy, J. M. Raimond, M. Gross, and S. Haroche, "Observation of cavity-enhanced single-atom spontaneous emission," *Phys. Rev. Lett.*, vol. 50, pp. 1903–1906, 1983.
- [41] G. Gabrielse and H. Dehmelt, "Observation of inhibited spontaneous emission," *Phys. Rev. Lett.*, vol. 55, pp. 67–70, 1985.
- [42] R. G. Hulet, E. S. Hilfer, and D. Kleppner, "Inhibited spontaneous emission by a rydberg atom," *Phys. Rev. Lett.*, vol. 55, pp. 2137–2140, 1985.
- [43] J. Martorell and N. M. Lawandy, "Observation of inhibited spontaneous emission in a periodic dielectric structure," *Phys. Rev. Lett.*, vol. 65, pp. 1877–1880, 1990.
- [44] E. Vetsch, D. Reitz, G. Sagué, R. Schmidt, S. T. Dawkins, and A. Rauschenbeutel, "Optical interface created by laser-cooled atoms trapped in the evanescent field surrounding an optical nanofiber," *Phys. Rev. Lett.*, vol. 104, p. 203603, 2010.
- [45] L. Ding, C. Belacel, S. Ducci, G. Leo, and I. Favero, "Ultralow loss single-mode silica tapers manufactured by a microheater," *Appl. Opt.*, vol. 49, no. 13, pp. 2441–2445, 2010.

- [46] P. Lodahl, S. Mahmoodian, and S. Stobbe, "Interfacing single photons and single quantum dots with photonic nanostructures," *Rev. Mod. Phys.*, vol. 87, pp. 347–400, 2015.
- [47] R. Ritter, N. Gruhler, H. Dobbertin, H. Kübler, S. Scheel, W. Pernice, T. Pfau, and R. Löw, "Coupling thermal atomic vapor to slot waveguides," *Phys. Rev. X*, vol. 8, p. 021032, 2018.
- [48] A. Skljarow, N. Gruhler, W. Pernice, H. Kübler, T. Pfau, R. Löw, and H. Alaeian, "Integrating two-photon nonlinear spectroscopy of rubidium atoms with silicon photonics," *Opt. Express*, vol. 28, no. 13, pp. 19593–19607, 2020.
- [49] A. Skljarow, H. Kübler, C. S. Adams, T. Pfau, R. Löw, and H. Alaeian, "Purcell-enhanced dipolar interactions in nanostructures," *Phys. Rev. Res.*, vol. 4, p. 023073, 2022.
- [50] D. Reitz, C. Sayrin, R. Mitsch, P. Schneeweiss, and A. Rauschenbeutel, "Coherence properties of nanofiber-trapped cesium atoms," *Phys. Rev. Lett.*, vol. 110, p. 243603, 2013.
- [51] P. Lodahl, S. Mahmoodian, S. Stobbe, A. Rauschenbeutel, P. Schneeweiss, J. Volz, H. Pichler, and P. Zoller, "Chiral quantum optics," *Nature*, vol. 541, p. 473, 2017.
- [52] V. A. Pivovarov, L. V. Gerasimov, J. Berroir, T. Ray, J. Laurat, A. Urvoy, and D. V. Kupriyanov, "Single collective excitation of an atomic array trapped along a waveguide: A study of cooperative emission for different atomic chain configurations," *Phys. Rev. A*, vol. 103, p. 043716, 2021.
- [53] P. Solano, P. Barberis-Blostein, F. K. Fatemi, and et al., "Super-radiance reveals infinite-range dipole interactions through a nanofiber," *Nat. Commun.*, vol. 8, p. 1857, 2017.
- [54] R. Pennetta, D. Lechner, M. Blaha, A. Rauschenbeutel, P. Schneeweiss, and J. Volz, "Observation of coherent coupling between super- and subradiant states of an ensemble of cold atoms collectively coupled to a single propagating optical mode," *Phys. Rev. Lett.*, vol. 128, p. 203601, 2022.
- [55] A. Asenjo-Garcia, M. Moreno-Cardoner, A. Albrecht, H. J. Kimble, and D. E. Chang, "Exponential improvement in photon storage fidelities using subradiance and "selective radiance" in atomic arrays," *Phys. Rev. X*, vol. 7, p. 031024, 2017.

- [56] A. Albrecht, L. Henriet, A. Asenjo-Garcia, P. B. Dieterle, O. Painter, and D. E. Chang, "Subradiant states of quantum bits coupled to a one-dimensional waveguide," *New J. Phys.*, vol. 21, no. 2, p. 025003, 2019.
- [57] G. Buonaiuto, R. Jones, B. Olmos, and I. Lesanovsky, "Dynamical creation and detection of entangled many-body states in a chiral atom chain," *New J. Phys.*, vol. 21, no. 11, p. 113021, 2019.
- [58] S. Mahmoodian, G. Calajó, D. E. Chang, K. Hammerer, and A. S. Sørensen, "Dynamics of many-body photon bound states in chiral waveguide qed," *Phys. Rev. X*, vol. 10, p. 031011, 2020.
- [59] Y. L. Wang, Y. Yang, J. Lu, and L. Zhou, "Photon transport and interference of bound states in a one-dimensional waveguide," *Opt. Express*, vol. 30, no. 9, pp. 14048–14060, 2022.
- [60] D. D. Sedov, V. K. Kozin, and I. V. Iorsh, "Chiral waveguide optomechanics: First order quantum phase transitions with \mathbb{Z}_3 symmetry breaking," *Phys. Rev. Lett.*, vol. 125, p. 263606, 2020.
- [61] G. Buonaiuto, F. Carollo, B. Olmos, and I. Lesanovsky, "Dynamical phases and quantum correlations in an emitter-waveguide system with feedback," *Phys. Rev. Lett.*, vol. 127, p. 133601, 2021.
- [62] F. Le Kien and A. Rauschenbeutel, "Nanofiber-mediated chiral radiative coupling between two atoms," *Phys. Rev. A*, vol. 95, p. 023838, 2017.
- [63] D. F. Kornovan, A. S. Sheremet, and M. I. Petrov, "Collective polaritonic modes in an array of two-level quantum emitters coupled to an optical nanofiber," *Phys. Rev. B*, vol. 94, p. 245416, 2016.
- [64] E. Stourn, M. Lepers, J. Robert, S. Nic Chormaic, K. Mølmer, and E. Brion, "Spontaneous emission and energy shifts of a rydberg rubidium atom close to an optical nanofiber," *Phys. Rev. A*, vol. 101, p. 052508, 2020.
- [65] A. S. Sheremet, M. I. Petrov, I. V. Iorsh, A. V. Poshakinskiy, and A. N. Poddubny, "Waveguide quantum electrodynamics: Collective radiance and photon-photon correlations," *Rev. Mod. Phys.*, vol. 95, p. 015002, 2023.
- [66] R. J. Bettles, J. c. v. Minář, C. S. Adams, I. Lesanovsky, and B. Olmos, "Topological properties of a dense atomic lattice gas," *Phys. Rev. A*, vol. 96, p. 041603, 2017.

- [67] D. Peter, N. Y. Yao, N. Lang, S. D. Huber, M. D. Lukin, and H. P. Büchler, "Topological bands with a chern number $c = 2$ by dipolar exchange interactions," *Phys. Rev. A*, vol. 91, p. 053617, 2015.
- [68] J. Perczel, J. Borregaard, D. E. Chang, S. F. Yelin, and M. D. Lukin, "Topological quantum optics using atomlike emitter arrays coupled to photonic crystals," *Phys. Rev. Lett.*, vol. 124, p. 083603, 2020.
- [69] D. De Bernardis, F. S. Piccioli, P. Rabl, and I. Carusotto, "Chiral quantum optics in the bulk of photonic quantum hall systems," *PRX Quantum*, vol. 4, p. 030306, 2023.
- [70] M. Bello, G. Platero, J. I. Cirac, and A. González-Tudela, "Unconventional quantum optics in topological waveguide qed," *Science Advances*, vol. 5, no. 7, p. eaaw0297, 2019.
- [71] C. McDonnell and B. Olmos, "Subradiant edge states in an atom chain with waveguide-mediated hopping," *Quantum*, vol. 6, p. 805, 2022.
- [72] T. F. Allard and G. Weick, "Multiple polaritonic edge states in a su-schrieffer-heeger chain strongly coupled to a multimode cavity," *Phys. Rev. B*, vol. 108, p. 245417, 2023.
- [73] S. R. Pocock, P. A. Huidobro, and V. Giannini, "Bulk-edge correspondence and long-range hopping in the topological plasmonic chain," *Nanophotonics*, vol. 8, no. 8, pp. 1337–1347, 2019.
- [74] B. Pérez-González, M. Bello, A. Gómez-León, and G. Platero, "Interplay between long-range hopping and disorder in topological systems," *Phys. Rev. B*, vol. 99, p. 035146, 2019.
- [75] F. Appugliese, J. Enkner, G. L. Paravicini-Bagliani, M. Beck, C. Reichl, W. Wegscheider, G. Scalari, C. Ciuti, and J. Faist, "Breakdown of topological protection by cavity vacuum fields in the integer quantum hall effect," *Science*, vol. 375, no. 6584, pp. 1030–1034, 2022.
- [76] R. G. Dias and A. M. Marques, "Long-range hopping and indexing assumption in one-dimensional topological insulators," *Phys. Rev. B*, vol. 105, p. 035102, 2022.
- [77] C.-E. Bardyn, M. A. Baranov, C. V. Kraus, E. Rico, A. İmamoğlu, P. Zoller, and S. Diehl, "Topology by dissipation," *New J. Phys.*, vol. 15, no. 8, p. 085001, 2013.

- [78] C. Leefmans, A. Dutt, J. Williams, L. Yuan, M. Parto, F. Nori, S. Fan, and A. Marandi, "Topological dissipation in a time-multiplexed photonic resonator network," *Nat. Phys.*, vol. 18, no. 4, pp. 442–449, 2022.
- [79] M. Goldstein, "Dissipation-induced topological insulators: A no-go theorem and a recipe," *SciPost Phys.*, vol. 7, p. 067, 2019.
- [80] G. Shavit and M. Goldstein, "Topology by dissipation: Transport properties," *Phys. Rev. B*, vol. 101, p. 125412, 2020.
- [81] S. de Léséleuc, V. Lienhard, P. Scholl, D. Barredo, S. Weber, N. Lang, H. P. Büchler, T. Lahaye, and A. Browaeys, "Observation of a symmetry-protected topological phase of interacting bosons with Rydberg atoms," *Science*, vol. 365, no. 6455, pp. 775–780, 2019.
- [82] K. Li, J.-H. Wang, Y.-B. Yang, and Y. Xu, "Symmetry-protected topological phases in a rydberg glass," *Phys. Rev. Lett.*, vol. 127, p. 263004, 2021.
- [83] S. K. Kanungo, J. D. Whalen, Y. Lu, M. Yuan, S. Dasgupta, F. B. Dunning, K. R. A. Hazzard, and T. C. Killian, "Realizing topological edge states with Rydberg-atom synthetic dimensions," *Nat. Commun.*, vol. 13, no. 1, p. 972, 2022.
- [84] D. Barredo, S. de Léséleuc, V. Lienhard, T. Lahaye, and A. Browaeys, "An atom-by-atom assembler of defect-free arbitrary two-dimensional atomic arrays," *Science*, vol. 354, no. 6315, pp. 1021–1023, 2016.
- [85] E. Guardado-Sánchez, P. T. Brown, D. Mitra, T. Devakul, D. A. Huse, P. Schauß, and W. S. Bakr, "Probing the quench dynamics of antiferromagnetic correlations in a 2d quantum ising spin system," *Phys. Rev. X*, vol. 8, p. 021069, 2018.
- [86] D. Barredo, V. Lienhard, S. de Léséleuc, T. Lahaye, and A. Browaeys, "Synthetic three-dimensional atomic structures assembled atom by atom," *Nature*, vol. 561, no. 7721, pp. 79–82, 2018.
- [87] S. Weber, S. de Léséleuc, V. Lienhard, D. Barredo, T. Lahaye, A. Browaeys, and H. P. Büchler, "Topologically protected edge states in small rydberg systems," *Quantum Sci. Technol.*, vol. 3, no. 4, p. 044001, 2018.
- [88] M. B. M. Svendsen and B. Olmos, "Modified dipole-dipole interactions in the presence of a nanophotonic waveguide," *Quantum*, vol. 7, p. 1091, 2023.

- [89] M. B. M. Svendsen, M. Cech, M. Schemmer, and B. Olmos, "Topological photon pumping in quantum optical systems," *Quantum*, vol. 8, p. 1488, 2024.
- [90] H.-P. Breuer and F. Petruccione, *The Theory of Open Quantum Systems*. Oxford University Press, 2007.
- [91] H. T. Dung, L. Knöll, and D.-G. Welsch, "Resonant dipole-dipole interaction in the presence of dispersing and absorbing surroundings," *Phys. Rev. A*, vol. 66, p. 063810, 2002.
- [92] H. J. Carmichael, *Statistical Methods in Quantum Optics 1*. Springer Berlin, 2010.
- [93] C. Cohen-Tannoudji, J. Dupont-Roc, and G. Grynberg, *Other Equivalent Formulations of Electrodynamics*. John Wiley & Sons, Ltd, 1997.
- [94] V. V. Klimov and M. Ducloy, "Quadrupole transitions near an interface: General theory and application to an atom inside a planar cavity," *Phys. Rev. A*, vol. 72, p. 043809, 2005.
- [95] M. Tanasittikosol, J. D. Pritchard, D. Maxwell, A. Gauguet, K. J. Weatherill, R. M. Potvliege, and C. S. Adams, "Microwave dressing of rydberg dark states," *J. Phys. B At. Mol. Opt. Phys.*, vol. 44, no. 18, p. 184020, 2011.
- [96] U. Weiss, *Quantum Dissipative Systems*. World Scientific, 4th ed., 2012.
- [97] D. Manzano, "A short introduction to the Lindblad master equation," *AIP Advances*, vol. 10, no. 2, p. 025106, 2020.
- [98] C.-T. Tai, *Dyadic Green Functions in Electromagnetic Theory*. IEEE, 2nd ed., 1994.
- [99] S. Buhmann, *Dispersion forces II*. Springer Berlin, 1 ed., 2012.
- [100] H. T. Dung, S. Y. Buhmann, L. Knöll, D.-G. Welsch, S. Scheel, and J. Kästel, "Electromagnetic-field quantization and spontaneous decay in left-handed media," *Phys. Rev. A*, vol. 68, p. 043816, 2003.
- [101] L. Knöll, S. Scheel, and W. D.-G., "Qed in dispersing and absorbing media," in *Coherence and Statistics of Photons and Atoms* (J. Periňa, ed.), New York: Wiley, 2001.

- [102] N.-A. P. Nicorovici, R. C. McPhedran, and L. C. Botten, "Relative local density of states for homogeneous lossy materials," *Physica B Condens.*, vol. 405, no. 14, pp. 2915–2919, 2010. Proceedings of the Eighth International Conference on Electrical Transport and Optical Properties of Inhomogeneous Media.
- [103] T. Søndergaard and B. Tromborg, "General theory for spontaneous emission in active dielectric microstructures: Example of a fiber amplifier," *Phys. Rev. A*, vol. 64, p. 033812, 2001.
- [104] R. J. Glauber and M. Lewenstein, "Quantum optics of dielectric media," *Phys. Rev. A*, vol. 43, pp. 467–491, 1991.
- [105] A. W. Snyder and J. D. Love, *Optical Waveguide Theory*. New York, NY: Springer, 1 ed., 1983.
- [106] L.-M. Steinert, P. Osterholz, R. Eberhard, L. Festa, N. Lorenz, Z. Chen, A. Trautmann, and C. Gross, "Spatially tunable spin interactions in neutral atom arrays," *Phys. Rev. Lett.*, vol. 130, p. 243001, 2023.
- [107] A. Browaeys and T. Lahaye, "Many-body physics with individually controlled Rydberg atoms," *Nat. Phys.*, vol. 16, no. 2, pp. 132–142, 2020.
- [108] A. P. Schnyder, S. Ryu, A. Furusaki, and A. W. W. Ludwig, "Classification of topological insulators and superconductors in three spatial dimensions," *Phys. Rev. B*, vol. 78, no. 19, p. 195125, 2008.
- [109] S. Ryu, A. P. Schnyder, A. Furusaki, and A. W. W. Ludwig, "Topological insulators and superconductors: tenfold way and dimensional hierarchy," *New J. Phys.*, vol. 12, no. 6, p. 065010, 2010.
- [110] A. Kitaev, "Periodic table for topological insulators and superconductors," *AIP Conference Proceedings*, vol. 1134, no. 1, 2009.
- [111] J. K. Asbóth, L. Oroszlány, and A. Pályi, *A Short Course on Topological Insulators*. Springer International Publishing, 2016.
- [112] F. Bloch, "Über die quantenmechanik der elektronen in kristallgittern," *Zeitschr. für Phys.*, vol. 52, pp. 555–600, 1929.
- [113] S. Basu, *Topological Phases in Condensed Matter Physics*. Springer, 1 ed., 2023.
- [114] K. Kawabata, K. Shiozaki, M. Ueda, and M. Sato, "Symmetry and topology in non-hermitian physics," *Phys. Rev. X*, vol. 9, p. 041015, 2019.

- [115] T. L. Hughes, E. Prodan, and B. A. Bernevig, "Inversion-symmetric topological insulators," *Phys. Rev. B*, vol. 83, no. 24, p. 245132, 2011.
- [116] L. Fu and C. L. Kane, "Topological insulators with inversion symmetry," *Phys. Rev. B*, vol. 76, p. 045302, 2007.
- [117] M. Born and V. Fock, "Beweis des Adiabatensatzes," *Zeitschr. für Phys.*, vol. 51, no. 3, pp. 165–180, 1928.
- [118] T. Kato, "On the adiabatic theorem of quantum mechanics," *J. Physical Soc. Japan*, vol. 5, no. 6, pp. 435–439, 1950.
- [119] J. J. Sakurai and J. Napolitano, *Modern Quantum Mechanics*. Cambridge University Press, 3 ed., 2020.
- [120] M. V. Berry, "Quantal phase factors accompanying adiabatic changes," *Proc. R. Soc. A: Math. Phys. Eng. Sci.*, vol. 392, no. 1802, pp. 45–57, 1984.
- [121] E. Cohen, H. Larocque, F. Bouchard, F. Nejadsattari, Y. Gefen, and E. Karimi, "Geometric phase from Aharonov–Bohm to Pancharatnam–Berry and beyond," *Nat. Rev. Phys.*, vol. 1, no. 7, pp. 437–449, 2019.
- [122] R. Resta and D. Vanderbilt, *Theory of Polarization: A Modern Approach*, pp. 31–68. Berlin, Heidelberg: Springer Berlin Heidelberg, 2007.
- [123] D. Xiao, M.-C. Chang, and Q. Niu, "Berry phase effects on electronic properties," *Rev. Mod. Phys.*, vol. 82, pp. 1959–2007, 2010.
- [124] E. Prodan, "Robustness of the spin-chern number," *Phys. Rev. B*, vol. 80, p. 125327, 2009.
- [125] W. P. Su, J. R. Schrieffer, and A. J. Heeger, "Solitons in polyacetylene," *Phys. Rev. Lett.*, vol. 42, pp. 1698–1701, 1979.
- [126] D. J. Thouless, "Quantization of particle transport," *Phys. Rev. B*, vol. 27, pp. 6083–6087, 1983.
- [127] H.-I. Lu, M. Schemmer, L. M. Aycock, D. Genkina, S. Sugawa, and I. B. Spielman, "Geometrical pumping with a bose-einstein condensate," *Phys. Rev. Lett.*, vol. 116, p. 200402, 2016.
- [128] Y. Ke, S. Hu, B. Zhu, J. Gong, Y. Kivshar, and C. Lee, "Topological pumping assisted by Bloch oscillations," *Phys. Rev. Res.*, vol. 2, no. 3, p. 033143, 2020.

- [129] A. Przysiezna, O. Dutta, and J. Zakrzewski, "Rice–mele model with topological solitons in an optical lattice," *New J. Phys.*, vol. 17, no. 1, p. 013018, 2015.
- [130] L. Privitera, A. Russomanno, R. Citro, and G. E. Santoro, "Nonadiabatic breaking of topological pumping," *Phys. Rev. Lett.*, vol. 120, p. 106601, 2018.
- [131] M. Christandl, N. Datta, A. Ekert, and A. J. Landahl, "Perfect state transfer in quantum spin networks," *Phys. Rev. Lett.*, vol. 92, p. 187902, 2004.
- [132] S. Bose, "Quantum communication through an unmodulated spin chain," *Phys. Rev. Lett.*, vol. 91, p. 207901, 2003.
- [133] K. Korzekwa, P. Machnikowski, and P. Horodecki, "Quantum-state transfer in spin chains via isolated resonance of terminal spins," *Phys. Rev. A*, vol. 89, p. 062301, 2014.
- [134] B.-H. Huang, Y.-H. Kang, Y.-H. Chen, Z.-C. Shi, J. Song, and Y. Xia, "Quantum state transfer in spin chains via shortcuts to adiabaticity," *Phys. Rev. A*, vol. 97, p. 012333, 2018.
- [135] S. Longhi, "Topological pumping of edge states via adiabatic passage," *Phys. Rev. B*, vol. 99, p. 155150, 2019.
- [136] Y. Xing, L. Qi, X. Zhao, Z. Lü, S. Liu, S. Zhang, and H.-F. Wang, "Quantum transport in a one-dimensional quasicrystal with mobility edges," *Phys. Rev. A*, vol. 105, p. 032443, 2022.
- [137] C. Wang, X. Gu, S. Chen, and Y. xi Liu, "Topological edge state transfer via topological adiabatic passage," 2023. arXiv:2305.14529.
- [138] L. Qi, G.-L. Wang, S. Liu, S. Zhang, and H.-F. Wang, "Engineering the topological state transfer and topological beam splitter in an even-sized su-schrieffer-heeger chain," *Phys. Rev. A*, vol. 102, p. 022404, 2020.
- [139] N. E. Palaiodimopoulos, I. Brouzos, F. K. Diakonos, and G. Theocharis, "Fast and robust quantum state transfer via a topological chain," *Phys. Rev. A*, vol. 103, p. 052409, 2021.
- [140] L. Huang, Z. Tan, H. Zhong, and B. Zhu, "Fast and robust quantum state transfer assisted by zero-energy interface states in a splicing su-schrieffer-heeger chain," *Phys. Rev. A*, vol. 106, p. 022419, 2022.

- [141] T. Yuan, C. Zeng, Y.-Y. Mao, F.-F. Wu, Y.-J. Xie, W.-Z. Zhang, H.-N. Dai, Y.-A. Chen, and J.-W. Pan, "Realizing robust edge-to-edge transport of atomic momentum states in a dynamically modulated synthetic lattice," *Phys. Rev. Res.*, vol. 5, p. L032005, 2023.
- [142] F. Mei, G. Chen, L. Tian, S.-L. Zhu, and S. Jia, "Robust quantum state transfer via topological edge states in superconducting qubit chains," *Phys. Rev. A*, vol. 98, p. 012331, 2018.
- [143] R. Balian and C. Bloch, "Distribution of eigenfrequencies for the wave equation in a finite domain: I. three-dimensional problem with smooth boundary surface," *Ann. Phys.*, vol. 60, no. 2, pp. 401–447, 1970.
- [144] I. H. Malitson, "Interspecimen comparison of the refractive index of fused silica*,†," *J. Opt. Soc. Am.*, vol. 55, no. 10, pp. 1205–1209, 1965.
- [145] C. W. Peterson and B. W. Knight, "Causality calculations in the time domain: An efficient alternative to the kramers–kronig method*," *J. Opt. Soc. Am.*, vol. 63, no. 10, pp. 1238–1242, 1973.
- [146] W. O. Saxton, "Phase determination in bright-field electron microscopy using complementary half-plane apertures," *J. Phys. D: App. Phys.*, vol. 7, no. 4, pp. L63–L64, 1974.
- [147] T. Bienaimé, R. Bachelard, N. Piovella, and R. Kaiser, "Cooperativity in light scattering by cold atoms," *Fort. der Phys.*, vol. 61, no. 2-3, pp. 377–392, 2013.
- [148] C. Liedl, F. Tebbenjohanns, C. Bach, S. Pucher, A. Rauschenbeutel, and P. Schneeweiss, "Observation of superradiant bursts in a cascaded quantum system," *Phys. Rev. X*, vol. 14, p. 011020, 2024.
- [149] S. J. Masson and A. Asenjo-Garcia, "Universality of dicke superradiance in arrays of quantum emitters," *Nat. Commun.*, vol. 13, p. 2285, 2022.
- [150] C. Sayrin, C. Clausen, B. Albrecht, P. Schneeweiss, and A. Rauschenbeutel, "Storage of fiber-guided light in a nanofiber-trapped ensemble of cold atoms," *Optica*, vol. 2, no. 4, pp. 353–356, 2015.
- [151] B. Gouraud, D. Maxein, A. Nicolas, O. Morin, and J. Laurat, "Demonstration of a memory for tightly guided light in an optical nanofiber," *Phys. Rev. Lett.*, vol. 114, p. 180503, 2015.
- [152] R. Citro and M. Aidelsburger, "Thouless pumping and topology," *Nat. Rev. Phys.*, vol. 5, no. 2, pp. 87–101, 2023.

- [153] R. G. Unanyan and M. Fleischhauer, "Effect of bloch-band dispersion on the quantized transport in a topological thouless pump," *Opt. Mem. Neural Netw.*, vol. 32, no. 3, pp. S467–S475, 2023.
- [154] S. Ryu, A. P. Schnyder, A. Furusaki, and A. W. W. Ludwig, "Topological insulators and superconductors: tenfold way and dimensional hierarchy," *New J. Phys.*, vol. 12, no. 6, p. 065010, 2010.
- [155] Y. Lu, C. Wang, S. K. Kanungo, F. B. Dunning, and T. C. Killian, "Probing the topological phase transition in the su-schrieffer-heeger hamiltonian using rydberg-atom synthetic dimensions," *Phys. Rev. A*, vol. 110, p. 023318, 2024.
- [156] C. S. Adams, J. D. Pritchard, and J. P. Shaffer, "Rydberg atom quantum technologies," *J. Phys. B: At. Mol. Opt. Phys.*, vol. 53, no. 1, p. 012002, 2019.
- [157] A. Browaeys and T. Lahaye, "Many-body physics with individually controlled rydberg atoms," *Nat. Phys.*, vol. 16, no. 2, pp. 132–142, 2020.
- [158] S. Jennewein, L. Brossard, Y. R. P. Sortais, A. Browaeys, P. Cheinet, J. Robert, and P. Pillet, "Coherent scattering of near-resonant light by a dense, microscopic cloud of cold two-level atoms: Experiment versus theory," *Phys. Rev. A*, vol. 97, p. 053816, 2018.
- [159] A. Glicenstein, G. Ferioli, L. Brossard, Y. R. P. Sortais, D. Barredo, F. Nogrette, I. Ferrier-Barbut, and A. Browaeys, "Preparation of one-dimensional chains and dense cold atomic clouds with a high numerical aperture four-lens system," *Phys. Rev. A*, vol. 103, p. 043301, 2021.
- [160] R. H. Lehmberg, "Radiation from an n -atom system. i. general formalism," *Phys. Rev. A*, vol. 2, pp. 883–888, 1970.
- [161] E. Vetsch, D. Reitz, G. Sagué, R. Schmidt, S. T. Dawkins, and A. Rauschenbeutel, "Optical Interface Created by Laser-Cooled Atoms Trapped in the Evanescent Field Surrounding an Optical Nanofiber," *Phys. Rev. Lett.*, vol. 104, no. 20, p. 203603, 2010.
- [162] A. Goban, K. S. Choi, D. J. Alton, D. Ding, C. Lacroûte, M. Pototschnig, T. Thiele, N. P. Stern, and H. J. Kimble, "Demonstration of a State-Insensitive, Compensated Nanofiber Trap," *Phys. Rev. Lett.*, vol. 109, no. 3, p. 033603, 2012.
- [163] T. Nieddu, V. Gokhroo, and S. N. Chormaic, "Optical nanofibres and neutral atoms," *J. Opt.*, vol. 18, no. 5, p. 053001, 2016.

- [164] L. Scarpelli, B. Lang, F. Masia, D. M. Beggs, E. A. Muljarov, A. B. Young, R. Oulton, M. Kamp, S. Höfling, C. Schneider, and W. Langbein, “99% beta factor and directional coupling of quantum dots to fast light in photonic crystal waveguides determined by spectral imaging,” *Phys. Rev. B*, vol. 100, no. 3, p. 035311, 2019.
- [165] A. S. Sheremet, M. I. Petrov, I. V. Iorsh, A. V. Poshakinskiy, and A. N. Poddubny, “Waveguide quantum electrodynamics: Collective radiance and photon-photon correlations,” *Rev. Mod. Phys.*, vol. 95, no. 1, p. 015002, 2023.
- [166] D. Reitz and A. Rauschenbeutel, “Nanofiber-based double-helix dipole trap for cold neutral atoms,” *Opt. Commun.*, vol. 285, no. 23, pp. 4705–4708, 2012.
- [167] N. Šibalić, J. Pritchard, C. Adams, and K. Weatherill, “Arc: An open-source library for calculating properties of alkali rydberg atoms,” *Comput. Phys. Commun.*, vol. 220, pp. 319–331, 2017.
- [168] C. Hölzl, A. Götzlmann, E. Pultinevicius, M. Wirth, and F. Meinert, “Long-lived circular rydberg qubits of alkaline-earth atoms in optical tweezers,” *Phys. Rev. X*, vol. 14, p. 021024, 2024.
- [169] M. Lohse, C. Schweizer, H. M. Price, O. Zilberberg, and I. Bloch, “Exploring 4D quantum Hall physics with a 2D topological charge pump,” *Nature*, vol. 553, no. 7686, pp. 55–58, 2018.
- [170] L. Fu and C. L. Kane, “Time reversal polarization and a Z_2 adiabatic spin pump,” *Phys. Rev. B*, vol. 74, no. 19, p. 195312, 2006.
- [171] C. S. van Niekerk and R. Warmbier, “Characterization of the 2d su-schrieffer-heeger model with second-nearest-neighbor interactions,” *physica status solidi (b)*, vol. 261, no. 1, p. 2300241, 2024.
- [172] M. Goné and N. Das, “Higher-order topology and bulk-boundary correspondence in a two-dimensional ssh model,” 2024. arXiv:2407.16520.
- [173] A. Agrawal and J. N. Bandyopadhyay, “Cataloging topological phases of n stacked su-schrieffer-heeger chains by a systematic breaking of symmetries,” *Phys. Rev. B*, vol. 108, p. 104101, 2023.
- [174] B. Min, K. Agarwal, and D. Segal, “Role of bath-induced many-body interactions in the dissipative phases of the su-schrieffer-heeger model,” *Phys. Rev. B*, vol. 110, p. 125415, 2024.

- [175] C.-A. Li, "Topological states in two-dimensional su-schrieffer-heeger models," *Front. in Phys.*, vol. 10, p. 861242, 2022.
- [176] C.-A. Li, S.-J. Choi, S.-B. Zhang, and B. Trauzettel, "Dirac states in an inclined two-dimensional su-schrieffer-heeger model," *Phys. Rev. Res.*, vol. 4, p. 023193, 2022.
- [177] G. Duan, S. Zheng, Z.-K. Lin, and B. Xia, "Weak topological insulators, nodal-line semimetals, and dirac semimetals in phononic crystal plates," *Thin-Walled Struct.*, vol. 204, p. 112306, 2024.
- [178] S. Jeon and Y. Kim, "Two-dimensional weak topological insulators in inversion-symmetric crystals," *Phys. Rev. B*, vol. 105, p. L121101, 2022.
- [179] L.-Y. Zheng, V. Achilleos, O. Richoux, G. Theocharis, and V. Pagneux, "Observation of edge waves in a two-dimensional su-schrieffer-heeger acoustic network," *Phys. Rev. Appl.*, vol. 12, p. 034014, 2019.
- [180] S. Liu, W. Gao, Q. Zhang, S. Ma, L. Zhang, C. Liu, Y. J. Xiang, T. J. Cui, and S. Zhang, "Topologically protected edge state in two-dimensional su-schrieffer-heeger circuit," *Research*, vol. 2019, 2019.
- [181] W.-J. Yang, S.-F. Li, X.-Y. Zou, and J.-C. Cheng, "Characterization of zero-energy corner states in higher-order topological systems with chiral symmetry," *Phys. Rev. B*, vol. 109, p. 024114, 2024.
- [182] M. Kim and J. Rho, "Topological edge and corner states in a two-dimensional photonic su-schrieffer-heeger lattice," *Nanophotonics*, vol. 9, no. 10, pp. 3227–3234, 2020.
- [183] F. Liu and K. Wakabayashi, "Novel topological phase with a zero berry curvature," *Phys. Rev. Lett.*, vol. 118, p. 076803, 2017.
- [184] F. R. Pratama and T. Nakanishi, "Topological edge states of massless fermions with nonquantized and zero berry phases," *Phys. Rev. B*, vol. 110, p. L161409, 2024.
- [185] F. Liu, H.-Y. Deng, and K. Wakabayashi, "Topological photonic crystals with zero berry curvature," *Phys. Rev. B*, vol. 97, p. 035442, 2018.
- [186] R. Resta, "Macroscopic polarization in crystalline dielectrics: the geometric phase approach," *Rev. Mod. Phys.*, vol. 66, pp. 899–915, 1994.

- [187] H.-Y. Lu, A. S. Cuamba, S.-Y. Lin, L. Hao, R. Wang, H. Li, Y. Zhao, and C. S. Ting, "Tilted anisotropic dirac cones in partially hydrogenated graphene," *Phys. Rev. B*, vol. 94, p. 195423, 2016.
- [188] S.-M. Choi, S.-H. Jhi, and Y.-W. Son, "Effects of strain on electronic properties of graphene," *Phys. Rev. B*, vol. 81, p. 081407, 2010.
- [189] C.-H. Park, L. Yang, Y.-W. Son, M. L. Cohen, and S. G. Louie, "New generation of massless dirac fermions in graphene under external periodic potentials," *Phys. Rev. Lett.*, vol. 101, p. 126804, 2008.
- [190] M. Milićević, G. Montambaux, T. Ozawa, O. Jamadi, B. Real, I. Sagnes, A. Lemaître, L. Le Gratiet, A. Harouri, J. Bloch, and A. Amo, "Type-iii and tilted dirac cones emerging from flat bands in photonic orbital graphene," *Phys. Rev. X*, vol. 9, p. 031010, 2019.
- [191] T. Kawarabayashi, Y. Hatsugai, T. Morimoto, and H. Aoki, "Generalized chiral symmetry and stability of zero modes for tilted dirac cones," *Phys. Rev. B*, vol. 83, p. 153414, 2011.
- [192] T. Cheng, H. Lang, Z. Li, Z. Liu, and Z. Liu, "Anisotropic carrier mobility in two-dimensional materials with tilted dirac cones: theory and application," *Phys. Chem. Chem. Phys.*, vol. 19, pp. 23942–23950, 2017.
- [193] J.-P. Lang, H. Hanafi, J. Imbrock, and C. Denz, "Tilted dirac cones and asymmetric conical diffraction in photonic lieb-kagome lattices," *Phys. Rev. A*, vol. 107, p. 023509, 2023.
- [194] M. Trescher, B. Sbierski, P. W. Brouwer, and E. J. Bergholtz, "Quantum transport in dirac materials: Signatures of tilted and anisotropic dirac and weyl cones," *Phys. Rev. B*, vol. 91, p. 115135, 2015.
- [195] L. Tarruell, D. Greif, T. Uehlinger, G. Jotzu, and T. Esslinger, "Creating, moving and merging Dirac points with a Fermi gas in a tunable honeycomb lattice," *Nature*, vol. 483, no. 7389, pp. 302–305, 2012.
- [196] G. Montambaux, F. Piéchon, J.-N. Fuchs, and M. O. Goerbig, "Merging of dirac points in a two-dimensional crystal," *Phys. Rev. B*, vol. 80, p. 153412, 2009.
- [197] Z. Ringel, Y. E. Kraus, and A. Stern, "Strong side of weak topological insulators," *Phys. Rev. B*, vol. 86, p. 045102, 2012.

- [198] F. Schindler, A. M. Cook, M. G. Vergniory, Z. Wang, S. S. P. Parkin, B. A. Bernevig, and T. Neupert, "Higher-order topological insulators," *Science Advances*, vol. 4, no. 6, p. eaat0346, 2018.
- [199] A. K. Ghosh, T. Nag, and A. Saha, "Generation of higher-order topological insulators using periodic driving," *J. Phys. Condens. Matter*, vol. 36, no. 9, p. 093001, 2023.
- [200] M. Mancini, G. Pagano, G. Cappellini, L. Livi, M. Rider, J. Catani, C. Sias, P. Zoller, M. Inguscio, M. Dalmonte, and L. Fallani, "Observation of chiral edge states with neutral fermions in synthetic hall ribbons," *Science*, vol. 349, no. 6255, pp. 1510–1513, 2015.
- [201] H. Miki, S. Tsujimoto, L. Vinet, and A. Zhedanov, "Quantum-state transfer in a two-dimensional regular spin lattice of triangular shape," *Phys. Rev. A*, vol. 85, p. 062306, 2012.
- [202] W. Qin, C. Wang, and G. L. Long, "High-dimensional quantum state transfer through a quantum spin chain," *Phys. Rev. A*, vol. 87, p. 012339, 2013.